Aeroacoustic Effect of Leading Edge Erosion

An Experimental Investigation of the Impact of Leading Edge Roughness on Airfoil Self-Noise on Wind Turbine Blades

T.F. Coelen

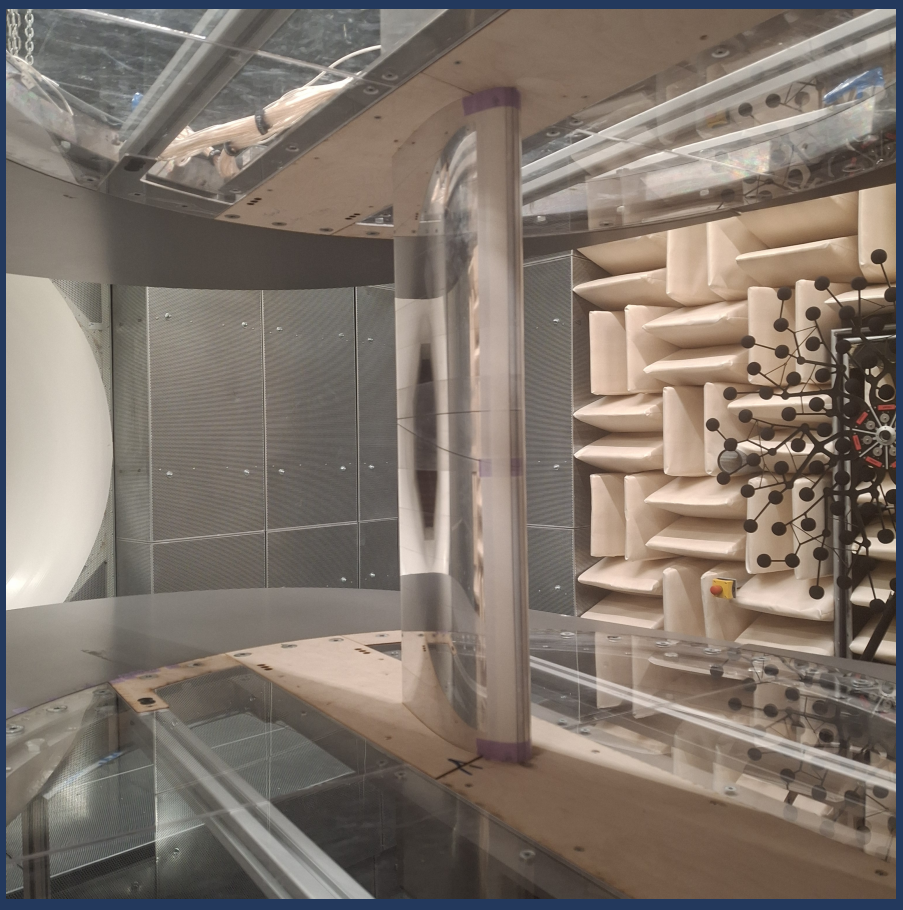

UNIVERSITY OF TWENTE.

Document No: 478

Aeroacoustic Effect of Leading Edge Erosion

An Experimental Investigation of the Impact of Leading Edge Roughness on Airfoil Self-Noise on Wind Turbine Blades

Thesis report

by

T.F. Coelen

to obtain the degree of Master of Science
at the University of Twente
to be defended on July 15, 2025 at 14:00

Thesis committee:	
Chair:	Prof.dr.ir. C.H.Venner
Supervisor:	dr.ir. A. van Garrel
External examiner:	dr.ir. J.S. Smink
Faculty:	Faculty of Engineering Technology
Place:	Enschede, The Netherlands
Project Duration:	October, 2024 - July, 2025
Student Number:	2829177
Document Number:	478

Faculty of Engineering Technology · University of Twente

Abstract

As global priorities shift towards sustainable energy, the importance of wind energy increases. In recent decades, the size of wind turbines has increased to capture more energy per turbine. This increase in size poses challenging conditions for the wind turbine blades, where tip speed can reach over 300 km/h. In harsh environmental conditions, impacts of rain and hail can lead to surface degradation in the form of Leading Edge Erosion (LEE). As a consequence, the aerodynamic performance is affected, reducing the lift and increasing the drag by up to 53% and 314%, respectively. This can lead to a drop in Annual Energy Production (AEP) of up to 3.7% In addition to the negative aerodynamic effects of LEE, it can also affect the aeroacoustic signature of the wind turbine, as the surface roughness can distort the boundary layer into becoming turbulent, thereby amplifying the self noise of the airfoil. A common complaint during the approval of a wind farm is the noise pollution experienced by surrounding communities. LEE develops overtime, the acoustic signature of the turbine at the beginning of its life cycle can be deemed acceptable by the community and regulatory agencies but can develop into unacceptable conditions. Quantifying the aeroacoustic effect of the wind turbine blade that has undergone erosion is of importance.

Therefore, this research investigated the following question: “Can leading edge erosion on wind turbine blades be detected through its influence on aeroacoustic noise signatures?”

This study investigates the impact of leading edge erosion using the aeroacoustic wind tunnel facility at the University of Twente. Seven erosion models were placed on the DU97-W-300 airfoil to simulate the conditions of leading edge erosion without damaging the airfoil surface. The experiments were carried out at Reynolds numbers of 800,000, 700,000 and 600,000 at the maximum lift-to-drag ratio. Using a microphone array and beamforming techniques, the effect of leading edge erosion was measured. The research provides insights into the modeling of roughness under non-ideal scaling conditions and depicts the relation between the roughness-induced turbulent boundary layer and the aeroacoustic effects.

Keywords: Aeroacoustics, Leading Edge Erosion, Wind Turbine, Wind Tunnel Experiment

Contents

Nomenclature

List of Abbreviations

AEP	Annual Energy Production
LE	Leading Edge
LEE	Leading Edge Erosion
LEP	Leading Edge Protection
PSD	Power Spectral Density
RPM	Revolutions Per Minute
SPL	Sound Pressure Level
TE	Trailing Edge
WT	Wind Turbine

List of Symbols

α	Angle of attack (°)
α_t	Wind tunnel angle of attack (°)
β	Angle of sideslip (°)
δ	Boundary layer thickness (m)
δ^*	Displacement thickness (m)
μ	Dynamic viscosity ($Pa{\cdot}s$)
ω	Angular velocity (rad/s)
ρ	Air density (kg/m^3)
τ_w	Wall shear stress (Pa)
θ	Momentum thickness (m)
ε	Equivalent sand grain roughness (m)
φ	Twist angle (°)
c	Chord length of airfoil (m)
C_f	Skin friction coefficient ($-$)
f	Frequency (Hz)
k	Roughness height (m)
Ra	Arithmetic average roughness height (m)
Re	Reynolds number ($-$)
Re_θ	Reynolds number based on momentum thickness ($-$)
Re_k	Roughness Reynolds number ($-$)
Rz	Average peak-to-valley roughness height (m)
St	Strouhal number ($-$)
u	x-direction velocity component (m/s)
$u(k)$	Velocity at roughness height (m/s)
U_∞	Free-stream velocity (m/s)
v	y-direction velocity component (m/s)
w	z-direction velocity component (m/s)
x, y, z	Spatial coordinates (m)

List of Figures

List of Tables

1

Introduction

1.1. Context

The world is transitioning to a greener way of producing our energy requirements. One of the major goals is to limit the increase in global temperature to $1.5°C$ above preindustrial levels, as outlined in the Paris agreement. To achieve this, we need to reduce our dependence on fossil fuels and transition to renewable energy sources. Wind energy plays a large role in this transition, as it is a prevalent source of clean, sustainable energy. In northern European countries such as the Netherlands, wind energy has enormous potential. The installed capacity for wind energy has been steadily growing over the last few decades. In the Netherlands, a total of 11 GW of wind energy capacity have been installed as of 2024, with close to half of that capacity coming from offshore wind turbines. The energy generated by wind turbines constituted 28 % of the total energy produced in the Netherlands, amounting to 33.5 TWh [1]. In addition to the positive impact of sustainable energy sources in reducing CO_2 emissions, reducing fossil fuel use also decreases the dependence of the Netherlands on foreign oil producing countries and can provide us with energy independence. As wind turbines have become more prominent in our energy production, their size has increased. Although this offers advantages, mainly in the amount of power produced by each turbine, increasing the size also has some negative consequences. Larger turbines are exposed to more demanding conditions. Another challenge in using wind energy is more human in nature. The installation of wind turbines is often opposed by surrounding communities; not only because they can be seen as an eyesore, but also because they can cause noise pollution.

(a) Leading edge erosion [2]

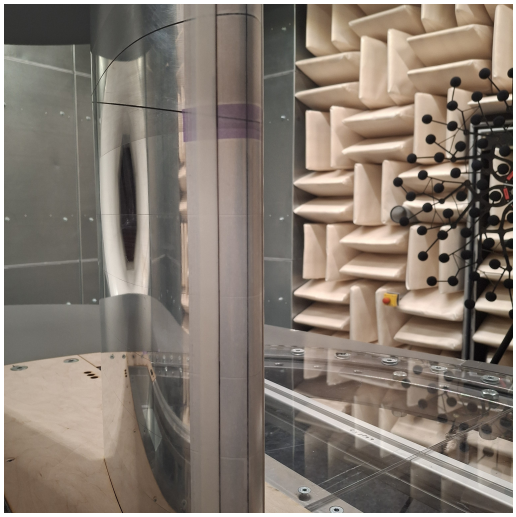

(b) Experimental wind tunnel setup

Figure 1.1: Leading edge erosion and experimental wind tunnel setup

1.2. Problem definition

When an object moves through the air, the interaction between the object and the air causes disturbances that present themselves as noise. During the operation of a wind turbine, the turbine is subjected to harsh conditions, both mechanical and environmental. Over time, the surface of the blade can become damaged due to repeated impacts from rain and hail. Most of this environmental stress is concentrated on the leading edge of the blade, causing erosion of the material. Initially, the damage appears as small pits. As time progresses and more impacts occur, the pits deepen and merge with others, gradually forming gouges. These features grow larger, wear the protective coating, and eventually damage the underlying laminate structure. This leads to delamination of the blade structure [3]. Leading Edge Erosion (LEE) can have severe consequences for wind turbine performance. It can reduce the lift coefficient by up to 53 %, increase the drag by up to 314 %, and result in a reduction of the Annual Energy Production (AEP) by up to 4 % [4]. A decrease in AEP also lowers the return on investment for a wind turbine. A study showed that a 2 % reduction in AEP for an offshore wind turbine could lead to losses of more than 4 million euros per year [5]. In addition to lowering energy output, LEE can also be detrimental to the structural integrity of the wind turbine, which could potentially lead to damage to the turbine blade to the point where it cannot be repaired [5]. Although the operational life of a wind turbine is around 20 years, erosion of the leading edge can significantly affect its long-term durability and performance. Often, the LEE of the wind turbine blades can start to form as early as two years after the start of operation [5] depending on the location of the wind turbine. Therefore, Leading Edge Protection (LEP) solutions can mitigate the effect of the erosion on the leading edges of the turbine blades; however, they typically do not last the life of the blade and require maintenance and are often replaced after 3 to 5 years of service. This issue is particularly relevant for offshore wind turbines, which are generally larger and operate under higher wind speed conditions. Due to their remote locations, inspection and repair work is more difficult and costly [6]. The maintenance cost of wind turbines was estimated to be 20 % of the levelized electricity cost [7]. By developing better tools to analyze the performance of the wind turbine, this could aid in the maintenance of the wind turbine by providing a more complete picture of the state of the turbine.

1.3. Relevance

As wind turbines become more and more prevalent and the available land is finite, wind turbines are a more common site and are placed closer to communities. As the goal is to increase the lifespan of wind turbine blades and erosion becomes more severe as a function of time, a better understanding of the aeroacoustic effects of the LEE on the wind turbine blades is important. A common complaint during the approval of a wind farm is the noise pollution experienced by surrounding communities. LEE develops over time, the acoustic signature of the turbine at the beginning of its life cycle can be deemed acceptable by the community and regulatory agencies, but can develop into unacceptable conditions.

1.4. Research objective

The purpose of the research was to investigate the ability to identify the presence of leading edge erosion on wind turbine blades using experimental methods. The idea is to test whether different levels of erosion can be detected through aeroacoustic measurements. This resulted in the main research question:

Research question

Can leading edge erosion on wind turbine blades be detected through its influence on aeroacoustic noise signatures?

To address the main research question. The first challenge is to figure out how LEE can be realistically modeled for the limited wind tunnel capabilities while still remaining realistic compared to actual wind turbine operating conditions. Then investigate whether the acoustic differences between clean and eroded airfoils can be detected using beamforming techniques and thereby identify how the LEE influences the acoustic signature of an airfoil, specifically in terms of sound pressure levels and power spectral density.

1.5. Scope

This study is experimental in nature, designed to explore the fundamentals of airfoil self-noise. The experimental investigation will be conducted using the wind tunnel model with the DU97-W-300 airfoil in the aeroacoustic wind tunnel at the University of Twente. To avoid damaging the airfoil during testing, actual erosion in the form of damage not induced on the airfoil. Instead, seven erosion models were designed to simulate different stages and types of surface damage. These models were applied to the airfoil surface using self-adhesive foils creating a simulated damaged leading edge. Acoustic measurements were taken using an array of 112 MEMS microphones (Micro-Electro-Mechanical Systems). The data was analyzed using the microphone array where the sound pressure levels, power spectral densities were calculated, and beamforming algorithms were used to identify and quantify noise sources within the experiment.

1.6. Thesis outline

Part I – Fundamentals of erosion and aeroacoustic analysis

Chapter 2 discusses the theoretical background behind LEE, boundary layers, surface roughness, and aeroacoustic noise. These topics are required to understand how erosion affects airfoil performance and what role it plays in acoustic performance.

Chapter 3 gives a literature review that summarizes earlier work on erosion modeling, acoustic measurements, and previous experiments. This shows what has already been done and where this study fits in.

Part II – Experimental design and data acquisition methods

Chapter 4 and 5 describe the wind tunnel setup, the airfoil used, and how the erosion features were modeled. It also goes into measurement equipment and test conditions.

Chapter 6 explains how the acoustic data was processed. This includes temperature corrections, beamforming, and how the sound pressure and power spectra were calculated.

Part III – Experimental findings and analysis of aeroacoustic measurements

Chapter 7 shows the differences in acoustic performance between clean and eroded airfoils. It includes SPL levels, beamforming plots, and spectral comparisons between the different erosion models.

Part IV – Conclusion of results and future outlook

Chapter 8 summarizes the results and answers the research questions.

Chapter 9 gives recommendations for future work, based on the findings and limitations of this study.

Part I

Fundamentals of erosion and aeroacoustic analysis

2

Theoretical background

2.1. Leading edge erosion

During the operation of wind turbines, the turbines are subjected to harsh conditions, both mechanical and environmental. This problem is not exclusive to wind turbine blades, but it also occurs in compressors, turbines, and other various aerospace structures [8]. Most of the environmental stress of the wind turbine blade is focused on the leading edge of the turbine. In particular, offshore wind turbines, which generally are larger, and operate in higher wind speed conditions and at higher tips speeds. Due to their remote locations, the inspection and repair work required are more costly [6]. In this chapter, we will look at the cause and the effect of LEE and we will discuss methods used to combat this problem.

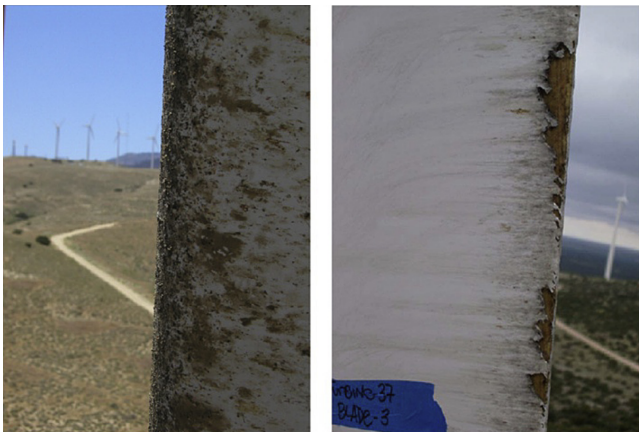

Figure 2.1: Leading edge erosion of wind turbine blades [9]

2.1.1. Cause of leading edge erosion

Over time, the stress of environmental conditions caused by the impact of raindrops, hail or sand particles, causes the leading edge of the turbine blade to degrade, causing surface roughness, material loss, and eventually structural damage [4].

In addition to mass loss caused by erosion, there are also other factors that could have a negative impact on the wind turbine blades, such as icing. Similarly to the phenomena on airplane wings, due to humid and cold conditions, ice could accumulate on the turbine blade; this can also have negative effects on the performance of a wind turbine. However, for this study we will only look at erosion at the leading edge [10].

The severity of erosion at the leading edge depends on several factors; (1) The frequency of impacts at the leading edge, depending on the climate conditions at the site where the wind turbine is located, the frequency of impacts can vary [11]. Depending on the rotational speed and the diameter of the rotor, the velocity of the impacts can increase. (2) The mass of the particle is the other contributing factor, and depending on the type and size of the impacting particle, the severity of the impact could increase, resulting in more damage. (3) The geometry of the blade is also important and explains why erosion features are mainly seen on the leading edge of the wind turbine blade [12]. The reason is that if an impact occurs close to the normal direction of the surface, the force of the impacting particle is greater than when it would have ricocheted on the upper or lower surface of the airfoil [11]. (4) The properties of the material of the leading edge of the blade. Depending on the

material of the wind turbine blade, the resistance to LEE can vary [11]. As a result of impacts, the leading edge will start to degrade [3]. Initially, the damage on the blade will present itself as small pits as time progresses and more impacts occur, the pits deepen and merge with other pits gradually forming gouges. These features eventually ”eat” up the protective coating and start to damage the underlying laminate structure; this damage then causes delamination of the structure. The problem of leading edge erosion is a relatively new field of study as the life spans of the wind turbine blades are increasing [13], and the erosion damage has more time to accumulate.

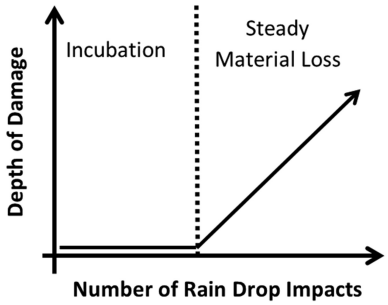

Figure 2.2: Temporal development of surface damage versus number of impacts [14]

2.1.2. Effect of leading edge erosion

Han et al. [4] published a paper on the effects of LEE on the NREL 5MW reference wind turbine. In the study a Computational Fluid Dynamics (CFD) analysis was performed and the results show that the NACA 64618 airfoil with leading edge erosion had a maximum drag increase of 314 % and a lift decrease of 53 % [4]. In a report by Vastas [15] that in extreme cases of leading edge contamination, such as severe stages of leading edge erosion, a reduction in annual energy production is estimated between 10 and 13 %. Several other papers discussed the loss of AEP due to the presence of LEE, where the loss ranges from 2.3 to 25 % [2], [4], [10], [16], [17]. Many studies aim to quantify the effect on AEP as a result of LEE; however, this study aims does not focus on AEP, but on the aeroacoustic effects of LEE.

When a droplet impacts a surface, a pressure zone is generated in which the momentum of the droplet is absorbed by the material, as shown in Figure 2.3. This generates stress waves in the material, where the propagation of the stress waves though the material are dependent on the material properties like the elasticity modulus, the Poisson’s ratio and the density. When the amplitude of the stress wave exceeds the fracture strength of the material, it can lead to erosion of the material. However, because of the continuous impacts seen on the leading edge of the wind turbine blades, the material also experiences fatigue, where the stress may not exceed the limit of the material, but it can fail over time.

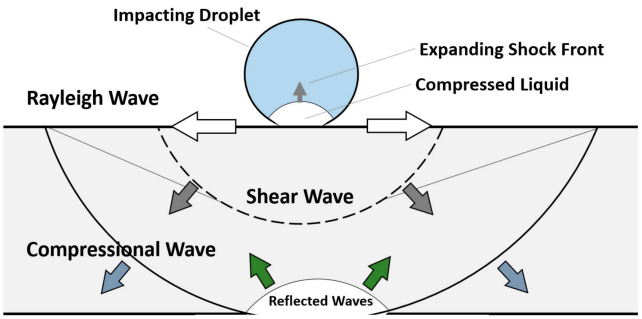

Figure 2.3: Stress wave propagation as a result of a water droplet impact on a solid surface [18]

The Springer model, as described in detail by Hoksbergen [19], is a widely used model to predict the lifetime of a turbine or compressor blade undergoing erosion conditions. The model has also been used to quantify the effect of leading edge erosion on a wind turbine blade over time and determine the resistance against erosion conditions. Using the properties of the material and the properties of the impacting material as an input.

2.1.3. Prevention

To reduce the effect of leading edge erosion and make turbine blades more resilient to environmental conditions, several protection systems have been developed. The most basic form of protection for LEE is the protective tape or paint that is placed on the leading edge of the blade [20]. The drawback of adding a protective tape section to the leading edge of the blade is that it alters the geometry of the turbine blade. In Section 2.3.5 the critical roughness height will be discussed, from where aerodynamic performance starts to deteriorate. Therefore, the allowable depth of the LEE is limited in thickness. One of the benefits of having a post-mold protective layer has, is that the layer can be replaced before the erosion affects the turbine blade itself. More recent developments include the introduction of leading edge protection within the mold of the wind turbine blade. These are called in-mold coatings; in the production of the wind turbine blade, the leading edge has a cavity. After the blade laminate structure is produced, the cavity can be filled with a material selected to withstand impacts [13]. When in mold leading edge protection is used, the thickness of protection is not as limited as in the case of post-molded leading edge protection. Although there is a great deal of research conducted in the field of leading edge erosion protection systems, LEE remains a prevalent problem [3].

2.2. Modeling of LEE/surface roughness

2.2.1. Fundamentals of roughness

In both materials science and engineering, the surface roughness parameter Ra is often used, which represents the average deviation in height from the mean surface height. However, the limitation of using Ra to describe the severity of the roughness of LEE is that Ra is an average over a set length of a surface. The pits and gouges are erosion features that are relatively well distributed over a certain surface area; however, in the case of delamination, the erosion feature is only a singular location where the flow effectively encounters a wall. Therefore the classic parameter Ra is not suitable for scaling a localized roughness feature, such as delamination [21].

$$Ra = \frac{1}{l_r} \int_0^{l_r} |z(x)| dx \tag{2.1}$$

Unlike the roughness parameter Ra, the roughness parameter Rz quantifies the roughness as a function of the highest and lowest points of a surface. This parameter would be more suitable for the delamination feature of the LEE. As it better represents the singular peak as seen in the delamination, however, it is still a mean value.

$$Rz = \frac{1}{n} \sum_{i=1}^{n} (Z_{p,i} + Z_{v,i}) \tag{2.2}$$

The arithmetic average deviation from the mean line can be misleading. As shown in Figure 2.4, a sharp step-like function and a smooth sine wave can have the same R_a value, although they interact differently with the boundary layer.

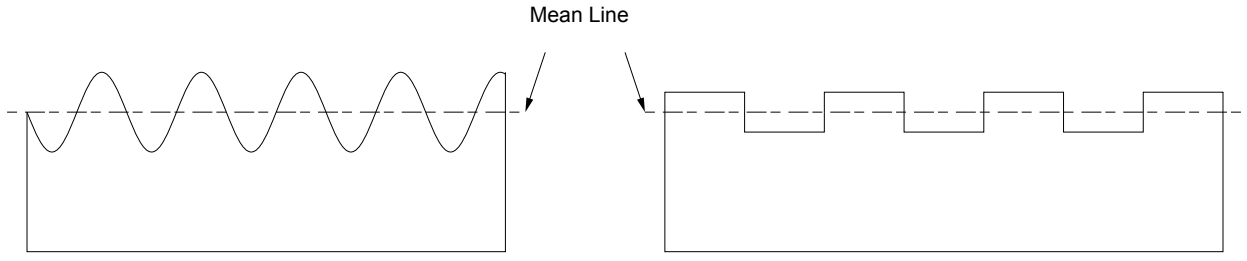

Figure 2.4: Different surface topology with the same Ra value

2.2.2. Dimensionless scaling

For modeling or scaling real world conditions, the concept of similarity is a tried and tested concept [22]. Here, by using dimensionless numbers, the conditions in the flow can be kept similar regardless of the physical scale. If, for instance, there is no way to test a model in a wind tunnel at the same physical scale of that in the real

world conditions, the parameters of the wind tunnel experiment can be adjusted in magnitude to maintain the "same" dimensionless number, thereby providing flow similarity. The experiment is limited by the capacity of the wind tunnel itself and is unable to analyze the airfoil for the exact operating conditions and is limited to $Re_c \approx 1 \times 10^6$.

Reynolds number
The Reynolds number is arguably the most famous dimensionless parameter. The Reynolds number as shown in Equation 2.3, relates the inertial $\rho u x$ and viscous effects μ of the flow. This describes how the flow interacts with a geometry; this allows the geometry described by the length parameter x to interact with the flow [23]. This ratio is particularly important in the boundary layer, where the viscous forces acting between the fluid and the surface interact with the inertia of the flow. This ratio can show whether the flow tends to remain laminar or transitions to turbulence: when the inertial forces are sufficiently large enough to overcome the viscous forces the flow can turn turbulent. This is of special interest to the current problem as when the turbulent structures at the TE cause unsteady pressure perturbations (noise).

$$Re = \frac{\rho u x}{\mu} \tag{2.3}$$

Boundary layer momentum thickness number Reynolds
The momentum thickness Reynolds number uses momentum thickness as the length scale denoted by x in Equation 2.3. The momentum thickness denoted by Equation 2.4 for incompressible flow, is the loss of momentum caused by the boundary layer, compared to that of the free stream velocity. The momentum thickness is the height of a layer of freestream velocity that would contain momentum equal to that of the momentum loss in the boundary layer [24].

$$\theta = \int_0^\infty \frac{u}{U_\infty}\left(1 - \frac{u}{U_\infty}\right) dy \tag{2.4}$$

The momentum thickness Reynolds number is defined as shown in Equation 2.5 [25].

$$Re_\theta = \frac{\rho U \theta}{\mu} \tag{2.5}$$

Roughness height Reynolds number
The roughness height Reynolds number is often used to determine if a roughness feature is large enough to cause a disturbance to affect the boundary layer and cause a transition from laminar to turbulent. Similarly to the chord-based Reynolds number, Smith et al. [25] investigated this and a critical roughness Reynolds number Re_{kcrit} was measured and determined to lie between 60 to 1100 [25]. The formulation of the roughness height Reynolds number is shown in Equation 3.4. In the equation, k denotes the height of the roughness feature and $u(k)$ is the boundary layer at the height where the undisturbed flow would encounter the roughness feature. This is illustrated in Figure 2.5.

$$Re_k = \frac{\rho u(k) k}{\mu} \tag{2.6}$$

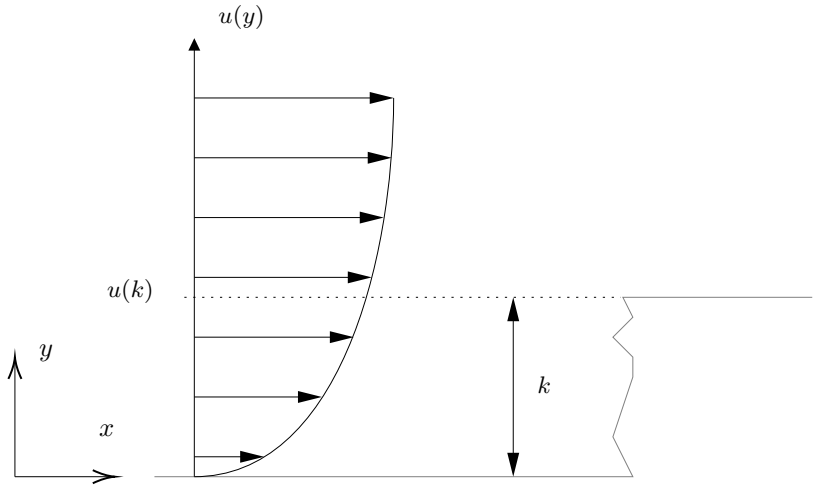

Figure 2.5: Illustration components Reynolds roughness number

2.2.3. Empirical roughness scaling

In 1933, Nikuradse conducted extensive experiments on the influence of surface roughness on flow through pipes [26]. In the experiments, the inside of the pipes were coated with sand grains and, based on the average diameter of the sand grains ϵ, the roughness increased. The effect of the roughness was then related to the pressure loss. This approach gave engineers a relatively simple method to relate the roughness of a surface to the pressure loss in a pipe. The Darcy-Weissbach equation uses a friction factor f_{DW}, which is dependent on the relative roughness ϵ/D and the Reynolds number of the flow. To find the friction factor f_{DW} using the Moody chart the the Reynolds number and the relative roughness is used, where f_{DW} was empirically derived. The Moody chart itself is basically a plot of the Colebrook-White equation that implicitly calculates f for turbulent flow [27]. Pipes are a relatively simple shape and can be easily scaled. Airfoils however, are geometrically quite complex structures. Some airfoil shapes are geometrically well defined and are able to be somewhat scaled. Most notably the NACA airfoil series, where the contour of the airfoil is determined by a function. The properties of the boundary layer are not easily scaled, and it is hard to correlate the effects of surface roughness, geometry, and Reynolds number.

2.3. Boundary layer theory

The TE noise on an airfoil is a result of the pressure perturbations that are formed. These perturbations and thereby the noise emitted are intensified when a boundary layer is more turbulent. Knowing how the boundary layer interacts with both erosion and roughness is useful. The intensity of the noise emitted is dependent on the state of the boundary layer. For example, a laminar boundary layer produces relatively low-amplitude and low-frequency noise as a result of its smoother, more orderly structure [28]. A turbulent boundary layer contains a wider spectral range in turbulent structures and pressure perturbations are stronger, the noise induced is larger in magnitude compared to laminar boundary layers. The interaction between the flow and the TE forms a key mechanism in the generation of TE noise. Understanding the boundary layer and its characteristics and how and if LEE can cause the transition from laminar to turbulent flow can give insight into the problem. In this chapter some fundamentals behind the boundary layer will be described, following that the effect of roughness on the boundary layer theory is of specific interest relative to our problem the acoustics effects of LEE.

2.3.1. Boundary layer fundamentals

The concept of the boundary layer was first introduced by Ludwig Prandtl in his famous 1904 paper [29]. In this paper, Prandtl discusses the interaction between a moving fluid moving over an object. In the paper he proposed that viscous friction within the fluid leads to the formation of a thin layer near the surface, where the velocity of the fluid increases from zero at the wall to the free stream velocity at the edge of the boundary layer. The assumption was made that the relative velocity of the fluid was zero at the surface of an object (the no slip condition). Outside of this boundary layer, the flow is not affected by viscous effects as in the boundary layer as the difference in velocity of the fluid particles in the free stream negligible and therefore can be treated as

inviscid [30] [29]. This principle can be seen in Navier–Stokes equations as derived in the appendix A, which show that viscous friction forces are proportional to the velocity gradient, leading to shear stresses within the boundary layer that exert a drag force on the surface.

2.3.2. Types of boundary layers

There are several stages of a boundary layer, the velocity profile starts at the surface of an object where there is no relative velocity between the surface and the flow. As the distance between increases, the velocity in the flow starts to increase until it reaches the edge of the boundary layer. This edge is commonly defined as $u(y) = 0.99u_e$ where y is the direction normal to the surface [22]. This threshold is used because, in theory, viscous effects extend infinitely far from the surface. However slight the effect may be, there are still results of the viscous forces through a medium, but at a certain point they are deemed to become negligible.

Upon the formation of the boundary layer, the fluid flow exhibits a smooth and parallel motion relative to the surface of the object, with negligible mixing between the fluid layers [22]. At this stage, the boundary layer is characterized as laminar.

In a turbulent boundary layer, unlike laminar boundary layers, there are velocity components that are not only parallel to the surface, causing mixing between the ”layers” in the flow. This mixing causes fluctuations in velocity and pressure in turbulent structures. In general terms, this occurs when the inertial forces are large enough to overcome the viscous dampening effects. This ratio is most famously described in the Reynolds number. Due to this mixing, the velocity gradient becomes steeper, and this higher velocity gradient increases the shear stress on the wall [31]. Due to the increase in momentum close to the surface, the flow becomes less prone to separate from the surface.

Between the laminar and turbulent phases of the boundary layer, there is a transition period in which the mixing of the layer increases. This transition starts off with unstable Tollmien-Schlichting waves that eventually develop into vortex formations that then turn into spots of turbulence that then develop into turbulent flow [31].

The development of the boundary layer is shown in the Figure 2.6. In the figure the development of the boundary layer over a flat plate is shown. The dashed line above the flat plate shows the thickness of the boundary layer, and below the flat plate shows the velocity profile.

For a flow over a flat plate at a certain point it has been observed that the boundary layer starts to transition, this typically happens at a certain loacal Reynolds number. The Reynolds number is not the only factor in the transition of the boundary layer from laminar to turbulent. Other factors that influence the point of transition are; the level of turbulence of the free stream, the temperature difference between the surface, the presence of adverse pressure gradients the noise level in the outer flow, and the roughness of the surface [22]. The latter is of special interest for this study.

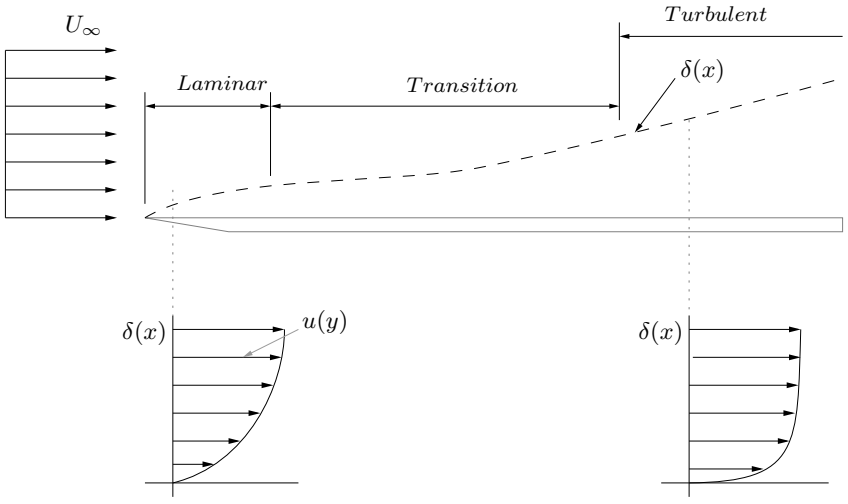

Figure 2.6: Development of a boundary layer over a flat plate

2.3.3. Boundary layer characteristics

There are several parameters that characterize and can help describe the boundary layer. In this section, these parameters that characterize the boundary layer are discussed.

Boundary layer thickness δ
This thickness of the boundary layer as described previously is defined as the height where the velocity is 99 % of the free stream velocity.

Displacement thickness δ^*
The displacement thickness δ^*, can be seen as the distance to which the outer flow would be shifted to compensate for the reduced mass flow rate caused by the slower fluid inside the boundary layer. The value gives an idea of how much mass flow is reduced near the wall due to viscosity [30]. The boundary layer effectively increases the thickness of an object for inviscid flow. Due to these viscous effects, the mass flow through the height boundary layer δ is less than it would be at the same height in the free stream, where the flow is uniform. This difference is δ^* and is mathematically described for incompressible flow by the equation shown in 2.7 [22] [31]:

$$\delta^*(x) = \int_{y=0}^{\infty} (1 - \frac{u}{U}) dy \tag{2.7}$$

Momentum thickness θ
The momentum thickness θ shows the thickness that accounts for the momentum loss within the boundary layer as a result of viscous effects [22]. The boundary layer reduces the momentum carried by the flow compared to what it would be like in an free stream. The momentum thickness shows this reduction by equating it to the loss of momentum compared to if the entire flow were a uniform freestream profile. This is mathematically described by Equation 2.8 [31].

$$U^2\theta = \int_{y=0}^{\infty} u(U-u)\, dy \tag{2.8}$$

Here, the integral captures the momentum deficit across the boundary layer, comparing the velocity component in the boundary layer $u(y)$ with the free-stream velocity U.

Skin friction coefficient C_f
The skin friction coefficient C_f, is a dimensionless factor that represents the shear stress exerted on a surface as a result of viscous effects within the boundary layer. The viscous effects result in the velocity gradient, where the non-slip condition causes the fluid velocity to be zero relative to the surface, as described by Prandtl [30]. The shear stress that develops due to viscosity is captured by C_f. This coefficient is mathematically defined as shown in Equation 2.9 [22]

$$C_f = \frac{\tau_w}{\frac{1}{2}\rho U^2} \tag{2.9}$$

Here τ_w is the wall shear stress. The wall shear stress is related to the velocity gradient in the wall and is defined as shown in the Equation 2.10.

$$\tau_w = \mu \left(\frac{\partial u}{\partial y} \right)_{y=0} \tag{2.10}$$

2.3.4. Boundary layer equations

By taking the conservation equation and applying some assumptions and conditions, the equations can be significantly reduced. This has been described extensively, most notably by Schlichting [31], who was a student who originally studied under Prandtl, who first introduced the concept of the boundary layer [29].

Assumptions and conditions
To apply the boundary layer equations, a few assumptions are made:

- The flow is assumed to be two-dimensional.
- The flow is steady
- No slip at the wall
- The boundary layer is thin compared to the chord length, so $\delta \ll c$.
- The Reynolds number is sufficiently large.

$$\boxed{\frac{\partial}{\partial x}(\rho u) + \frac{\partial}{\partial y}(\rho v) = 0} \tag{2.11}$$

$$\boxed{\frac{\partial p}{\partial x} + \frac{\partial u}{\partial x}(\rho u) + \frac{\partial u}{\partial y}(\rho v) = \frac{\partial}{\partial y}(\mu \frac{\partial u}{\partial y})} \tag{2.12}$$

$$\boxed{\frac{\partial p}{\partial y} = 0} \tag{2.13}$$

The von Kármán momentum equation
Understanding the boundary layer is useful when analyzing the effect of erosion on aerodynamic performance and acoustic signature. The von Kármán momentum equation is a simplified, yet powerful way to describe how momentum is lost in the boundary layer due to viscous effects that are a result of roughness [32]. The momentum thickness θ gives a measure of how much momentum is lost in the boundary layer compared to if the flow were inviscid. The von Kármán integral equation relates this loss to the wall shear stress and external pressure gradient. For incompressible, steady 2D flow, the equation is given by:

$$\frac{d}{dx}\left(\rho U_e^2 \theta\right) + \rho U_e \frac{dU_e}{dx}\delta^* = \tau_w, \tag{2.14}$$

This equation shows that the boundary layer does not just ”slow down” the air, momentum is taken away from the flow. The loss of this momentum builds up along the surface of the airfoil and is seen in the form of skin drag. From an engineering point of view, this means that we can estimate the skin friction and pressure drag just by knowing how the boundary layer develops. Another way to look at it is that the momentum in the airfoil wake thickness is related to the drag through;

$$D = \rho U_e^2 \theta, \tag{2.15}$$

which tells us that a thicker boundary layer and therefore more momentum loss leads to higher drag on a body. This is particularly relevant when talking about leading edge erosion. When the surface becomes rough, the boundary layer trips earlier and grows thicker more quickly. This increases δ^* and θ, which directly increases drag which negatively affects aerodynamic and acoustic performance. Especially in adverse pressure gradients ($\frac{dU_e}{dx} < 0$), the effect of δ^* becomes more pronounced. A large displacement thickness combined with a decrease in U_e results in a significant increase in drag and potentially flow separation.

2.3.5. Effect of surface roughness on the boundary layer

This study focuses on the effect of LEE on the aeroacoustics of a wind turbine blade. In essence, the LEE acts as surface roughness, and as discussed before, the surface roughness can have an effect on the transition of the boundary layer and the development of the turbulence downstream. This boundary layer, in turn, has influence on acoustics.

Types of roughness
There are two types of surface roughness, single element roughness and distributed roughness elements [31]. The single element roughness, as the name suggests, is a singular roughness feature that obstructs the path of the boundary layer. This can be a bump or drop on a surface where a fluid is flowing. The other type of surface roughness is a distributed surface roughness where a continuous section of a surface has a non-smooth surface [22].

Critical roughness height

The critical roughness height is the maximum height that a roughness feature can have on the surface of an object without affecting the transition point of the boundary layer [25]. When the surface roughness remains below this critical height, the surface is considered hydrodynamically smooth. As mentioned earlier, the boundary layer transition depends on several factors, one of which is the surface topology. In addition to the height of the roughness, its shape also plays an important role in disturbing the boundary layer.

The key parameters that influence the transition are [25]:

- The height of the roughness (k)
- The streamwise position of the roughness feature (x_k)
- The velocity within the boundary layer at the top of the roughness $(u(k))$
- The free-stream velocity (U_∞)
- The pressure gradient at the roughness location
- The viscosity of the fluid (μ)

The roughness height Reynolds number is often used to determine if a roughness feature is large enough to cause a disturbance to be large enough to affect the boundary layer and cause a transition from laminar to turbulent [25]. Similarly to the chord-based Reynolds number, a critical roughness height Reynolds number was investigated and was determined to be between $Re_{kcrit} = 60 \rightarrow 1100$ [33]. The formulation of the roughness height Reynolds number is shown in Equation 3.4. In the equation, k denotes the height of the roughness feature and $u(k)$ is the velocity of the height of the boundary layer where the flow encounters the roughness feature, this is shown in Figure 2.5.

$$Re_k = \frac{\rho u(k) k}{\mu} \tag{2.16}$$

Whenever the roughness height k is small in comparison to the thickness of the boundary layer, we can assume that the boundary layer is a linear function, this assumes that the roughness feature only exits in the lower viscous layer of the boundary layer. Through this approximation we can say that the velocity component at height k can be approximated by this linear velocity profile [34]. In this, A is a constant that indicates the gradient of the linear part of the boundary layer and is proportional to wall shear stress τ_w.

$$\frac{u(k)}{U} = \frac{Ak}{\theta_k} \tag{2.17}$$

Thus the Reynolds roughness number can be approximated as shown in Equation 2.18. In the equation, the term θ_k is the thickness of the momentum at the location of the defect, as the thickness of the momentum increases as the boundary layer develops and therefore is related to Re_c [34].

$$Re_k = \frac{\rho u(k) k}{\mu} = \frac{\rho U \theta_k}{\mu} \frac{u(k)}{U} \frac{k}{\theta_k} = A R_{\theta_k} (\frac{k}{\theta_k})^2 \tag{2.18}$$

As shown in the equation, the Reynolds roughness number scales quadratically with the on the basis of the ratio of k/θ_k. The quadratic scaling, in combination with the gradient A, approximates the velocity profile of the boundary layer.

Whenever the roughness height k exceeds the thickness of the boundary layer, we can no longer approximate the linear scaling of velocity in the boundary layer. Hence $u(k) = U_e$ because the roughness characteristic sticks above the thickness of the boundary layer δ_k and is in the free stream. The Reynolds roughness number at this point is scaled linearly on the basis of the momentum thickness at the point where the roughness feature is located.

$$Re_k = \frac{k}{\theta_k} Re_{\theta_k} \tag{2.19}$$

Smith et al. [34] conducted experiments to determine the smallest roughness that could disturb the boundary layer into transition. In the experiments, what was found was that an Re_k of less than 80 does not significantly disturb the boundary layer enough. If the value for Re_k falls below this, a surface/object is deemed to be hydro dynamically smooth.

2.3.6. Boundary layer tripping devices

Sometimes, the transition of the boundary layer is desired; to do this, tripping devices are used. The reason for wanting a turbulent flow instead of a laminar boundary layer may seem counter-intuitive at first. As a turbulent boundary layer increases the skin drag on the body, it reduces the aerodynamic efficiency. However, a turbulent boundary layer is more likely to stay attached to the surface, and for this reason the separation of boundary layer from the surface is delayed. This prolonged attachment of the boundary layer could pay its dividends if the drag caused by separation is reduced and a penalty is taken on the skin drag. There are several methods to trip the flow. The most common and widely used method is the tabulator strip, also known as the zigzag strip. This was studied in the paper by Hama [33], where the effectiveness of different tripping devices was discussed. In addition to the zigzag strip, another alternative is the use of sand paper, where the surface roughness is increased by applying a sandpaper-like surface finish. When this is applied to a surface and if the critical roughness height is reached, the boundary layer is forced into transition earlier than under hydro dynamically smooth conditions. Similarly to sandpaper, a mesh-like structure could be applied, which essentially functions in a method similar to that of the sandpaper and is distributed in roughness. In addition to the application of a zigzag strip, a wire could be placed on the surface, as a more discrete disturbance.

2.4. Acoustic theory

2.4.1. Fundamentals of noise

Sound pressure level

Noise are the perturbations of pressures, these pressure fluctuations occur at various frequencies and humans are able to these pressure perturbations between a frequency range of $20\ Hz$ to $20\ kHz$. The larger the pressure fluctuation the higher the power of the sound. The intensity of the sound is often denoted by decibels (dB). This is a logarithmic scale that compares a standard pressure measurement of $20\ \mu Pa$, this is the lowest pressure difference that human hearing allows for [35]. The sound pressure level is a way of quantifying the ”loudness” off a given sound, and is calculated using the Equation 2.20.

$$\text{SPL} = 20\log_{10}\left(\frac{p_{\text{rms}}}{p_{\text{ref}}}\right) \tag{2.20}$$

Power spectral density

The sound pressure level takes the root mean square of a given sound. It does not include the frequency of the sound. To be able to identify the power of a noise over a range of frequencies, a Power spectral density can be used.

The Power Spectral Density (PSD) shows how the power of a signal is spread across different frequencies. Instead of looking at the signal over time, the PSD breaks the signal down to see which frequencies contain the most energy. In the calculation of the PSD a signal is broken up into its fundamental frequency components using the Fourier transform, after which each measured frequency is sorted into bins, containing a range of frequencies. For each of these bins the power is calculated. When this is done for all frequency bins the power of a range of frequencies can be plotted by analyzing the result of the PSD, and we can identify what the frequencies of interest are and see where the region of interest lies for a given sound measurement. The equation for the PSD is shown in Equation 2.21.

$$PSD(f) = \frac{1}{t|x(f)}|^2 \tag{2.21}$$

Third octave binning is a method used for the binning of frequencies like what is used for the calculation of PSD, in the method the size of the frequency bins is set to one third of an octave so where an octave is a dubbing of frequency, one third of an octave is $f_n = 2^{\frac{n}{3}}$. The midpoint of the frequency bin is positioned at the center of the third octave bin. As the frequency grows larger the width and thereby spacing of the frequency bins become larger on a logarithmic scale. Where the lower and upper are one sixth of the frequency bins. The reason for using a third-octave beam forming is that human hearing was roughly scaled logarithmically as the frequency increased. To correct for the ”loudness” of the a noise, the A-Weighted scaling can be used [35]. This scaling of power over frequencies adjusts for the sensitivity of human hearing to frequencies. The weighted scale and is shown in Figure 2.7, when this scaling is applied to the power over the frequencies the (dBa) unit is used to reflect the scaled loudness of the signal.

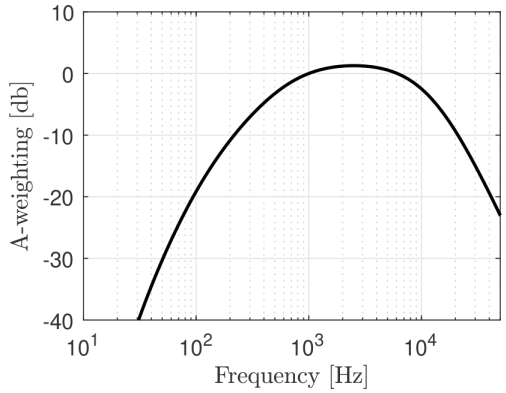

Figure 2.7: A-Weighting Scale [35]

Lighthill's aeroacoustic equation and wind turbine noise
The Lighthill equation provides an analogy to model the aeroacoustic impact of turbulent fluid motion. The equation is derived from the Navier-Stokes equation that was reformulated under several assumptions. The resulting equation results in a nonhomogeneous wave equation as shown in Equation 2.22.

$$\frac{\partial^2 \rho'}{\partial t^2} - a_0^2 \nabla^2 \rho' = \frac{\partial^2 T_{ij}}{\partial x_i \partial x_j} \tag{2.22}$$

Within the equation, the properties are constructed out of two components, the average component and the fluctuating component. An example is shown in Equation 2.23

$$\rho = \rho_\infty + \rho' \tag{2.23}$$

The Lighthill stress tensor T_{ij} represents the acoustic source and defined as shown in Equation 2.24.

$$T_{ij} = \rho u_i u_j + \left[(p - a_0^2 \rho) \delta_{ij} - \tau_{ij} \right] \tag{2.24}$$

For LEE, surface roughness causes the boundary layer to be disturbed, causing a transition into turbulence. The turbulence the velocity components $u_i u_j$ for $i \neq j$ and become greater. Unlike in laminar boundary layers, where there is very little to no vertical mixing in the boundary layer. In addition to this, the Lighthill stress tensor also includes the viscous stress tensor τ_{ij}, because of the surface roughness the viscous stress component will become larger, increasing the general acoustic source tensor strength at the location affected by the roughness. Although Lighthill's equation is exact, it is not practical to solve directly for wind turbine applications. It does show the importance of several factors that contribute to the noise generated. Curle's Aeroacoustic analogy solves the the Lighthill's equations using the Greens theorem and shows that dipole noise like turbulent boundary layer noise, scales proportional the the velocity to the 6th power. Quadrupole sources, like jet flow scale to the velocity to the eighth power and monopole sources, like combustion, scale to the fourth power [36].

2.4.2. Characterizing Numbers in Acoustics

Helmholtz resonance
When air flows inside of a cavity, the trapped air inside acts like a spring-like structure where the force of the flow pushes against the compressibility creating an oscillation in pressure. The frequency of these perturbations can be calculated using the Helmholtz resonance equation as shown in Equation 2.25 [23].

$$f_H = \frac{c}{2\pi} \sqrt{\frac{A}{V L_{\text{eff}}}} \tag{2.25}$$

In this study, Helmholtz resonance could occur if there are enclosed or semi-enclosed gaps, like pits or gouges. These act as cavities when exposed to flow, which might result in a tonal peak in the spectrum. While not the main focus, it is something to consider when analyzing unexpected narrow band noise components.

Strouhal
The Strouhal number is a dimensionless number that relates the frequency to a characteristic length and the flow velocity as shown in Equation 2.26. It can be used to provide information on the frequency at which a vortex or pressure fluctuation occurs [23].

$$\mathrm{St} = \frac{fx}{U} \tag{2.26}$$

For airfoils, the characteristic length x is usually the chord [37], the thickness of the airfoil, or the thickness of the trailing edge, in the case of the bluntness of the trailing edge.

2.4.3. Acoustic beamforming

Beamforming is a technique that uses multiple sensors to obtain the directionality of a signal. When multiple microphones are used, the direction from which a noise originates can be determined. For humans, our brain can determine this using the time delay between the sound reaching one ear compared the other.

Delay and sum time domain beamforming
In essence, this time delay is the basis for time-domain delay and sum beamforming. Delay and sum beamforming is a technique in which multiple microphones that are used to locate the origin of a noise source. The incoming sound wave is captured by the array of microphones, where the position of each microphone is known. Due to differences in distance between the microphones, pressure waves reaches them at different times. Using this, the position of a noise source can be determined.

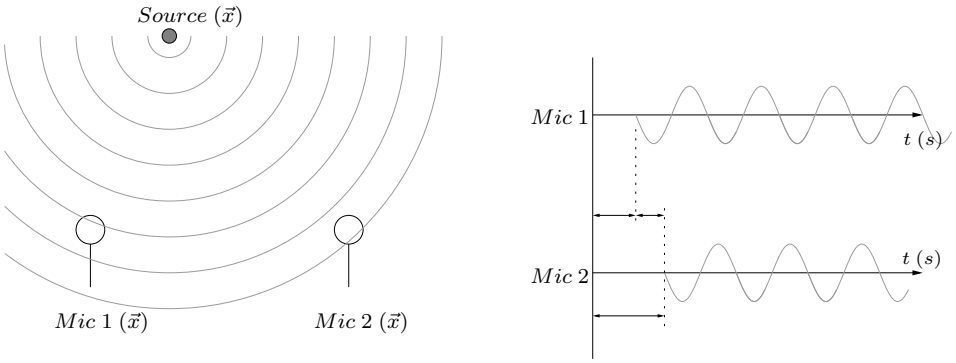

Figure 2.8: Visualization of the delay and sum principle

To find the location of a noise source, a search grid and steering vectors are required. The search grid consists of points in space where the sound is expected to originate from. The steering vector is a vector drawn from each microphone in the array to each point in the search grid. Each of these steering vectors has a specific magnitude; this is the distance. Knowing the distance between each search grid point and the microphones and the speed of sound, the time delay can be calculated between a search grid point and each microphone. Using this time delay, the microphone signals can then be shifted according to the search grid point. The closer the source originates from this point, the greater the constructive interference will be, and if the sound does not originate from that point, destructive interference will reduce the intensity of the signal. When this is done for the entire search grid, the origin of the noise can be located at the search grid point where the signal is most intense [23]. The resolution of the beamformer is (among other factors) determined by the number of points in the search grid that are analyzed. In the Figure 2.9a the search grid with 900 points is shown in Figure 2.9b and a beamformer with a search grid of 90 000 search grid points. For this image a single noise source was used, however, when there are multiple smaller noise sources and the amount of search grid points is lower and the sources are close together it could appear as a singular source when if in fact there could have been multiple.

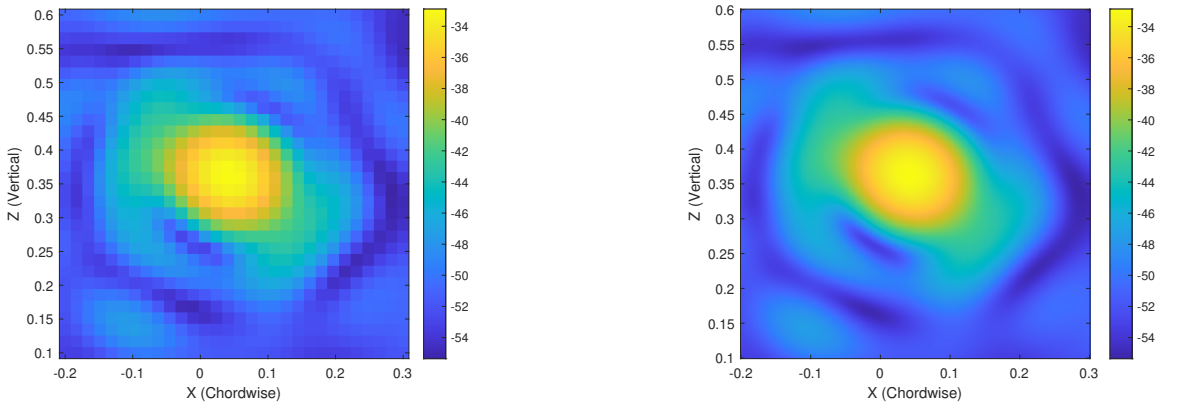

(a) Beamformer map using 900 search grid points

(b) Beamformer map using 90 000 search grid points

Figure 2.9: Effect search grid on sharpness of the beamformer

Steps time-domain delay and sum beamforming

1. Set up a searching grid.
2. Apply time delay to microphones based on position of microphone and the search grid position.
3. Sum the time corrected (delayed) time signal of each microphone to generate a map where the signal is most intense.

Mathematically, time domain beamforming can be described as shown in Equation 2.27. In this equation the beamformer output is calculated using the summation of the signal of the microphone $p_m(\vec{x}, t)$. Based on the difference in distance $|\vec{x} - \vec{x}_0|$ a shift in time for the signal is taken into account $t + t_0$ where $t_0 = \frac{|\vec{x}-\vec{x}_0|}{c}$ this shifts the signal to align with the ”base” microphone. The location of the search grids point is denoted by $\vec{x}_0$. The summation over all of the microphones creates constructive or destructive interference based on the location of the source. This is then numerically expressed over the number of microphones M. The 4π account for the spherical expansion of the pressure waves [38].

$$L(t, \vec{x}_0) = \frac{4\pi}{M} \sum_{m=1}^{M} p_m(\vec{x}_0, t + t_0) \, |\vec{x} - \vec{x}_0| \tag{2.27}$$

Sum and delay frequency domain

Sum and delay Frequency domain beamforming uses the same techniques as in time domain based delay and sum beamforming, by adjusting the signal for the time it takes for a noise to complete its propagation path to the microphone; however, it happens in the frequency domain. In the frequency domain, beamforming the temporal data from the microphones is converted to the frequency domain using the Fourier transform. Here, the microphone signals are split up into different frequencies. Time domain beamforming is easier to calculate; however, frequency domain beamforming offers more options for postprocessing and analysis, and is therefore often chosen over time domain beamforming. Frequency domain beamforming allows us to look at specific frequencies of sound whilst ignoring all others. Where in time domain beamforming a time delay is introduced to compensate for the different search grid and microphone positions, in frequency domain beamforming a phase shift is introduced (the delay). By summing the parts of the phase shifted data are then summed together and constructive or destructive interference provides a map of the search grid where the noise at that frequency is closest to [38].

Steps frequency domain delay and sum beamforming

1. `Segment Data`
   Segment the temporal data into blocks, optionally an overlap can be introduced.
2. `Window Function`
   Apply windowing function to the segmented data
3. `Fourier transform`
   Transform the data into the frequency domain using the Fourier transform to the segmented windowed data.
4. `Search Grid`
   Define search grid from which noise is expected to originate.
5. `Steering Vector`
   Based on the distance between microphone positions and the locations of the search grid, a steering vector can be calculated that accounts for phase sifting due to distance and time delay.

Mathematically, conventional frequency domain beamforming is given by Equation 2.28. In Appendix B a more thorough explanation and derivation of frequency domain beamforming is shown.

$$Z_{j,k} = \sum_{m=1}^{M} w_m \, \tilde{p}_{m,k} \, e^{-i\omega_k \tau_{j,m}} \tag{2.28}$$

Fourier transformation The Fourier transformation is a mathematical tool that can convert any temporal signal into the frequency domain. Any random signal can be decomposed into components of sine and cosine. by doing so the frequency corresponding to each of the sine and cosine pairs can be extracted. The idea here is to divide the signal into separate frequencies [39].

Block For analysis of larger signals, a common technique used is splitting the data into blocks; this allows for a more efficient Fourier transfer in post-processing. In addition to this, splitting the signal into blocks allows the use of a windowing function and overlap. Another aspect is that by splitting the total signal into shorter blocks, the amount of noise in the signal is reduced. The drawback of having small blocks is that lower frequencies cannot be detected as the size of the block does not match the frequency period.

Window function A window function is applied before performing a Fourier transform. Most window functions scales the data at the edges where the signal gets reduced in amplitude. The goal here is to minimize the discontinuous signals, which in turn reduces the spectral leakage; this is where some power from a different frequency seeps into another frequency, hence leaking over. This happens when a part of a signal is taken and then a Fourier transform is taken, in a measurement there is a finite number of data measured, so at the start the measurement part of an frequency part of a frequency component in the signal may be cut off, the use of a window reduces this. The drawback of this is that the amplitude in the signal are reduced at the edges. The choice of window function (Hamming, Hanning, Gausian, etc.) effects the trade-off between main lobe width (frequency resolution) and side lobe level (leakage). The Hanning and Hamming window attempt to balance frequency resolution with leakage [39].

Overlap When the signal is divided into blocks prior to the Fourier analysis, overlapping the blocks can be used to reduce the signal loss caused by the windowing. As the window function reduces the beginning and end of each block, reducing the magnitude to minimize spectral leakage. This reduction can suppress other parts of the signal. By overlapping blocks such that each part of the signal is covered by multiple windows [39].

Nyquist frequency When data from a microphone is converted from the time domain to the frequency domain, there is a limit to the highest frequency that can be accurately measured. This limit is called the Nyquist frequency and is equal to half of the sampling frequency. If a signal contains frequency components higher than the Nyquist frequency, they cannot be correctly measured and will be misinterpreted as lower frequencies; this phenomenon is known as aliasing. This makes it impossible to distinguish between the true frequency and its aliased counterpart(s) [38].

Cross spectral matrix The Cross Spectral Matrix (CSM) is a tool used in signal analysis where multiple sensors are used, like in beamforming where there are several microphones present. The CSM shows how the signals from the different sensors compare to each other in the frequency domain. This comparison between the different signals is made by calculating the cross-power spectral density between each pair of signals, which captures both how similar their frequency content is and how their phases are aligned, creating either constructive or destructive interference. Similarly to the time-domain beamforming, the delay can also be introduced into the CSM. By adding a phase sift to each element of the CSM the signal of the microphones can be compensated for their position [40].

Steering vector The steering vector is the part that introduces the phase shift onto the CSM. Unlike the time domain beamforming where a set amount of time is added to each of the microphone signal the phase shift does this in the frequency domain. The steering vector uses the position of the search grid and the position of the microphone to calculate the time it takes for the signal to propagate and based on the frequency a phase shift is introduced. In essence, a phase sift changes the starting point where a frequency signal starts. For example, normally a sine wave would start at 0 and return to this original point after one wave length. Now because the signals come in at a different time the starting angle of the sine wave (the phase) needs to be adjusted for this time delay [38].

Advanced beamforming algorithms
To improve the accuracy of beamforming, more advanced algorithms have been developed. DAMAS and CLEAN are some of the most widely used algorithms to improve the beamforming map. DAMAS is a de convoluting algorithm where the goal is to localize the peaks of the sound sources and it aims to reduce the effect of the side lobes, resulting in a cleaner beamforming map [35]. The CLEAN algorithm searches for the most intense sound source, after this the sound source is then virtually removed and the next loudest sound source is located. Then these iterations are repeated until a certain minimum peak value is reached [35].

2.5. Wind turbine aerodynamics

2.5.1. Blade element geometry

For understanding the aerodynamics of a wind turbine blade, the flow and blade geometry needs to be understood. The velocity components and the angles of a blade element are shown in Figure 2.10.

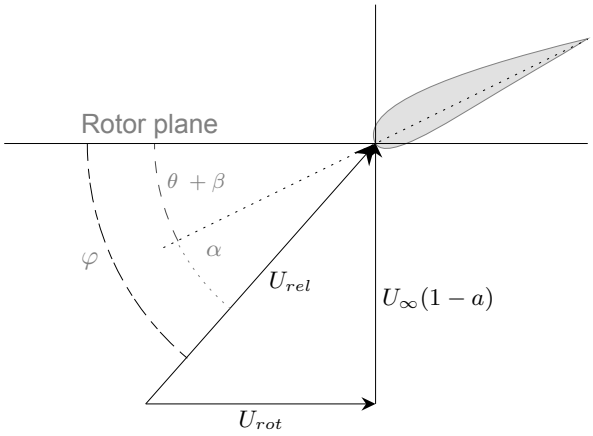

Figure 2.10: Angles and velocity components for a blade element adapted from [41]

Flow angles

- φ: *Inflow angle*, this is the angle between the relative wind velocity and the rotor plane.
- θ_t: *Twist angle*, this is that angle of the blade section relative to the root of the wind turbine blade
- β: *Pitch angle*, this is that angle of the turbine blade relative to the hub, this angle is able to be adjusted based on the wind condition.
- α: *Angle of Attack*, this is the angle between the cord line of the airfoil with respect to the relative wind speed.

Velocity components

- $U_\infty(1-a)$ This is the effective wind speed over the rotor disk area of the wind turbine and is dependent on the freestream velocity.
- U_{rot}; This is the rotational component of the velocity, due to the rotation of the turbine the flow
- U_{rel}; This is the combined relative velocity of both the freestream velocity and velocity as a result of the rotation of the wind turbine.

2.6. Wind tunnel aerodynamics

2.6.1. Shear layer effects

The wind tunnel facility at the University of Twente is a closed-loop wind tunnel with an open test section; this test section is an anechoic chamber. This is an open room where the velocity of the flow is stationary, the flow through the test section has a certain velocity. Similarly to the boundary layer where the moving flow interacts with a solid wall, a shear layer is the interaction between the moving flow in the open test section and the stationary air in the anechoic chamber.

Acoustic propagation through shear layer

When an acoustic source is positioned in the wind tunnel the noise is carried away by the flow. The shear layer, causes pressure perturbations introducing uncertainties into the acoustic measurements. J. Biesheuvel [42] investigated this effect and found that the shear layer does hamper the localization of a sound source, due to the distorting effects in the shear layer that alter the propagation path of the sound waves.

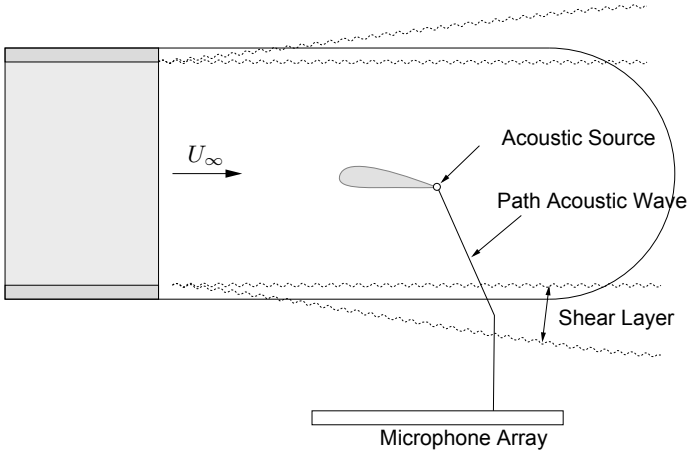

Figure 2.11: Acoustic wave propagation though shear layer

2.6.2. Wind tunnel corrections

Even though the goal of a wind tunnel is to simulate real world conditions, the flow in the wind tunnel does not match the real world free stream flow conditions. One of the ways in which the flow in the wind tunnel varies from that in the real world is that the flow is bounded by walls of the wind tunnel, where as in the real world the flow is unbounded. The airfoil itself creates a pressure distribution; this pressure distribution sucks the flow on one side of the airfoil and pushes it away on the other side of the foil. This results in a bending effect on the flow in the wind tunnel. In the real world, the flow field extends far beyond the limited stream of the wind tunnel. These effects alter the effective angle of attack and the shape of the camber, affecting the lift and pressure distribution. To compare wind tunnel measurements with theoretical predictions or free-stream behavior as seen in operating conditions, corrections must be made. Brooks et al. [28] describes a correction for the difference between unbounded flow in the real world conditions and the bounded flow in the wind tunnel. To correct for the angles in the wind tunnel as shown in the Equation 2.29, the lift and drag coefficients for the measurements in the wind tunnel are required.

$$\alpha = \alpha_t - \frac{\sqrt{3\sigma}}{\pi} c_{\ell t} - \frac{2\sigma}{\pi} c_{\ell t} - \frac{\sigma}{\pi}\left(4 c_{m_{\frac{1}{4}t}}\right) \tag{2.29}$$

2.7. Airfoil self noise

When a flow moves over an object, noise is generated as the object interacts with the flow. The noise that is generated is called (airfoil) self noise. The types of noise that can be generated have been described by Wolfe et al. [37] into five categories. In this section we will discuss these five classifications of self noise.

1 - Turbulent boundary layer-trailing edge noise

One of the major contributors to the broadband noise that an airfoil produces is the turbulent boundary layer–trailing edge (TBL-TE). The cause of this noise, as the name might suggest, is the interaction between the turbulent boundary layer and the trailing edge of the airfoil. The turbulent boundary layer consists of chaotic flow structures, and as this leaves the surface of the airfoil, the scattering of these structures causes pressure perturbations that are perceived as noise.

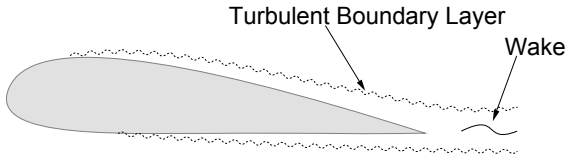

Figure 2.12: Illustration of Turbulent Boundary Layer Trailing Edge Interaction

2 - Laminar boundary layer-vortex shedding noise

The Laminar Boundary Layer-Vortex Shedding (LBL-VS) noise is a tonal noise that occurs when the instabilities within a laminar boundary layer causes vortex shedding at the trailing edge of the airfoil.

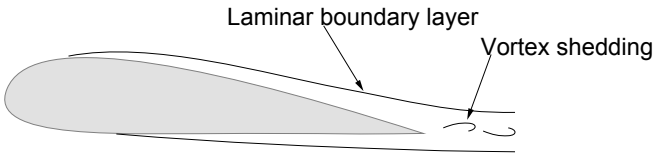

Figure 2.13: Illustration of Laminar Boundary Layer Vortex shedding

3 - Separation/stall noise

When the angle of attack becomes so great that the boundary layer is unable to adhere to the surface of the airfoil the boundary layer will separate form the airfoil itself. This occurs mainly on the suction side of the airfoil. When this occur near the trailing edge the sound presents itself as trailing edge noise. However when deep stall is achieved, meaning the separation occurs closer to the leading edge of the airfoil. Large turbulent structures form, due to the side of the eddies the frequency of this noise is relatively low.

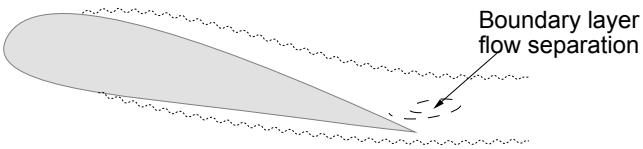

Figure 2.14: Illustration of stall occurring close to the trailing edge of the airfoil

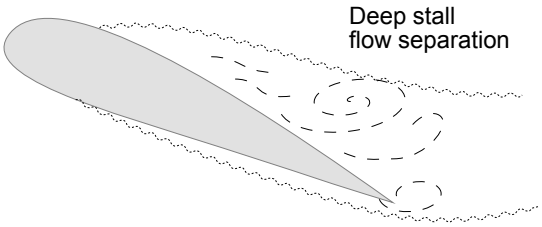

Figure 2.15: Illustration of stall occurring close to the leading edge of the airfoil (Deep Stall)

4 - Trailing edge bluntness vortex shedding noise
The Trailing Edge Bluntness Vortex Shedding Noise (TEB-VS) is caused by vortex shedding at the trailing edge of the airfoil caused by the blunt shape of the airfoil itself. Due to this shape an unstable shear layer is created between the suction and pressure side of the airfoil. This generally occurs when the thickness of the trailing edge is larger than the boundary layer displacement thickness.

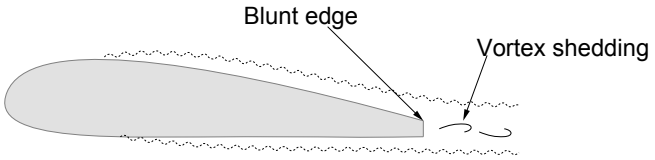

Figure 2.16: Illustration of trailing edge bluntness vortex shedding

5 - Tip vortex noise
The tip vortex noise is caused by the vortexes that are created at the tip of the airfoil where the lower pressure on the suction side and the higher pressure on the lower side of the airfoil interact with each other causing a vortex to form, resulting in noise.

Figure 2.17: Illustration of tip vortex formation

2.7.1. Effect surface roughness on airfoil noise
The surface roughness at the leading edge of the airfoil is sufficient enough the boundary layer transition from laminar to turbulent earlier. The laminar boundary layer vortex shedding noise is effectively eliminated by this transition and turbulent boundary later trailing edge noise forms. As a result of the increased mixing in the turbulent boundary layer, the boundary layer is more resistant to adverse pressure gradients and therefore less prone to separation and will adhere longer to the surface of the airfoil. This delays stall to higher angles of attack and or moves it further down the chord length of the airfoil.

2.7.2. Cavity noise
Helmholtz resonance for impinging flow
When a jet of air impinges directly onto the opening of a Helmholtz resonator cavity This impinging flow reduces the effective neck length of the resonator typically to about 30–60% [43]. The equation for the resonant frequency is show in Equation 2.25.

Rossiter formula for grazing cavity flow
The characteristic frequency of pressure oscillations in a grazing cavity flow can be estimated using the Rossiter formula. This formula is used to predict oscillation frequencies that can appear when a boundary layer flows over a cavity as in the case of the P and PG erosion model. The expression is given in Equation 2.30 [44]:

$$St = \frac{fL}{U} = \frac{n - \phi}{\frac{1}{K} + \frac{M}{\sqrt{1 + \frac{(\gamma - 1)}{2} M^2}}} \tag{2.30}$$

3

Literature review

3.1. Leading edge erosion

In this chapter the leading edge erosion as described and quantified in previous papers are discussed. In the chapter the stages of the erosion and their classification are discussed as well as the coverage, dimensions and quantity of the erosion features. Besides this, we will look into the scaling of the erosion features has been done in previous experiments.

3.1.1. Classification of erosion

LEE on wind turbine blades initially starts as small pits on the leading edge, and over time these develop into larger pits eventually turning into gouges. This form of erosion only affects the protective coating often found on the leading edge of turbine blades. Further stages of erosion cause the coating layer to erode away damaging the underlying laminate structure of the turbine blade. The severity of this erosion is often described in several stages. Table 3.1 provides an description of how different sources classify these stages of erosion.

Erosion stage	**IEA Wind** [2]	**Gaudern** [45]	**Sareen** [46]
Stage 1	Light pitting of coating	Small pinholes of missing paint distributed across LE with some grouping.	Pits
Stage 2	Small patches of missing coating	Pinholes have coalesced into larger eroded patches.	Pits + Gouges
Stage 3	Large patches of missing coating	Affected area has increased, with isolated larger patches with a greater depth.	Delamination
Stage 4	Erosion of laminate	Patches have coalesced further, and depth has increased.	Delamination+
Stage 5	Complete loss of laminate	Large areas of LE laminate exposed.	Delamination++

Table 3.1: Erosion severity stages as described in various papers

3.1.2. Quantity

The most comprehensive description of the quantity especially for the pits and gouges on the laminate is provided by Sareen et al. [46], where measurements provided by 3M, a supplier of leading edge protection tapes are shared. The data is shown in Table 3.2. The quantity of the defects are based on a 851 mm section in spanwise direction.

Erosion Stage	Pits, Gouges & Delamination
Stage 1	100P
Stage 2	200P / 100G
Stage 3	400P / 200G / DL
Stage 4	800P / 400G / DL^{+}
Stage 5	1600P / 800G / DL^{++}

Table 3.2: Quantity of defects in various stages of leading edge erosion [46]

Gaudern [45] does not describe the quantity of the erosion features as a function of the span, instead several damage patters are constructed for a span wise section of the leading edge. This pattern was designed for a 730 mm span section. The pattern is not a repeating pattern and has a random distribution, because of the erosion features being modified, the pattern is not able to be scaled directly, and a new similar pattern would have to be made when a different airfoil or span is utilized in similar experiments.

3.1.3. Coverage

In previous papers the coverage of the erosion features of the leading edge varies from 3 up to 15 % of the chord length centered around the leading edge of the airfoil [3], [45]–[47]. This was dependent on the stage of the erosion features on the leading edge and the type of airfoil. In real world conditions, it has been observed that the distribution between the upper and lower damage has the ratio 1:1.3 [2]. The coverage of the LEE is highly dependent on the shape and orientation of the leading edge of the airfoil as it dictates the angle of impact.

3.1.4. Depth erosion feature

In Table 3.3 the depth of various features of erosion at the leading edge is shown as described in the articles by Gaudern, Sareen, and Maniaci.

Erosion Type	**Gaudern** [45]	**Sareen** [46]	**Maniaci** [2]
Pits depth (mm)	0.1–0.2	0.51	0.1
Gouges depth (mm)	0.3–0.5	2.54	0.14
Delamination depth (mm)	0.8–1.2	3.81	0.59

Table 3.3: Depths in mm of LEE features as described by various authors

Dimensions Sareen

In the experiment carried out by Sareen et al. [46], the depth of the erosion features was not scaled based on the wind tunnel conditions relative to the real word conditions. Measurements for the study were derived from photographs capturing the eroded leading edges of wind turbine blades. For the pits and gouge erosion features the depth of the features was set equal to the diameter of the erosion features. The delamination feature was modeled by a relatively straight line with gentle slopes in the spanwise direction.

Dimensions Gaudern

In the paper by Guadern [45] LEE was measured on a used blade provided by Vestas. In the experiment, a method to scale the depth was proposed using the roughness height Reynolds number Re_k. However, to obtain the value for $u(k)$ several assumptions where made. We will now go over the processes how the value for Re_k was acquired in the paper. To estimate the value of $u(k)$ the wall shear stress is used as shown in Equation 3.1.

$$\tau_w = \mu(\frac{\partial u}{\partial y}) \tag{3.1}$$

To determine the values for the wall shear stress coefficient τ_w, XFOIL was used to analyze the airfoil for both operational conditions and wind tunnel conditions at various Re_c . The XFOIL analysis provided the friction coefficient over the surface of the airfoil. The wall shear stress can be calculated using the Equation 3.2.

$$\tau_w = C_f \frac{1}{2} \rho U_\infty^2 \tag{3.2}$$

Using the calculated value of the wall shear stress, the slope $\frac{du}{dy}$ is used to estimate the components of the velocity in the boundary layer as a function of height y. This assumes that the velocity profile in the boundary layer increases linearly as a function of height. From this equation, we see that the gradient of the boundary layer is dependent on the wall shear stress. The velocity gradient in the boundary layer is represented by the term $(\frac{\partial u}{\partial y})$, this term will increase as the wall shear stress decreases. Integrating the equation by the height of k we get:

$$\tau_w = \mu \frac{u(k)}{k} \rightarrow u(k) = \frac{\tau_w k}{\mu} \tag{3.3}$$

Then, taking the formula for the roughness height Reynolds number and filling in for the length scale k and the velocity $u(k)$, Re_k can be rewritten into the term τ_w.

$$Re_k = \frac{\rho \tau_w k^2}{\mu^2} \tag{3.4}$$

Because density ρ and viscosity μ are approximately the same in the wind tunnel as under operating conditions, and the model for the airfoil is limited in size and the wind tunnel is limited in velocity, the wall shear stress τ_w cannot be altered to match the value in real-world operating conditions. Therefore, the roughness height k must be altered. By excluding the constant variables, the relationship is derived as indicated by Equation 3.5.

$$(\tau_w k^2)_{Real-world} = (\tau_w k^2)_{Wind\ tunnel} \tag{3.5}$$

The assumption of a linear boundary layer does work for small defects that are well within the viscous sub-layer of the boundary layer where the velocity gradient is linear. The problem in this paper is that the defects not only reach beyond this viscous sub layer where the velocity components roughly follow the initial velocity gradient, but also extend above the thickness of the boundary layer, even for the lowest roughness height k. Therefore, the estimated $u(k)$ is significantly higher than the actual present. This approximation is shown in Figure 3.1

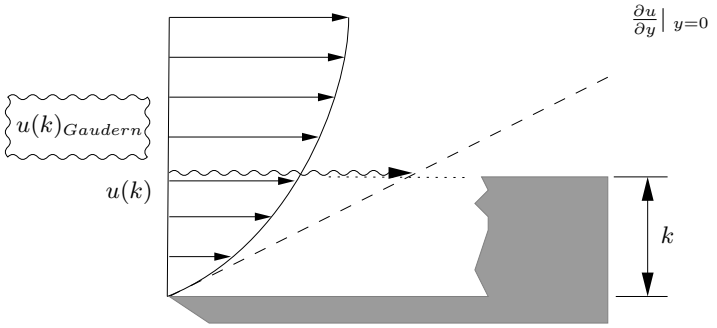

Figure 3.1: Illustration of linear approximation boundary layer to determine $u(k)$

In the paper, the operational conditions had a chord-based Reynolds number of $Re_c = 3 \times 10^6$ and the test condition was performed at $Re_c = 2.2 \times 10^6$. These conditions are relatively close to each other compared to the conditions that this study focuses on. As a result, the scaled depth and the depth in the operational conditions are similar to each other. The values for the $u(k)$ calculated using this linear approximation were both wrong, but due to the relative similarity between the Reynolds numbers, the error was limited.

Dimensions Maniaci
Similar to the Guardern, the depths of the erosion features were scaled using the dimensionless roughness Reynolds number. However, unlike the method proposed in the paper by Gaudern, the boundary layer was not approximated to be linear, but a CFD model was used to get the data from the boundary layer. Using this data the roughness Reynolds number was calculated [2]. The simulation could be performed under the operating conditions of the wind turbine, scaling is not a factor.

3.1.5. Mass loss
To determine the size and depth of the features of LEE, the IEA Wind has proposed modeling LEE based on mass loss of the coating and the laminate layer. The depth or thickness of the layers is not specified, but a percentage of mass loss is given per stage of LEE; this is presented in the Table 3.4.

Erosion Class	Description	Coating Mass Loss	Laminate Mass Loss
Stage 1	Light pitting of coating	<10%	0%
Stage 2	Small patches of missing coating	10%–50%	0%
Stage 3	Large patches of missing coating	50%–100%	<10%
Stage 4	Erosion of laminate	100%	10%–100%
Stage 5	Complete loss of laminate	100%	100%

Table 3.4: Erosion class definitions with associated coating and laminate mass loss [2]

3.2. Operating conditions NREL 5MW reference turbine
For the analysis of LEE on wind turbine blades specifications and operating conditions of a wind turbine are required. In this section, the turbine selected as the foundation for the analysis will be examined, along with an description of the real-world operating conditions.

3.2.1. NREL reference turbine
To analyze the operational conditions of a wind turbine, the NREL 5 MW reference wind turbine is used. This turbine is similar in size and operation to modern wind turbines. The reference turbine is, as its name implies, commonly used in research as a reference. While this turbine is not a commercially available model, the technical specifications required for research are often inaccessible for widely used commercial turbines. The NREL wind turbine model provides extensive technical data, facilitating the standardization necessary for others to use these results in comparative studies. The employment of commonly used airfoils further aids in the investigation. This turbine has also been successfully scaled to a 10 MW variant by DTU [48]. The basic specifications for the NREL reference turbine are presented in Table 3.5. There are certain limitations to the NREL 5 MW reference turbine; specifically, it is relatively large in size for the power it produces, compared to modern commercial wind turbines, which for a similar size are capable of generating more energy.

Property	Magnitude	Unit
Rated Power	5	MW
Rotor, Hub Diamater	126, 3	m
Cut-in, Rated, Cut-out windspeed	3, 11.4, 25	m/s
Cut-in, Rated rotational speed	6.9, 12.1	RPM

Table 3.5: Basic Specification NREL 5MW reference wind turbine [49]

3.2.2. Blade geometry

In addition to the basic information, the length of the chord and the twist angle as a function of the radial position of the blade are shown in Figure 3.2a. What should be noted is that the airfoil varies over the blade span and for the first 8.33 m or $r/R = 0.13$, the turbine has a circular airfoil. The data provides an angle of twist of the circular airfoil even though this has no effect. The wind turbine blade is designed to have optimal lift-to-drag coefficients for the entire blade; therefore, the twist angle along the radius is altered because the effective inflow angle is a combination of velocity U and rotational velocity, the twist and pitch angle of the blade corrected for this. Figure 3.2 shows these angles over the span and for various wind speeds.

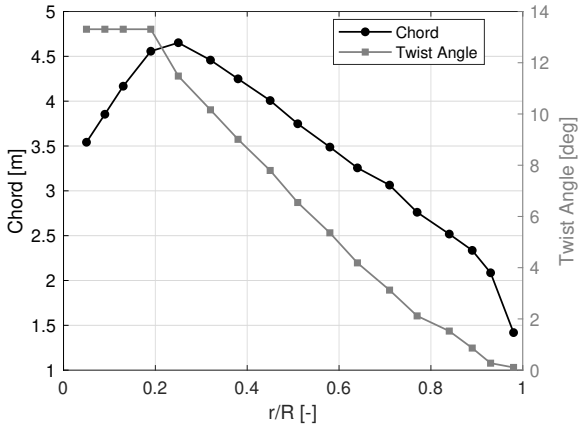

(a) Chord and Twist for the radial position of the blade for the NREL 5MW reference turbine

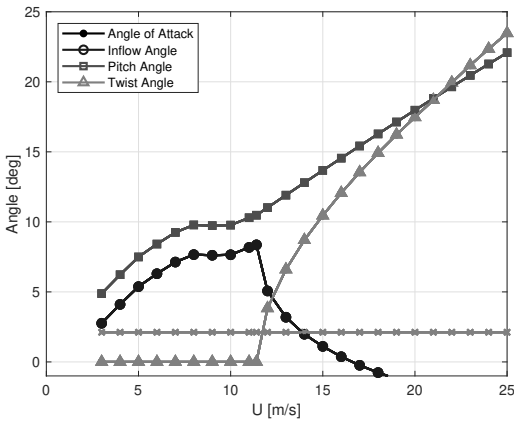

(b) Angles over the wind speeds for blade section at r/R=0.89

Figure 3.2: Angles over the span of the turbine blade under varying wind speeds

3.2.3. Section of interest

For a given wind turbine blade, the noise produced is shown in Figure 3.3. As can be seen in the figure, the outer section of the wind turbine blade produces the most noise. The radial position of this section is where the acoustic effects heights are approximately at $r/R = 0.9$. The specification for this section of the reference wind turbine is shown in Table 3.6. The rated wind speed is taken because this is where the wind turbine was designed. Here, the standard atmosphere conditions are taken for dry air at $20\ C°$ [22].

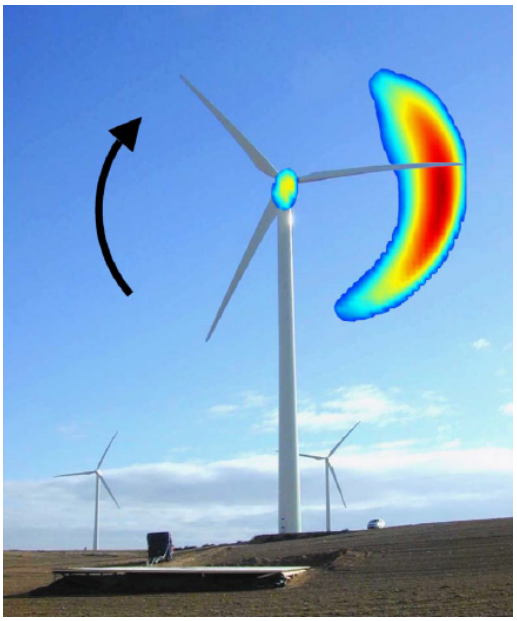

Figure 3.3: Acoustic beam forming image of an wind turbine [50]

Parameter	Value	Unit
Airfoil	NACA 64-618	
Radial position (r/R)	0.89	(-)
Angle of attack	8.8	(°)
Reynolds number	11350900	(-)
Wind speed	71.8	(m/s)

Table 3.6: Specification NREL 5MW reference wind turbine at r/R=0.89 [49]

3.2.4. Properties of the turbine in span wise direction

Reynolds number development in spanwise direction of the turbine blade

In Figure 3.4a the Reynolds number of the blade element is shown, in Figure 3.4b, the Reynolds number of the blade element over the radial position between the cut-in-, rated- and cut-out wind speed are shown.

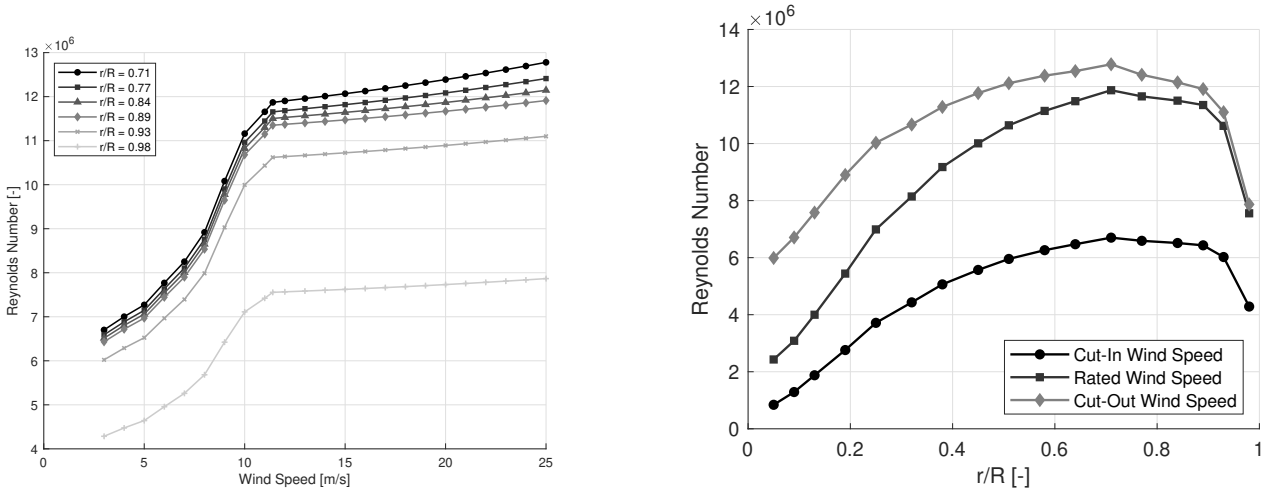

(a) Reynolds number as a function of wind speed for multiple radial positions

(b) Reynolds number for the blade sections at three wind speeds

Figure 3.4: Chord based Reynolds number for various conditions and radial positions of the wind turbine blade

3.3. Modeling roughness in literature

Surface roughness plays an important role in the development and behavior of the boundary layer. The surface defects behave like roughness as a result of LEE. However, unlike most roughness discussed in the field of fluid dynamics, LEE is not a continuous roughness as seen in pipe flow. The surfaces on which the flow interacts and develop LEE are irregular and worsen over time. In this chapter, we will discuss how surface roughness and erosion has been modeled in previous studies. The goal is to asses the possibilities, methods and limitations for the modeling of LEE.

3.3.1. Equivalent sand grain roughness

The equivalent sand grain roughness as introduced in Section 2.2.1 can be used to model the roughness. In experimental setups, a practical approach to simulate roughness is by using sandpaper as it is easy to obtain and comes in standardized grades. Adams et al. [21] investigated the correlation between the grain size of different sandpaper grades and the equivalent sand grain roughness k_s.

To improve the estimation of k_s, Adams et al. [21] proposed an algorithm that converts commonly used surface roughness parameters (R_a, R_{rms}, R_{zd}) into an equivalent sand grain roughness. A surface was modeled with equally sized spheres and calculated k_s values, which were then validated using experimental flow data.

Among the parameters studied, R_{zd} showed the strongest correlation with k_s, while R_a performed poorly in capturing the aerodynamic effect of roughness.

To validate this method, surface measurements were taken on a variety of materials. The measured roughness parameters were used in the conversion algorithm to estimate k_s, and these were compared against experimentally determined roughness values. The results showed that R_a while frequently used in industry did not reliably estimate the aerodynamic impact of the surface. In contrast, R_{zd} produced estimates that were much closer to the flow behavior.

Although the equivalent sand grain roughness has been used in rotor applications such as axial compressors [8], it is still a simplified model. The idea assumes a uniform and evenly distributed roughness, which is rarely the case in reality. Real erosion features such as pits, gouges, or delamination tend to be more randomly distributed and decrease in severity based on the location and are much more difficult to model accurately.

While k_s is a practical and commonly used way to quantify the effects of roughness, it does not always reflect real world conditions. Especially for complex geometries, such as the leading edge of a turbine blade.

A comparison can be made between real surface topologies and the simplified equivalent sand grain model. As shown in Figure 3.5, real surface features tend to be more irregular and complex, and are not always accurately captured by uniform sphere models.

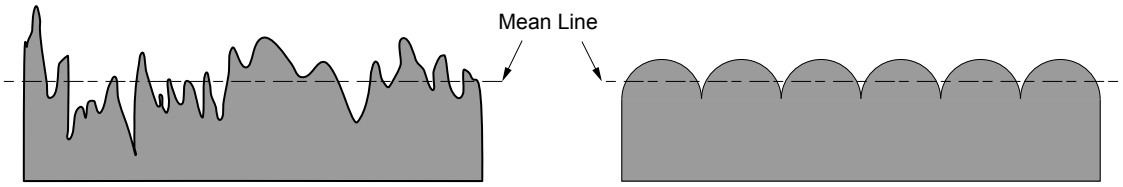

Figure 3.5: Real roughness vs theoretically sand grain roughness

3.3.2. Positive and negative erosion modeling

LEE, especially in early stages, is somewhat evenly distributed and could therefore be modeled by a distributed roughness like sandpaper. In the severe case of LEE, particularly during advanced stages such as delamination, alterations to the surface are unevenly distributed as singular defects. Therefore, the application of sand paper or a mesh where the roughness is a constantly distributed roughness is ideal to model LEE.
Additionally, by applying a sand paper-like material such as Zig-Zag tape or a mesh, the modeled surface roughness is a positive roughness. However, the LEE can be negative roughness features. When the roughness either positive or negative is constant, the difference is physically somewhat similar; however, for LEE this is not the case. In Figure 3.6, the difference between the negative erosion and positive erosion is depicted.

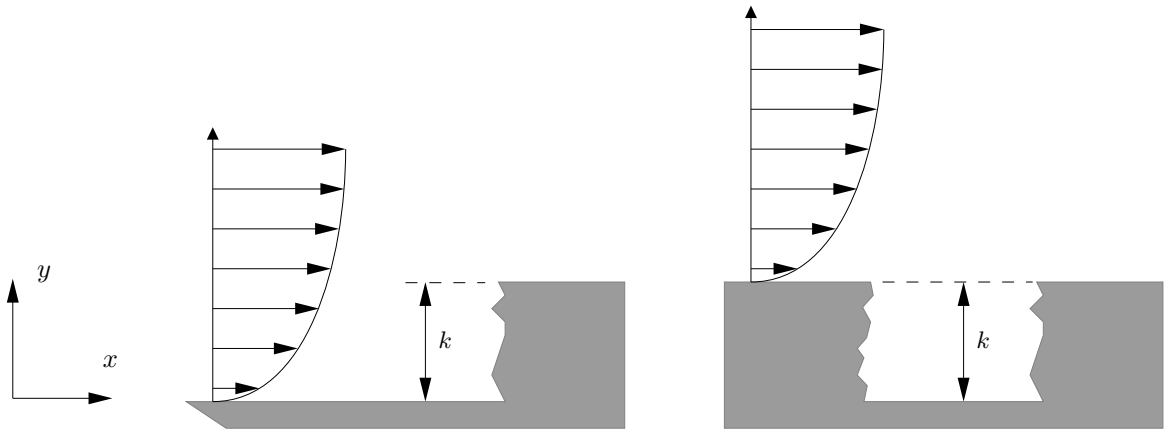

Figure 3.6: Boundary layer encountering positive and negative erosion

3.3.3. Zig-Zag tape

The hypothesis is that the LEE, especially in severe stages, effects the boundary layer and causes transition. Zig-Zag strips are a common way to trip the boundary layer and could be used to simulate the effect of LEE. In a previous experiment by Gutiérrez et al. [51], Zig-Zag strips have been used to trip the boundary layer and emulate the effect of LEE; however, these are designed to intentionally trip the boundary layer. However, in this paper, the goal is to investigate if the boundary layer is tripped by the LEE that will present itself as trailing edge noise. This approach will not prove the hypothesis, as the goal is to see what the various stages of erosion do to the boundary layer and the aeroacoustic effect. This approach would only show the aeroacoustic effect of a turbulent boundary layer, not the effect of erosion.

3.3.4. Real erosion modeling

To simulate the erosion of the leading edge, a Rain Erosion Test (RET) facility was constructed by DTU to realistically evaluate the effect of rain on the erosion of the leading edge in a wind turbine blade [52]. To do this, a blade profile is rotated at high speeds and water droplets are dropped in the same axis where the blade rotates to simulate rainfall. The impact of these water droplets causes LEE to occur. By increasing the amount of rain and the tip velocity by up to 224 m/s, the erosion development can be carried out in a short time. This method would be the most realistic process to model the LEE; however, the problem here is that the scale of the defects might not correspond to what is seen in real life given the conditions of the wind tunnel. That is, the erosion caused by the RET might result in the same size defect, as the impact conditions and materials do not match the physical scale of the airfoil model.

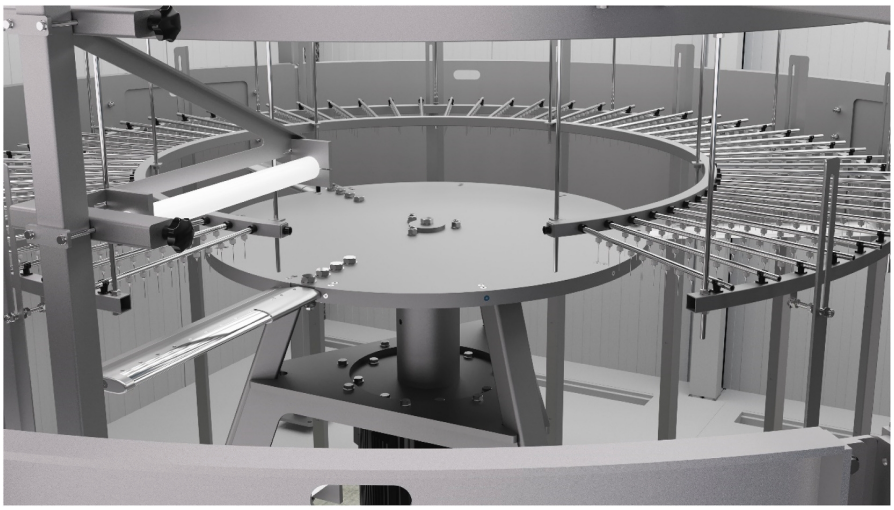

Figure 3.7: The Rain Erosion Test (RET) setup at DTU [52]

3.4. Wind tunnel experiment DU97-W-300

3.4.1. Correction angle

As described in an earlier part of the report, the real-world conditions do not match that in the wind tunnel, and therefore corrections need to be made to account for the angle in the wind tunnel [23]. Y. de Valk [53] studied the DU97-W-300 airfoil for his master thesis in the open test section of the wind tunnel facility at the University of Twente. In his thesis, the aerodynamic performance of the airfoil was extensively described. The thesis used the correction as described by Brooks [23]. Figure 3.8 shows the data of the experiments by Y. de Valk [53], added to this data is an XFOIL simulation of preformed at the measured Re_c and at the calculated effective angle. What can be seen is that the XFOIL simulation and the measured data seem to correlate to each other in the linear section of the graph.

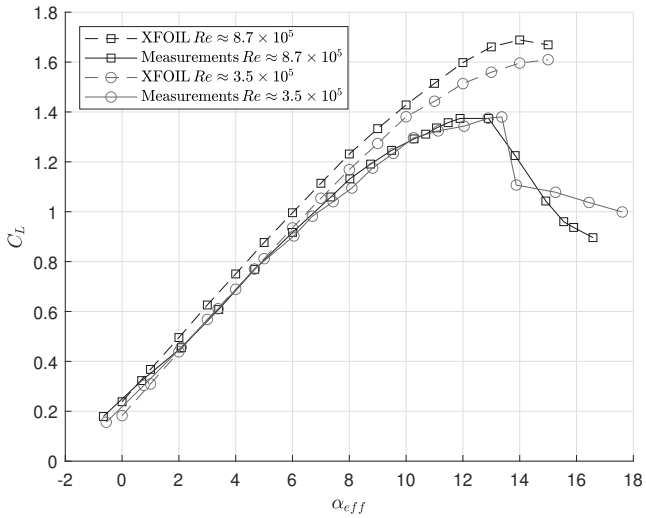

Figure 3.8: Lift coefficient over angle of attack using data from Y. de Valk [53]

Table 3.7 shows the points and Reynolds numbers where the maximum coefficient of lift to drag occurred in the University of Twente aeroacoustic wind tunnel facility using the DU97-W-300 airfoil.

$Re_{c\ wt}$	α_{eff}	α_{wt}	$\frac{C_l}{C_{d\ max}}$
869795	8.02	13	77.88
350610	10.26	16	52.46

Table 3.7: Angle of attack at $\frac{C_l}{C_{d\ max}}$ for both Reynolds numbers for the DU97-W-300 airfoil [53]

Part II

Experimental design and data acquisition methods

4

Experimental setup

To model the effects of LEE damaging airfoil and allowing for evaluation of the effects of various stages of LEE a simplified approach is taken; in this chapter the models for the LEE are described. In addition to this, the setup of the measurement equipment is discussed.

4.1. Wind tunnel facility

The wind tunnel facility at the University of Twente is an aeroacoustic closed-loop wind tunnel and consists of several sections. In this part of the report we will discuss some of these sections.

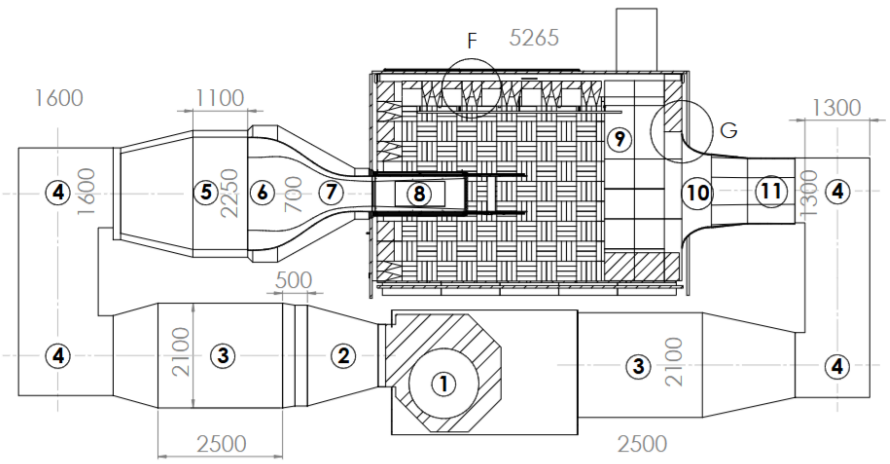

Figure 4.1: Setup of the Aeroacoustic wind tunnel at the University of Twente [54]

Control

For this experiment, the wind tunnel was controlled using a LabVIEW program. The program controls the speed of the motor located in the basement of the facility. The control of the wind tunnel is limited to the motor power as a percentage with increments of 0.5 %.

Anechoic chamber

The test sections are located in an anechoic chamber; in this chamber, the goal is to absorb most of the noise generated within the test section and minimize the reflection of sound produced of objects within the wind tunnel. To achieve this, the anechoic chamber is fitted with acoustic absorbent materials that absorb the sound waves and reflect them into itself using wedge-shaped blocks. Thereby limiting the amount of acoustic reflections to the anechoic chamber itself.

Test sections
Within the anechoic chamber there are two test locations. The first test location is in a ducted section. This section was not used as the aim was to quantify the aeroacoustic signature of the airfoil for various erosion conditions using a microphone array, and the wall prevents the sound waves to propagate to the microphone array. The second test section is located further back. Here, the test section only has a solid wall on the top and the bottom side where the airfoil is mounted, The sides are open and the microphone array has line of sight to the model, this was section used for the experiment. The open test section where the airfoil is mounted has a height of 695 mm. The leading edge of the airfoil in an $\alpha_t = 0°$ configuration is positioned 730 mm from the fully ducted section. The lower surface of both the ducted and open test sections of the wind tunnel is positioned 1415 mm from the ground.

Rotating disk
The airfoil is mounted on a rotating disk; this allows the angle of attack to be altered. The rotating disk is relatively flush with the bottom and top surfaces of the test section. However, the adjustment of the angle only occurs on the bottom rotating disk, while the top rotating disk follows the bottom using torsion that is transferred through the model. as the top disk only ”follows” the bottom disk, the angle does not evenly match however, the bearings in the top disk are smooth and the model is quite stiff, so the difference in angle between the top and bottom is insignificant. To measure the angle of the model, a protractor is positioned on the bottom of the disk; however, when installing this scale, there was a large tolerance on the positioning of this scale, so to measure the angle accurately, an alternative method was used. The rotating disk consists of four circular sectors that are mounted on a large bearing. The assumption was made that these circular sectors were cut perfectly perpendicular and that the edges were mounted parallel to each other. Furthermore, the airfoil insert is placed in the middle of the table. To position it to the zero degree angle, the distance between the edge of the table and the edge of the insert plate was measured at two locations, then the disk was rotated to a point where the measurements on these two locations matched resulting in a zero angle of attack. Here the assumption is made that the edge of the table is parallel to the flow of the wind tunnel. The diameter of the rotating disk (D_{DRD}) was measured at 1198 (mm), the distance between the cut out in the table and the gap between the circular sectors was measured in the zero angle of attack positioned. The distance between the table and the gap between the circular sections can be calculated for the desired angle using the diameter of the disk. Using a caliper, the disk was rotated to match the distance (D_{ARD}) value of the desired angle.

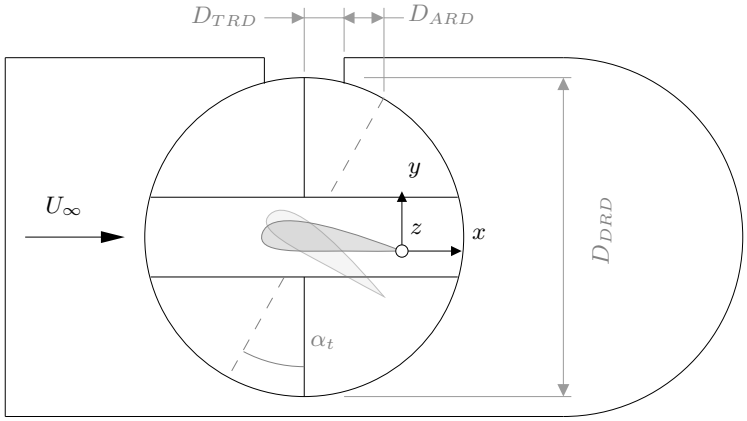

Figure 4.2: Angle alignment rotation disk

Motor
To move air through the wind tunnel, a motorized fan is placed in the basement of the wind tunnel facility. The motor is controlled by the LabVIEW program by setting a power between 0 and 100 %. When the motor speed is set, there is some time required to stabilize the flow to achieve near steady conditions.

Cooling
Due to the friction between the circulated air and the surface of the wind tunnel the temperature increases. To limit the heat built up of the flow, an evaporator of a refrigerator cycle is placed behind the fan where the air is cooled. This cooling works on an automated system and a manual valve. During the experiments, there were some difficulties with the cooling system, causing some fluctuations between the measurements.

4.2. Wind tunnel conditions

The goal was to test the airfoil at the maximum lift over drag ratio, and a wind tunnel angle of attack that was able to be reached comfortably. Therefore, the conditions selected to conduct the experiments were chosen partly based on the paper by Y. de Valk [53], here the maximum tested Reynolds number is around 870,000. To be sure that the experiment could be conducted, a lower Reynolds number of 800,000 was chosen. By doing so, the conditions that where chosen to operate were able to be interpolated*.

α_{wt}	α_{eff}	Re_c	C_L	C_M	C_d	C_{dp}	$\frac{C_l}{C_d}$
13.0	8.02	869795	1.132	-0.1528	0.0145	0.0256	77.883
16.0	10.26	350610	1.296	-0.1440	0.0247	0.0378	52.461
13.4*	8.32*	800 000*	1.154*	-0.1516*	0.0159*	0.0272*	74.465*

Table 4.1: Interpolated data for experimental conditions based on measurements of DU97-W-300 airfoil by de Y. de Valk [53]

For the experiment, the wind tunnel $\alpha_t = 14°$ was used as this is slightly beyond the point of $(C_l/C_d)_{max}$. At this point, the flow is attached to the airfoil. When a surface disturbance like LEE is introduced at this critical point, the effect of the LEE is expected to be more severe.

4.3. Design of experimental Model

4.3.1. DU97-W-300 airfoil

The airfoil that was available to be used in the wind tunnel was the DU97-W-300. The airfoil was developed at the Technical University Delft with the use of wind turbine applications in mind. The airfoil was designed for wind turbines of significantly lower power 300 kW and the position of the airfoil was intended for a more root sides position. The high thickness of the airfoil at $t/c = 0.3$ is more suitable closer to the root, which favors this property. The region where the aeroacoustic effects are the most pronounced as discussed lies more to the tip side of the rotor. This region typically has airfoil with a smaller relative thickness. The NREL reference wind turbine uses a NACA 64-618 profile at a radial position of $r/R = 0.89$. The two airfoils are shown in the Figure 4.3.

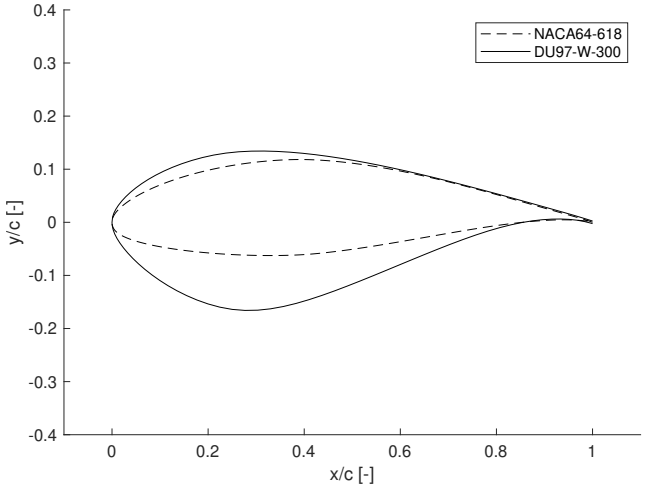

Figure 4.3: Airfoil of the NREL turbine at $r/R = 0.89$ and the DU97-W-300 airfoil

The two airfoils do differ from each other as the pressure side of the NACA 64-618 airfoil is not similar to the DU97-W-300 airfoil, but the suction sides are relatively similar to each other. However, because this study is experimental in nature and the wind tunnel facilities at the University of Twente are not capable of reaching the Reynolds regime that the wind turbine blade experiences closer to the tip of the airfoil, another approach is taken. For this we will look at the conditions of the NACA 64-618 airfoil at the Reynolds conditions of the wind turbine, and these conditions will be attempted to be matched at for the DU97-W-300 airfoil at Reynolds numbers capable at the wind tunnel facility.

4.3.2. XFOIL analysis

Due to the inability of wind tunnel conditions to accurately replicate real-life scenarios and the geometry is not similar of the airfoil, the airflow around the NACA 64-618 airfoil was examined under the conditions depicted in Table 4.2. These conditions correspond with those under which the NREL 5MW reference turbine was analyzed, as described in Section 3.2. The angle of $\alpha_t = 14°$ for the DU97-W-300 was selected based on the maximum lift to drag ratio at a chord-based Reynolds number of 800 000. This Reynolds number represents the higher end of the capabilities, yet remains within the wind tunnel capabilities.

Airfoil	$\boldsymbol{Re_c}$	$\boldsymbol{\alpha}$
DU97-W-300	8×10^5	$8.8°$
NACA 64-618	1.1×10^7	$8.3°$

Table 4.2: Airfoil comparison with Reynolds number (Re_c) and angle of attack (α)

Figure 4.4 illustrates the pressure coefficient across the airfoil under the two different conditions. The figure depicts the pressure coefficient along the total chord length of the blade for both airfoils, the figure also shows a focused view on the leading edge of the airfoils. What can be seen is that the pressure side of the leading edge shows a relatively close correlation between the two conditions.

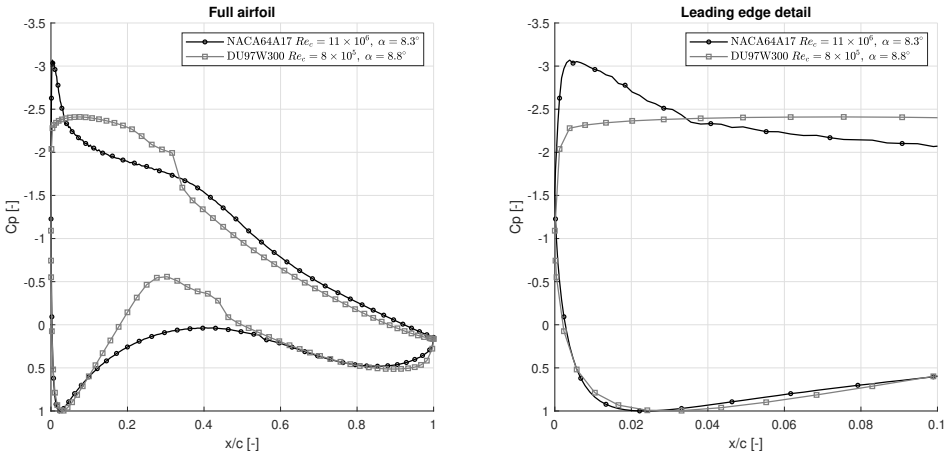

Figure 4.4: Comparison of pressure coefficient (C_p) between NACA 64-618 and DU97-W-300 airfoils.

4.3.3. Coverage

The decision was taken to use the coverage as outlined by Gaudern [45], where the coverage of various stages is quantified by the percentage of chord length. The same coverage methodology was adopted in the IEA Wind task 46 [2] which aims to standardize the models of erosion on the wind turbine blades. In this context, the coverage is denoted as a percentage of the chord length and is centered on the leading edge of the airfoil.

Erosion Model	Coverage (%)	Upper Surface Coverage (mm)	Lower Surface Coverage (mm)
P	3	7.5	7.5
PG	3	7.5	7.5
DL 4	5	1.1	1.4
DL 3, DL 5, DL 6	5	6.5	8.5
DL 2	8	17.4	22.6

Table 4.3: Coverage per erosion stage

Distribution and quantity of pits and gouges
The quantity of the pits and gouges was based on the data from Sareen [46], this data was scaled to the span of the model used in the wind tunnel wind tunnel experiments. The resultant scaling of the defect quantities is shown in the Table 4.4

Erosion Model	Number of Pits	Number of Gouges
P	72	0
PG	144	72

Table 4.4: Number of pits and gouges per damage stage

The distribution and locations of the pits and gouges where determined using a Gaussian distribution. The extend of the upper and lower coverage of the erosion features remains the same; however, the quantity is distributed between the upper and lower side of the airfoil in the ratio 1 to 1.3 respectively. The location of the pits and gouges erosion features are shown in appendix C, in the Figures C.2, C.4, C.5.

4.3.4. Depth scaling using roughness height Reynolds number

To scale the depth of the erosion features in the wind tunnel to the conditions in the in the real world, the roughness height Reynolds number was used. This was done because the Reynolds number based on chord dimensions could not be reproduced within the wind tunnel. The objective is to match the values Re_k between ”real” conditions and the ”model” conditions that are achievable in the wind tunnel of the University of Twente. For the calculation of the roughness height Reynolds number, an XFOIL analysis was performed for both airfoils under conditions specified in Table 4.2, using the boundary layer data. As indicated previously, the computation of Re_k varies depending on whether the roughness characteristic is within or outside of the boundary layer. This required the velocity profile, specifically the velocity $u(k)$. The profile which is approximated using the Pohlhausen fourth-order polynomial [55]. The formula is shown in Equation 4.1 [56].

$$u(y) = f(\eta)\, U_\infty \tag{4.1}$$

In the equation $\eta = \frac{y}{\delta}$, and can be calculated using the equation:

$$f(\eta) = 2\eta - 2\eta^3 + \eta^4 + \Lambda\left(\frac{\eta}{6} - \frac{\eta^2}{2} + \frac{\eta^3}{2} - \frac{\eta^4}{6}\right) \tag{4.2}$$

In the equation the Pohlhausen parameter Λ is used, this is based on the shape factor H, which is obtainable from XFOIL simulations.

$$H(\Lambda) = \frac{\frac{3}{10} - \frac{\Lambda}{120}}{\frac{37}{315} - \frac{\Lambda}{945} - \frac{\Lambda^2}{9072}} \tag{4.3}$$

The reason why the Pohlhausen fourth-order approximation was used above other velocity profile approximations was that Pohlhausen used momentum as the parameter to be preserved [56]. Equation 4.4 shows that

Reynolds roughness is calculated using Reynolds momentum thickness when the roughness feature protrudes from the boundary layer.

$$Re_k = \frac{\rho u(k) k}{\mu} \quad (k < \delta) \qquad or \qquad Re_k = \frac{k}{\theta_k} Re_\theta \quad (k > \delta) \tag{4.4}$$

What was found was that all erosion features extend beyond the boundary layer. In the Figure 4.5 the velocity profile and the pit erosion feature is shown for operational conditions of the NREL reference turbine.

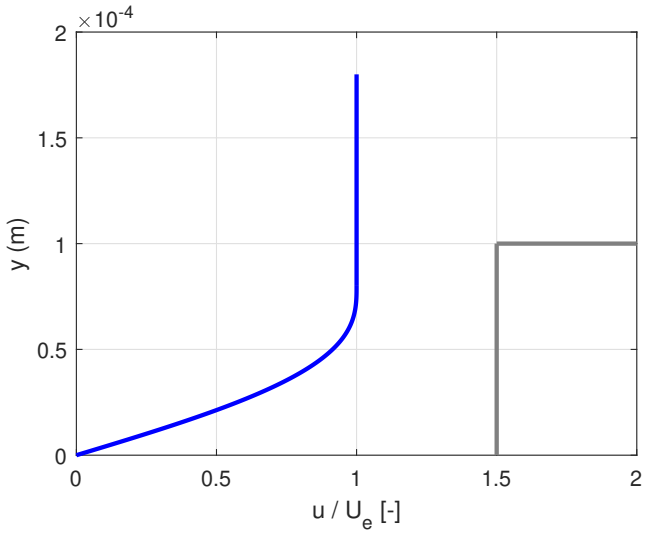

Figure 4.5: The boundary layer velocity profile compared to the depth of a pit erosion feature, for the operating conditions of the NREL Turbine

The result of the scaling is shown in Table 4.5 where both the depth used in the model and the depth in real world conditions are shown. However, an attempt was made to match Re_k as closely as possible, because the model is constructed by gluing sheets of foil on top of each other, a perfect match for the height required to match Re_k could not be achieved, as a certain thickness of foil sheets was used and the depth increment was set at 0.2 mm. The modeling of pits and gouges differs from Re_k encountered in the operating conditions of the wind turbine. As the pits and gouges are distributed features, the depth would have to be scaled according to the chord wise position. The decision was made to use the average position of the defects. The depths chosen for the scaling of the erosion features was based on the measurements as discussed by Gaudern [45], as here the measurement when not based on only based on photographs but also inspection reports of an eroded model of an wind turbine blade provided by Vestas [45].

Erosion Model	Depth ”K” model (mm)	Depth ”k” real (mm)	Re_k (-) model	Re_k [-] real
P	0.2	0.1	1,059	907
PG	0.4	0.2	1,182	1,155
DL2	1.2	0.8	5,503	5,554
DL3	1.2	0.8	5,743	5,753
DL4	1.2	0.8	1,624	6,145
DL5	1.0	–	4,691	–
DL6	0.8	–	3,521	–

Table 4.5: Scaled depth for wind tunnel conditions of Re_k at $Re_c = 8 \times 10^5$ at $\alpha_t = 14°$

4.3.5. Size

Based on the depth and quantity of the erosion features, the size of the feature was determined based on the mass loss presented in the Table 4.6. This was based on the model proposed by IEA Wind [2].

Erosion model	Coating mass loss (%)	Laminate mass loss (%)
P	2	0
PG	30	0
DL4	75	10
DL3	100	60
DL2	100	100

Table 4.6: Mass loss percentages used based on data from the IEA Wind task 46 [2]

Using the mass loss shown in Table 4.6, the size of the erosion features where calculated. The total mass of the coating and laminate is based on the thickness of the coating and laminate respectively, and the height and width of the laminate. The thickness of the coating is set to be equal to the depth of gouge erosion defect ($k_G = 0.4$ mm). The thickness of the laminate is set to be equal to the depth of the delamination ($k_{DL} = 1.2$ mm) feature minus the depth of the coating thickness. The construction of the coating and the laminate is depicted in the Figure 4.6.

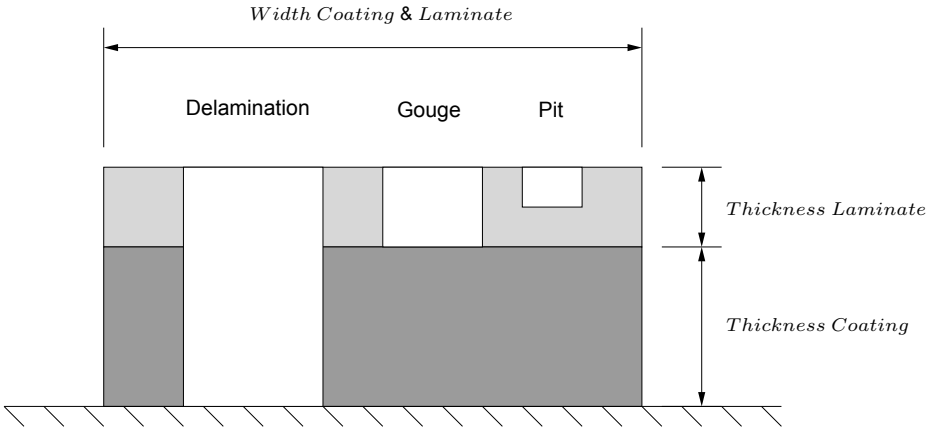

Figure 4.6: Thickness of coating and laminate layer

Dimensions pits and gouges

The pits and gouges are modeled as cylinders where the depth is based on the value Re_k. The diameter of the pits and gouges is based on the mass loss presented in the Table 4.6. In the stage where both pits and gouges were present, the mass loss attributed to the pits was calculated based on the determined size of the pits. The remaining mass loss was attributed to the presence of gouges, the size of the gouges was subsequently determined.

Erosion Feature	Diameter calculated (mm)	Diameter used (mm)
Pits	1.9271	2
Gouges	4.9157	5

Table 4.7: Diameter of erosion features calculated from surface data

Delamination
In real-world conditions, delamination often presents itself as a jagged edge that follows the orientation of the underlying composite layup. For the modeling of the delamination feature, a simplified approach was taken and the delamination was modeled as a vertical straight edge. The width of the delamination feature was calculated on the basis of the coverage in the damage stage and the mass loss of the laminate. The extension of the erosion feature is divided on the basis of the 1:1.3 ratio [46]. The extent of the delamination features of the erosion model is shown in the Table 4.8.

Erosion Model	Extension upper Foil (mm)	Extension lower foil (mm)	Total width (mm)
DL4	1.1	1.4	2.5
DL3	6.5	8.5	15
DL2	17.4	22.6	40

Table 4.8: Extension measurements for different erosion stages

4.3.6. Erosion models
To model the effects of surface roughness on the leading edge of the model without damaging the airfoil model and allowing evaluation of the effects of various degrees of LEE. To model the LEE a self-adhesive foil was attached to the leading edge of the DU97-W-300 airfoil. The adhesive foil used is a plastic foil with a thickness of 0.2 mm. Depending on the specifications of the erosion feature, the layers of the erosion model where altered to simulate erosion damage. Table 4.9 shows an overview of the basic specifications of the erosion models.

Erosion model	Erosion feature	Coverage (mm)	Depth (mm)	Re_k
Clean	-	-	-	-
No DMG	-	-	-	-
P	Pits	15	0.2	1,059
PG	Pits+Gouges	15	0.2–0.4	1,182
DL2	Delamination	40	1.2	5,503
DL3	Delamination	15	1.2	5,743
DL4	Delamination	2.5	1.2	1,624
DL5	Delamination	15	1.0	4,691
DL6	Delamination	15	0.8	3,521

Table 4.9: Description of erosion features per erosion model

The data for each foil to model the different erosion stages are shown in Table 4.9. The ”No DMG” model is the standard stack of adhesive foils that forms the basis for all erosion models. The foil is shown in Figure 4.7. For the No DMG model none of the layers are damaged in any way. The standard foil stack is constructed in a pyramid shape. The upper layer covers the ”steps” of the foil stack. This is to have a smooth transition from the foil to the surface of the airfoil. For application, the layers are placed iteratively on the leading edge of the airfoil. In the subsequent figures illustrations of each erosion models are shown.

Erosion model: No DMG

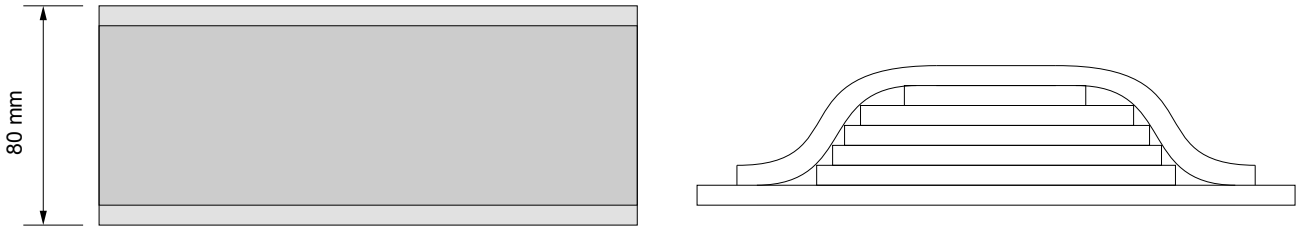

Figure 4.7: Schematic illustration of the erosion model NO DMG

Erosion model: P

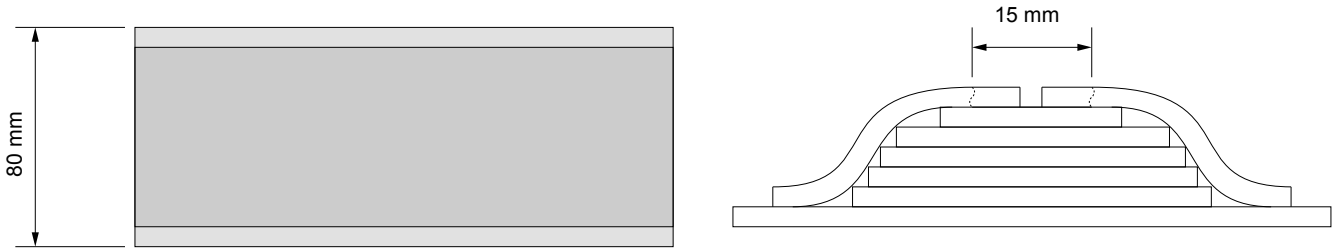

Figure 4.8: Schematic illustration of the erosion model P

Erosion model: PG

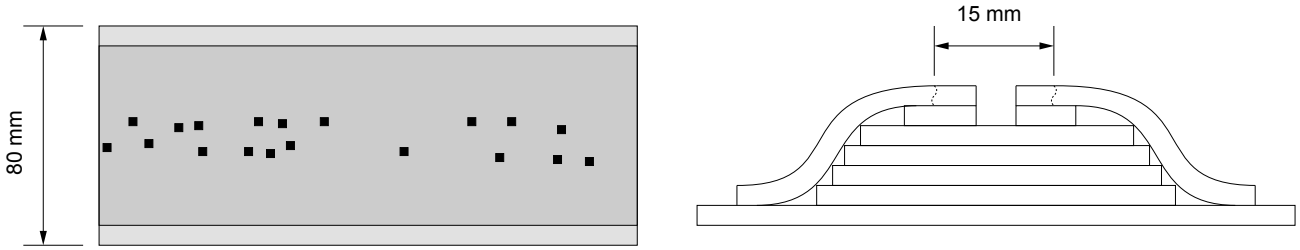

Figure 4.9: Schematic illustration of the erosion model PG

Erosion model: DL2

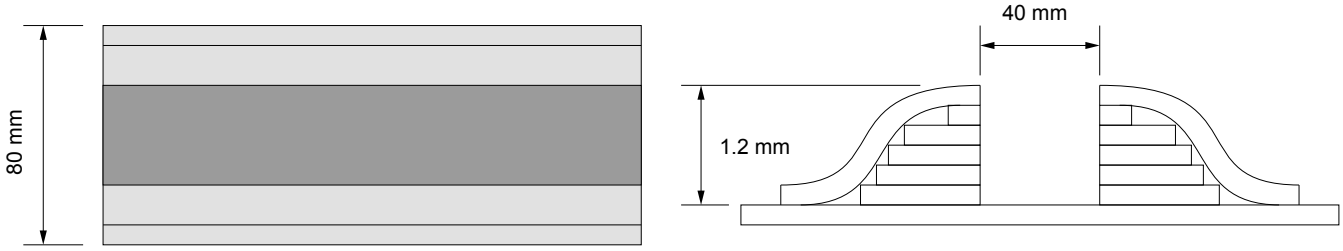

Figure 4.10: Schematic illustration of the erosion model DL2

Erosion model: DL3

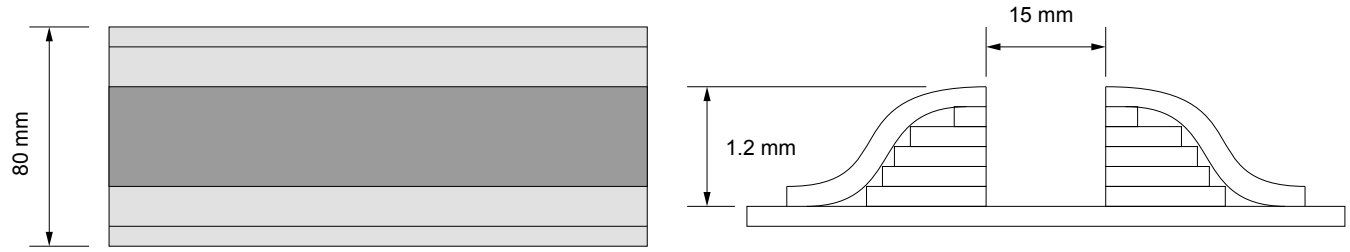

Figure 4.11: Schematic illustration of the erosion model DL3

Erosion model: DL4

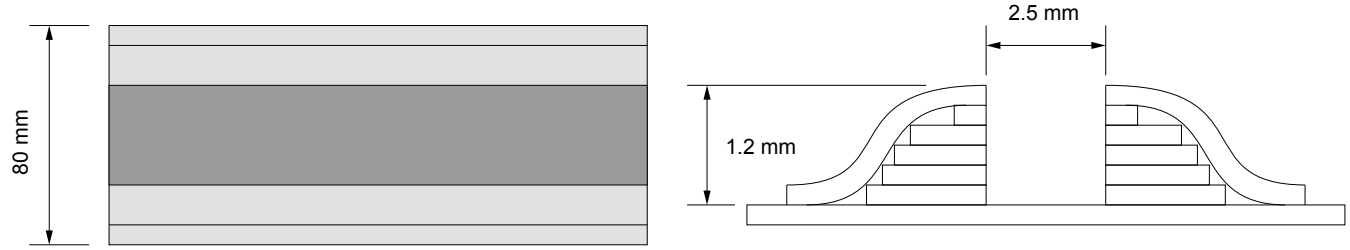

Figure 4.12: Schematic illustration of the erosion model DL4

Erosion model: DL5

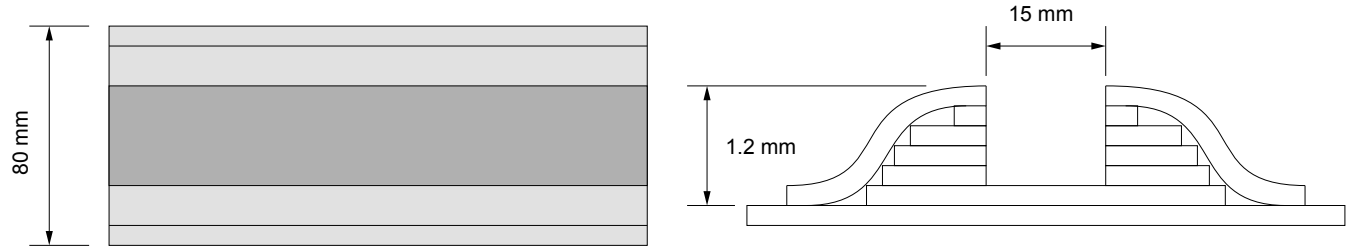

Figure 4.13: Schematic illustration of the erosion model DL5

Erosion model: DL6

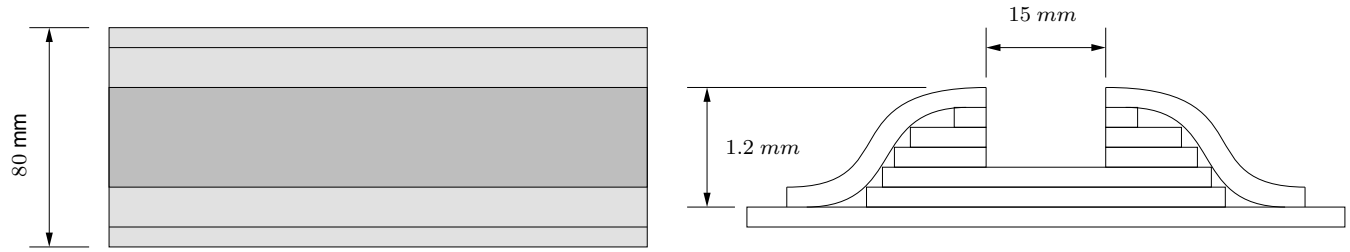

Figure 4.14: Schematic illustration of the erosion model DL6

4.4. Measurement instrumentation

In this chapter the measurement instrumentation, their properties and the locations are discussed. In the Figure 4.15 the general layout of the measurement setup is shown.

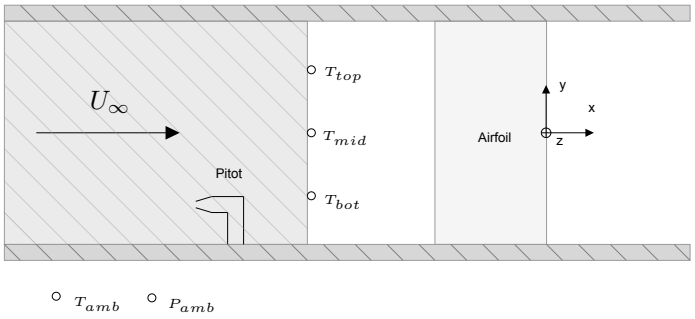

Figure 4.15: General layout measurement instrumentation

4.4.1. Microphone array

The main measurement device was the Bionic M-112 microphone array, which consists of 112 MEMS microphones and was made by CAE Software & Systems. The microphones are mounted on a web shaped structure that positions them in a spiral configuration. The microphones in the array are all located in the same XY plane, the positions of the microphones are shown in the Figure 4.16. During microphone setup, the position of the array was carefully measured.

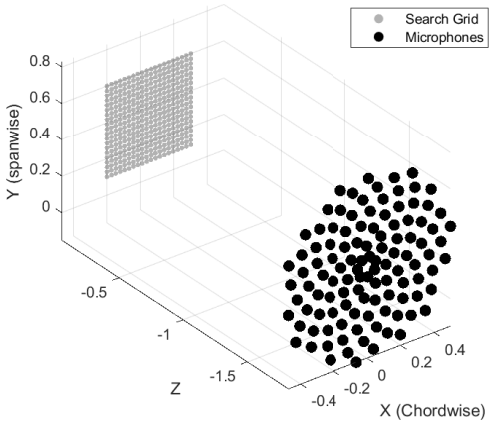

Figure 4.16: Positions of the microphones search grid array

To position the microphone array in the X direction, the origin of the microphone array was positioned inline with the ZY plane of the global coordinate system such that it lines up with the trailing edge of the airfoil in the zero AoA condition. To determine the Z position of the microphone array, there were several considerations, firstly, the microphone array had to be positioned in the far field of the noise produced. In addition to this, the microphone array was desired to be placed as far away from the test section as possible. During preliminary testing what was found was that due to the large angle of attack used in the experiments there is an flow in the Z direction, this flow ”pushes” in the direction of the airfoil. And what was found that this caused some vibrations in the ”arms” where the microphones are mounted, by moving the microphone further away from the test section the vibration of the microphone arms was minimized. However, the limitation here was the size of the anechoic chamber. The Z coordinate of -1.8 m was chosen; this ensures that the microphone is in the far field of the expected noise produced. Another reason for the positioning of the microphone array is the idea that in the real world microphones could be mounted on the tower structure of the wind turbine to concurrently monitor the noise produced by the airfoil. To make sure the microphone array remains in place, a large mass was mounted underneath the tripod to prevent the wind from moving the array itself.

4.4.2. Pressure sensors

For the calibration of the velocity of the stream in the wind tunnel, a pitot tube was placed in the ducted section of the wind tunnel. The pitot tube mount is mounted inside the ducted test section at a height of 110 mm, to ensure that the angle of the pitot tube is perpendicular to the flow, the mount holding the pitot tube has an indent such that it is mounted in the same orientation every time.

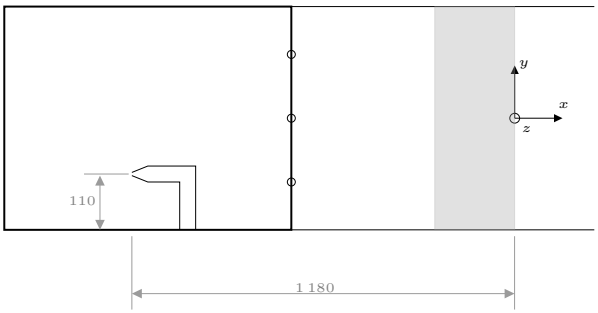

Figure 4.17: Location pitot tube

The pressure measured by the pitot tube is the total pressure and the static pressure, this consists of both a static and a dynamic component. The relation between these pressures can be used to determine the velocity of the flow using Bernoulli's principle.

Pitot tube pressure sensor

The pressure sensor that measured the total pressure in the steam of the wind tunnel consisting of both dynamic and static components is the CXLdP made by AE sensors. The sensor used is a high accuracy low pressure differential sensor. The accuracy class (span) of the sensor is $\pm 0.25\%$. However, the sensor used in the experiments has been calibrated to reach a span of $\pm 0.02\%$. The calibration report for this sensor can be found in Appendix G. The data output from the pressure sensor is analog and is read by the LabVIEW control program. The equation for the best-fit line for the calibrated curve is shown in Equation 4.5, this was incorporated in the LabVIEW control program.

$$dP = V_{CXLdP} * 1.000026 - 0.00521 \tag{4.5}$$

Pressure sensor Ambient pressure

For the used ambient pressure sensor is the model 278 barometric pressure transducer manufactured by SETRA Systems. The pressure sensor range is limited from 806 to 110 hPa and has a precision specification of $\pm$ 0.3 hPa, but it has been calibrated to reduce this to an accuracy of $\pm$ 0.2 hPa, the calibration report for the sensor can be found in Appendix G. The sensor outputs a voltage between 0.1 and 5 V and is read by the LabVIEW program. Using the pressure calibration, a best-fit curve was created and used in the LabVIEW program. The temperature used for the temperature of the stream is the average of the three sensors.

$$P = V_{AmbP} * 5997.697 + 79998.96 \tag{4.6}$$

4.4.3. Temperature sensors

There are several temperature sensors present in the experiment; one is positioned to measure the temperature in the anechoic chamber, and three are positioned at the end of the ducted test section. The location of the sensors are shown in Figure 4.18.

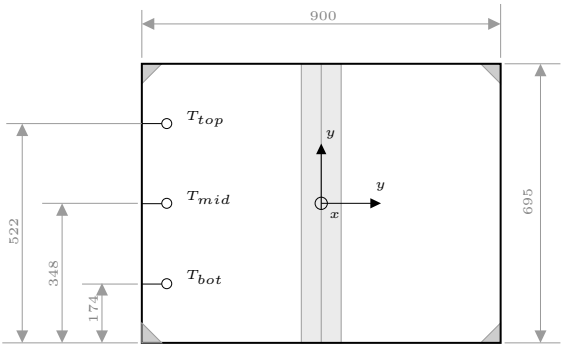

Figure 4.18: Location temperature sensors

5

Experimental procedure

5.1. Preliminary experiments

Because the airfoil section and the wind tunnel itself can not be damaged during the experiments, preliminary tests were carried out to prove that the application of the erosion model does not effect the airfoil or the wind tunnel itself. To do this test where preformed to test the removability of the adhesive foil on the surface of the model and that the foil itself remained attached to the airfoil.

5.1.1. Test removability of the foil

Before the foil was applied to the airfoil, a preliminary test was conducted to ensure that the foil could be applied and removed without causing damage to the airfoil's surface. This procedure was carried out on a demonstration section of the airfoil, where several square sections of foil were applied. These sections were removed at varying intervals to determine the presence of any residue. For the removal of the foil a soft plastic wedge was used to prevent damage to the model. After removal, the airfoil surface was cleaned with a microfiber cloth with isopropyl alcohol. Figure 5.1 shows the before and after completion of the test.

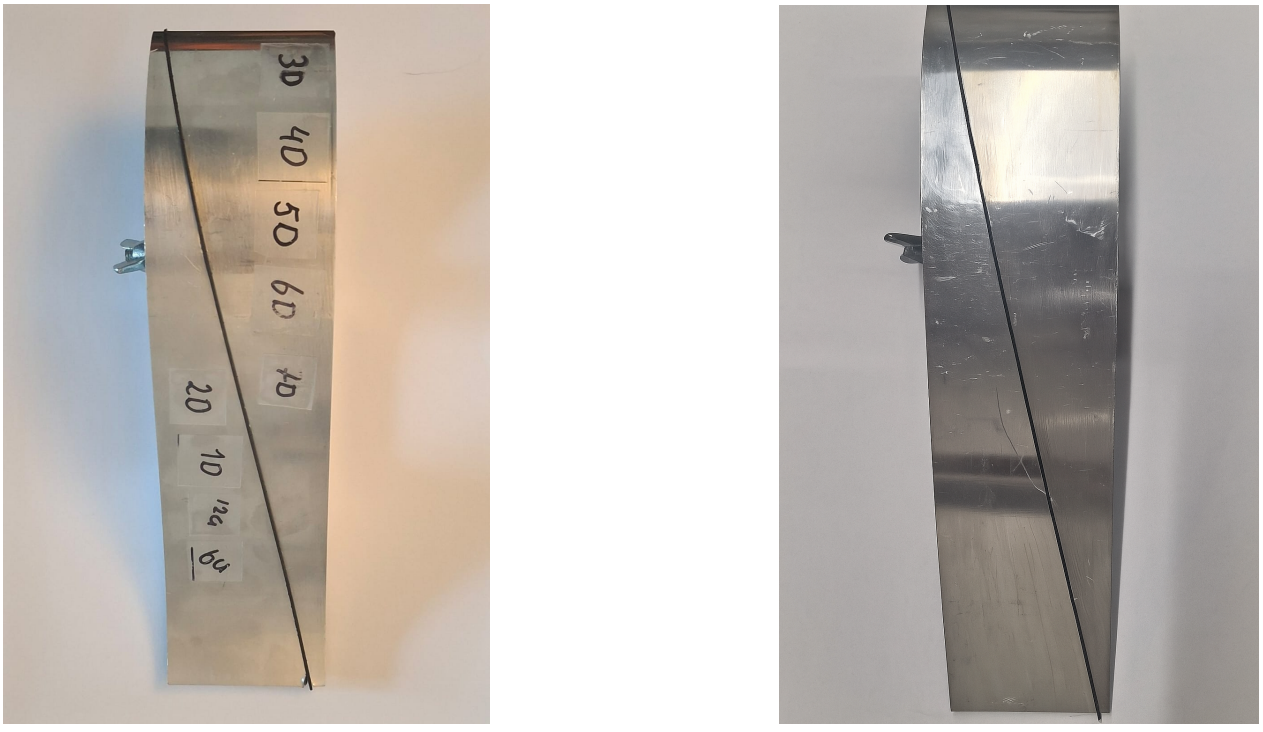

(a) Test applied foil squares

(b) After removal and cleaning

Figure 5.1: Test foil removal on a section of the DU97-W-300 airfoil

5.1.2. Net test

To test if the erosion model would remain attached to the airfoil, a section of foil was attached to the airfoil while a net was positioned at the rear of the anechoic chamber. If the foil where to be detached from the airfoil the net would prevent this from entering the tunnel loop. In the Figure 5.2 the setup of the net test is shown where in 5.2a the foil attached to the model is shown and in 5.2b the net mounted to the rear of the anechoic chamber is shown.

(a) Test applied foil squares

(b) Adhesive foil used for the Net test

Figure 5.2: Setup net test for the wind tunnel experiment

The net test was performed at the maximum wind speed and at a wind tunnel angle of $\alpha_t = 14°$. The test was successfully completed with the foil stayed attached during the 5 minute test under these conditions.

5.1.3. Calibration

For the calibration of the microphone array, CEA includes a built in microphone calibration algorithm. For the calibration the microphone array requires a frequency to be played for a certain length of time [57]. To do this a speaker was placed as close to the origin as possible as shown in Figure 5.3. In an ideal scenario, a perfect sound source would have been used that would be floating in the air. However, for this experiment the calibration was done by a speaker that was placed on a box to achieve the desired position.

Figure 5.3: Microphone Calibration Setup using a Speaker

Frequencies were played from 200 Hz to 22 kHz, in steps of 200 Hz for a length of 10 seconds each. The sound was made at the same volume for all frequencies. The reason for not including frequencies above 22 kHz was that the speaker started to distort and could not accurately produce frequencies above 22 kHz.

5.2. Erosion application

The DU97-W-300 airfoil has static pressure ports, these are very small holes located on the top and bottom surface of the airfoil over the entire chord. As the foil used to model the damage is self adhesive, there is a risk that when the foil is applied over the static pressure pots, the holes might get clogged. To prevent this a thin film of of tape is placed over the static cover port to prevent this from happening as shown in Figure 5.4. The model of the erosion was applied to the leading edge of the airfoil on top of this protective tape.

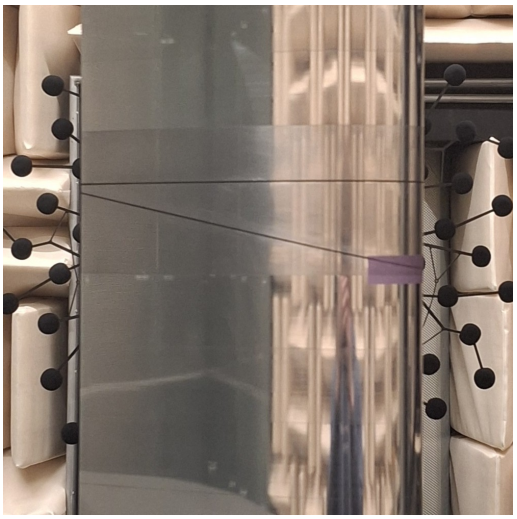

Figure 5.4: Static pressure ports covered by protective tape on the DU97-W-300 airfoil

5.3. Velocity calibration

Before each acoustic measurements a velocity calibration test was preformed, this was done because between the acoustic measurement, significant time was required to remove the old erosion model, clean the airfoil, and apply a new erosion model. These processes generally took around three hours. Therefore, a singular measurement of the wind tunnel velocity at the beginning of the day for a specific motor speed was not deemed to be sufficient as the ambient conditions varied. The pitot tube could not be inserted during the test, as the pitot tube itself caused the flow to be disturbed before reaching the airfoil. As this disturbance was unknown, and the goal was to assess the disturbances caused by the LEE, the decision was made to perform a separate velocity calibration run and an acoustic run in the wind tunnel. The reason for performing a velocity calibration run, as the name implies, is to measure the velocity in the test section of the wind tunnel. The power supplied to the motor compensated for the friction in the entire wind tunnel loop, the greatest effect of to the power required between tests was the angle where the airfoil was mounted, as a higher angle of attack increased the drag on the airfoil. The assumption was made that the drag caused by the pitot tube itself was negligible.

5.4. Acoustic measurement

For the acoustic measurements, the motor power was set to the same speed as that of the velocity calibration. Before starting the measurements of the microphone array, the velocity in the wind tunnel was allowed to stabilize. The pitot tube was not installed during the acoustic measurements, but the temperature data was taken. When the temperature was steady for roughly 20 seconds, the microphone measurement was stared. The microphone measurement period was set to 25 seconds with a sample rate of 48 kHz. During this measurement, the properties of the wind tunnel sensors were captured.

5.5. Test matrix

In Table 5.1 the experimental runs are shown for each damage model. The decision was made to include experiments under multiple chord based Reynolds number as this would allow to see the effect of different values for Re_k. Although erosion was not scaled for these conditions and the pressure field varied between these conditions, the additional experiments conducted at different wind speeds were relatively time efficient. These experiments have the potential to offer valuable insights into the effects of the Re_k on the acoustics of LEE.

Erosion Model	$Re_c = 8.00 \times 10^5$	$Re_c = 7.00 \times 10^5$	$Re_c = 6.00 \times 10^5$
No Airfoil	0a	0b	0c
CLEAN	1a	1b	1c
NO DMG	2a	2b	2c
DL 2	3a	3b	3c
DL 3	4a	4b	4c
DL 4	5a	5b	5c
P+G	6a	6b	6c
P	7a	7b	7c
DL5	8a	8b	8c
DL6	9a	9b	9c

Table 5.1: Test runs grouped by erosion feature and Re_c values

6

Post processing

After the data was collected, the data was processed and analyzed. In this chapter, the steps taken in the post-processing of the data are discussed.

6.1. Correction velocity calibration and acoustic measurements

6.1.1. Velocity correction

Between the velocity calibration run in the wind tunnel and the acoustic measurement, the temperature in the wind tunnel varied. The measurement devices used in the respective measurement are shown in Table 6.1.

Properties	Velocity Calibration	Acoustic Measurement
P_0 Test section	x	–
P_0 Anechoic Chamber	x	x
T Test section	x	x
T Anechoic Chamber	x	x
Microphone	–	x

Table 6.1: Measurement setup matrix for velocity calibration and acoustic testing.

To account for the impact of temperature variations between the velocity measurement test and the acoustic measurement test runs, some corrections have to be made. Between the experiments, the power of the motor was set to the same power between the experiments. The assumption was made that the power of the motor is proportional to the energy within the mass flow of the wind tunnel [23]. Using the assumption, the relation between motor power and wind power is shown in Equation 6.1. The assumption made here is that the performance coefficient of the motor C_η is constant between the different conditions.

$$P_{motor} = E_{Wind} = C_\eta \frac{1}{2} \rho A_T U^3 \tag{6.1}$$

Because the power of tunnel and the shape of the tunnel are constant, the velocity is dependent on the change in density and can be calculated using the Equation 6.2.

$$U_{AT} = U_{VC} (\frac{\rho_{VC}}{\rho_{AT}})^{1/3} \tag{6.2}$$

The difference in density is calculated using the ideal gas law [22].

6.1.2. Viscosity correction

The correction of the viscosity between the velocity calibration experiment and the acoustic measurement utilized Sutherland's law [23]. This law uses the empirical value Sutherland's constant to relate the viscosity of a gas and its temperature. In this equation, the Sutherland constant has a value of $S = 110.4$ K, and the reference temperature and reference viscosity are $T_{\text{ref}} = 273.15$ K and $\mu_{\text{ref}} = 1.716 \times 10^{-5}$ Pa · s, respectively.

$$\mu = \mu_{ref} \left(\frac{T}{T_{ref}} \right)^{3/2} \frac{T_{ref} + S}{T + S} \tag{6.3}$$

6.2. Beamforming analysis

6.2.1. Section of interest

For the beamforming map, a specific section of the test section is looked at. To make sure that the entire microphone array has line of sight to the test section, not the entire test section can be used.

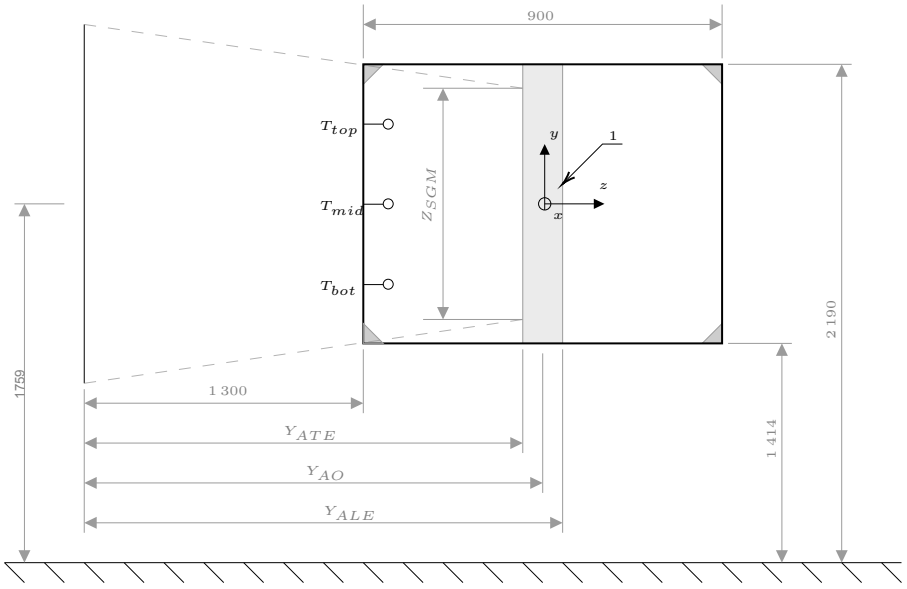

Figure 6.1: Line of sight of the beamforming array and the test section

To ensure that the analyzed section of the beamforming array is within the line of sight of the microphone array, the section of interest was set to 600 by 600 mm.

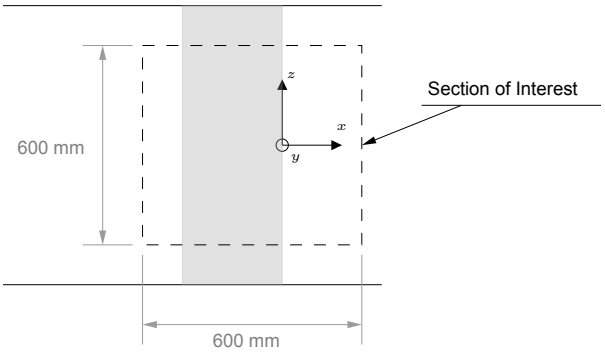

Figure 6.2: Assumed propagation path acoustic wave

6.2.2. Beamforming correction

Based on the conditions measured during the acoustic test, the beamformer was corrected. To correct for the sound propagation, the downstream transport of the acoustic waves was taken into account. In this correction, the assumption is that the shear layer is straight, that the flow only exists as a perfect rectangular flow, and that the air in the anechoic chamber is stationary. The correction for transport in the x direction can be calculated. First, we calculate the time of the acoustic wave in the wind tunnel t_{WT}, as shown in Equation 6.4. Using the speed of sound in the wind tunnel based on the ideal gas law 6.6.

$$t_{WT} = \frac{Z_{AP,\ WT}}{a_{wt}} \tag{6.4}$$

The correction for the propagation of the wave in the x direction uses the time in the wind tunnel and the velocity of the wind tunnel, as shown in Equation 6.5

$$X_{BFCorrection} = t_{WT} * U_{WT} \tag{6.5}$$

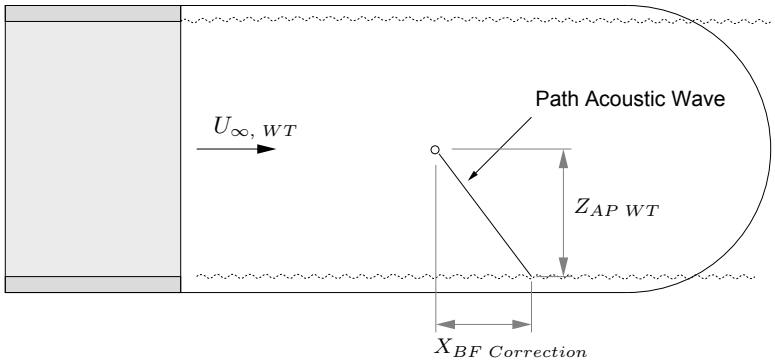

Figure 6.3: Assumed propagation path acoustic wave

The speed of sound in the wind tunnel a_{wt} is calculated using the ideal gas law and is therefore a function of the temperature of the fluid.

$$a_{wt} = \sqrt{\frac{\gamma RT}{M}} \tag{6.6}$$

6.2.3. BeamUT beamformer

The beamformer used was developed by Sanders [35] and extensively described in BeamUT documentation. The reason for the use of this beamformer is that it has been verified and tested against standard benchmark cases as set by BTU [58]. The results show this especially at higher frequencies above 5 000 Hz, where the beamformer showed good coherence with the exact values and the power was well within 1 dB of the results. At lower frequencies, the accuracy of the beamformer was within 2 dB. The advanced algorithms DAMAS and CLEAN algorithms that where created were generally worse in terms of the dB accuracy. However, they where more successful in showing more clearly where the sound originates. Due to the assumption that the shear layer is straight and the uncertainty of the path of the acoustic waves that propagate through the shear layer, the exact location already has a degree of uncertainty. However, for this research the exact location of the noise source is not of great importance. As the goal is to identify generally where the sound is coming from, either leading edge, trailing edge, or from the wind tunnel itself. The DAMAS and CLEAN algorithms are computationally intensive and thus not used for this study. The beamformer used is a conventional delay and sum beamformer in the frequency domain. The frequencies are split up into a bin the size of one-third octave. The frequency shown in the beamforming maps represents the center of this bin. The Cross Spectral Matrix (CSM) is calculated using the Welshes method. In this method an overlap of 50 % is used over the different frequency bins, in addition to this a Hamming window is applied to the bins. By defining a search grid and knowing the positions of the microphone array, steering vectors are drawn from each microphone position to

the search grid point, and a phase delay is added to the signal, compensating for the time delay for the signal to get to the microphone. The steps of the BeamUT are shown in the box below.

Beamformer - BeamUT procedure

1. `TDMS2MDATA.m`
   Converts a `.TDMS` file to `.hdf5` format, which is used as input for the beamforming code. Mostly it contains the microphone time series data. This code was adapted by introducing a Python script to decrease the time required to read the TDMS file.
2. `MDATA2CSM.m`
   Converts the time signals in the `.hdf5` file to Cross Spectral Matrix (CSM) format for the BEAMUT beamforming code. The shear layer is taken into account for each test section.
3. `Plot_Single_Mic_Spectra.m`
   Calculates and plots the spectrum for a single microphone.
4. `INPUTBEAMUT.m`
   Defines all required beamforming input parameters, including search grid locations and microphone positions.
5. `RUN_CBF.m`
   Runs the conventional beamforming (CBF) in the frequency domain.
6. `PLOT_THIRD_OCT_BMAPS.m`
   Integrates and plots third-octave band beamforming noise maps based on the results from the beamforming output.

Beamformer settings

For the depth of the search grid, the distance from the microphone array to the measurement plane was set to $Z_{\text{ATE}} = 1.75$ m. This value was determined to focus the steering vector on the trailing edge region of the airfoil, which is expected to be one of the dominant noise sources, especially for trailing edge noise. The value corresponds to the physical distance from the array to the model in the wind tunnel and was verified by direct measurement. The search grid itself was set to 200 by 200 points, which gives a good balance between spatial resolution and computational time. Increasing the number of points improves the resolution of the beamforming output but also increases processing time, so this grid size was chosen as a practical compromise that still captures the key features of the acoustic sources in the region of interest.

6.3. PSD and SPL

6.3.1. PSD calculation

To calculate the PSD for each of the microphone signals, the cross spectral matrix is used. The diagonal elements of the CSM, denoted as S_{ii}, represent the PSD for each individual microphone. To express the PSD on a decibel scale, Equation 6.7 is used, as described by [35]:

$$\text{PSD} = 10\log_{10}\left(\frac{S_{ii}}{p_{\text{ref}}^2}\right) \tag{6.7}$$

6.3.2. SPL calculation

The sound pressure level is calculated using Equation 6.8. For the calculation, the reference pressure $p_{ref} = 20$ μPa was used [35], as this is the threshold of human hearing. For the measurement, the microphone used is microphone 1, and this microphone is located near the center of the array. The RMS of the pressure was taken for the entire 25 second measurement period.

$$\text{SPL} = 20\log_{10}\left(\frac{p_{\text{rms}}}{p_{\text{ref}}}\right) \tag{6.8}$$

Part III

Experimental findings and analysis of aeroacoustic measurements

7

Acoustic measurements

7.1. Sound pressure level

In Figure 7.1, the sound pressure levels for all erosion models are shown, at $Re_c \approx 8 \times 10^5$. Here 7.31a shows the SPL of the measurement averaged over all 112 microphones, Figure 7.31c shows the normalized SPL around the Clean condition. The figure shows that the SPL does vary depending on the erosion model and thus, the modeled erosion does change the aeroacoustic profile of the airfoil. In the profile section, we discuss the effect of the erosion models.

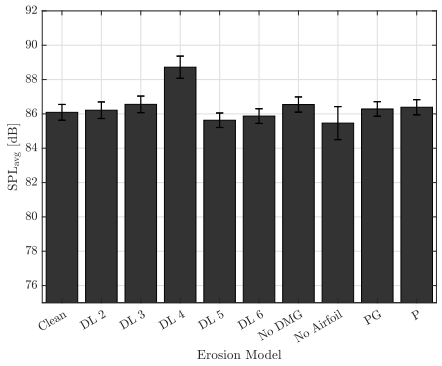

(a) Sound pressure levels per erosion models conditions at $Re_c \approx 8 \times 10^5$ $\alpha_t = 14°$

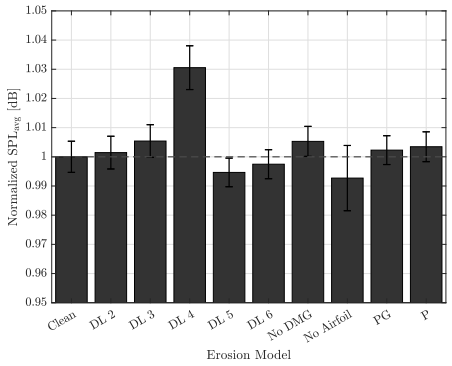

(b) Normalized sound pressure levels per erosion models conditions at $Re_c \approx 8 \times 10^5$ at $\alpha_t = 14°$

Figure 7.1: Normalized sound pressure levels for all conditions at $Re_c \approx 8 \times 10^5$, $\alpha_t = 14°$

In the Figure 7.2 the sound pressure levels averaged of the 112 microphone arrays for all conditions at $Re_c \approx 8 \times 10^5$, $Re_c \approx 7 \times 10^5$, $Re_c \approx 6 \times 10^5$ and $\alpha_t = 14°$. The SPL is expected to increase as the free stream velocity increases. The effects will be discussed in more detail later in the following section.

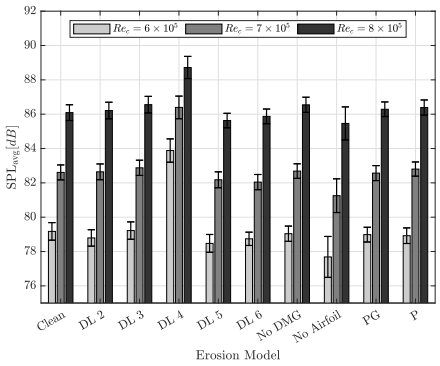

Figure 7.2: Average SPL for all conditions $Re_c \approx 8e5$, $\alpha_t = 14°$

7.1.1. Effect Re_k on the sound pressure level

In Figure 7.3 the influence on the Reynolds roughness number Re_k on the SPL is shown. What can be seen is that the sound pressure level that was measured increases based on the chord-based Reynolds number Re_c, however, the SPL measured remains relatively constant as a function of the Re_k, it even slightly decreases. This shows that the Re_k does not have a direct effect on the SPL.

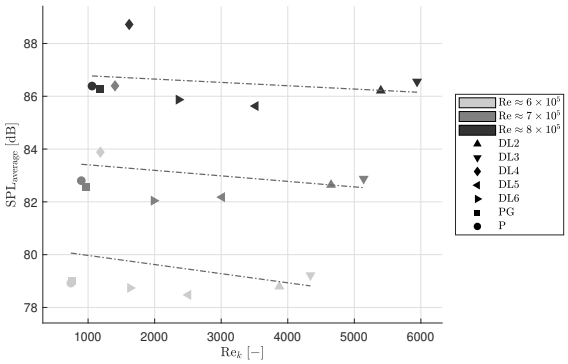

Figure 7.3: Relation between the sound pressure level and the roughness height Reynolds number , $Re_c \approx 8 \times 10^5$ at $\alpha_t = 14°$

The velocity of the flow in the wind tunnel increased from $U \approx 41$ m/s to $U_2 \approx 47$ m/s, increasing the Reynolds number from approximately 700,000 to 800,000. As shown in the Figure 7.2 this increase in velocity resulted in an increase in SPL of approximately 4 dB. As discussed earlier, the typically noise scaling of airfoil self-noise is $P \propto U^6$. Since an increase of 4 dB gives a power ratio of about $P_2/P_1 = 10^{4/10} \approx 2.51$ and the velocity ratio between the two cases is $47/41 \approx 1.146$. Solving for $(U_2/U_1)^n = P_2/P_1$, we get the scaling of the power $n = \log_{10}(2.51)/\log_{10}(1.146) \approx 6.7$. So, the noise scales roughly with the 6.7^{th} power.

7.2. Frequency based acoustic analysis

Using the Fourier transform, the measurements in the time domain can be converted to the frequency domain. By doing so the transformed data can be analyzed in the frequency domain. The SPL analysis showed that the erosion increases the SPL, however the increase in severity of the erosion by an increase in the SPL does not show a correlation between the two. In this section, we will look at the effect of the different erosion models in the frequency domain.

7.2.1. Expected frequencies of airfoil self noise

In Section 2.4 of the report the different types airfoil noise are discussed. Based on the type of airfoil self-noise, the frequency that will be generated can be predicted using the Strouhal number. The Strouhal number expected for the frequency is taken from empirical data as described by Brooks et al. [59].

Noise Source	Characteristic Length L	Strouhal Range	Frequency Formula
TBL–Trailing Edge	Displacement thickness δ^*	0.1 – 1.0	$f = St \cdot \frac{U}{L}$
LBL Vortex Shedding	Thickness t	0.2 – 0.3	$f = St \cdot \frac{U}{L}$
Deep Stall	Separation bubble size	0.05 – 0.4	$f = St \cdot \frac{U}{L}$
Late Stall	Separation bubble length	0.05 – 0.3	$f = St \cdot \frac{U}{L}$
Trailing Edge Bluntness	Bluntness dimension	0.2 – 0.5	$f = St \cdot \frac{U}{L}$

Table 7.1: Characteristics of noise sources and their frequency formulation in terms of the Strouhal number.

Noise Source	$Re = 6 \times 10^5$	$Re = 7 \times 10^5$	$Re = 8 \times 10^5$
TBL–Trailing Edge (Untripped)	1,805.1 – 18050.5	2,312.5 – 23,124.6	2,836.5 – 28,364.5
TBL–Trailing Edge (Tripped)	1,554.2 – 15541.7	1,956.1 – 19,561.1	2,418.9 – 24,189.4
Laminar BL Vortex Shedding	93.3 – 140.0	109.3 – 164.0	125.3 – 188.0
Deep Stall (Laminar/Turbulent)	8.8 – 70.0	10.2 – 82.0	11.8 – 94.0
Late Stall (Laminar/Turbulent)	17.5 – 105.0	20.5 – 123.0	23.5 – 141.0
Trailing Edge Blunt Shedding	1,750 – 4,375	2,050 – 5,125	2,350 – 5,875

Table 7.2: Frequency ranges for different noise generation mechanisms at various Reynolds numbers $\alpha_t = 14°$.

Cavity noise

To estimate the pressure perturbation frequencies in a grazing cavity flow, the Rossiter formula was used. This semi-empirical model captures the feedback loop between acoustic waves and flow instabilities over an open cavity. Calculations were performed for two cavity depths, representing the cavity length L, at three different freestream velocities. Due to the high frequency only the first mode was considered, the results are shown in Table 7.3.

Cavity Type and Depth L (mm)	Re_c	**Frequency f (Hz)**
Pit cavity ($L = 0.2\ mm$)		
	8×10^5	94,300
	7×10^5	83,365
	6×10^5	72,040
Gouge cavity ($L = 0.4\ mm$)		
	8×10^5	47,150
	7×10^5	41,683
	6×10^5	36,020

Table 7.3: Rossiter frequencies for the first mode at different cavity depths and Re_c.

For the pit and gouge erosion features, the Helmholtz resonance was also calculated, and the resonant frequencies of these erosion features are $93,762$ and $41,700$ Hz. The reason for this is that the size of the pits and gouges is relatively small and shallow. Given that the Nyquist frequency of the measurement equipment is 24 kHz, it is not possible to measure the acoustic effects at the frequencies predicted accurately.

7.3. Influence of erosion models on the PSD

In Figure 7.4 the power spectral density of all damage stages is shown under the test conditions of $Re_c \approx 8 \times 10^5$. What can be seen is that the power of the frequencies between 100 Hz and 10 kHz is significantly lower than the rest of the models tested. In the figure the erosion models DL2, DL3, and DL4 all show significant divisions from the clean condition.

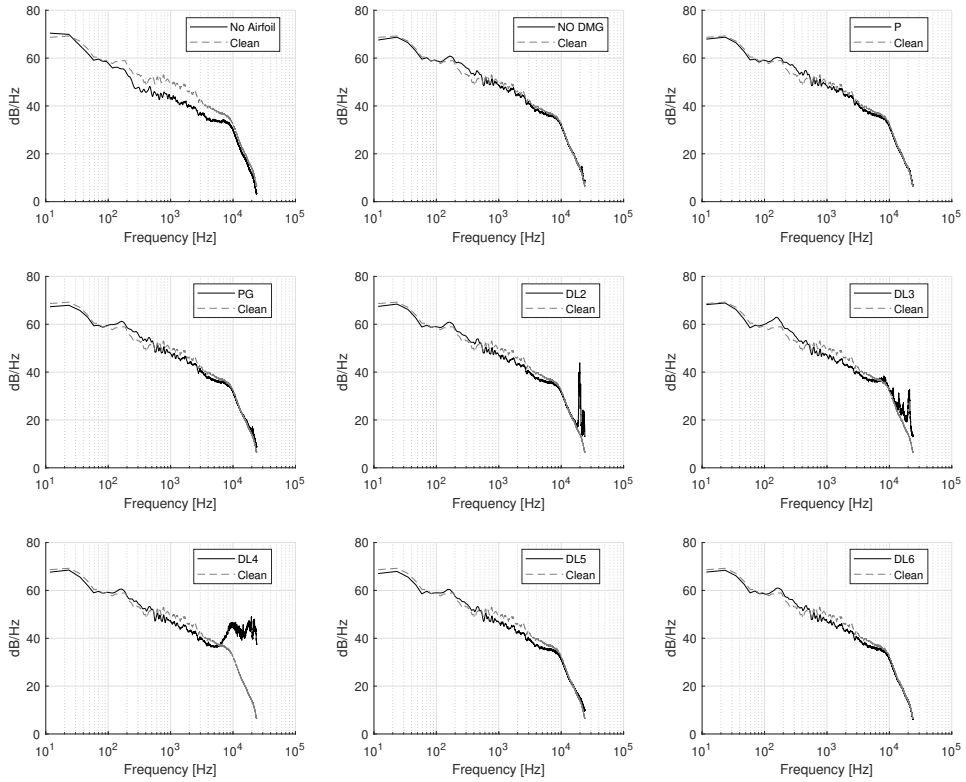

Figure 7.4: PSD's for all erosion models on the DU97-W-300 airfoil at $Re_c \approx 8 \times 10^5$ at $\alpha_t = 14°$

7.3.1. Wind tunnel noise

The first experimental runs were dedicated to measuring the noise that the wind tunnel itself produces. These tests where carried out with the wind tunnel angle set to the same angle as if the test was carried out with the airfoil mounted to maintain an equal comparison with the other erosion models. In Figure 7.5 the PSD of the wind tunnel without any airfoil and with the clean airfoil is shown. What can be seen in the figure is that the general shapes of the PSD's are similar to each other. This shows us that a significant amount of the acoustic power, especially at lower frequencies, is a result of the noise generated by the wind tunnel itself. The clean airfoil with no damage applied to it elevates the noise in the frequency range, but there are no specific spikes in power at a specific frequency. The difference in power of the plot shows a relatively constant plot; however, after a frequency of 10 kHz the difference between the Clean Airfoil and the No Airfoil case, the gap becomes smaller. Prior to the 10 kHz, the difference between the clean airfoil and no airfoil is around 2 dB or lower. However, between the frequencies of 1 kHz and 10 kHz the difference is roughly 5 dB. This shows that the noise the presence of the clean airfoil introduces is within that frequency range.

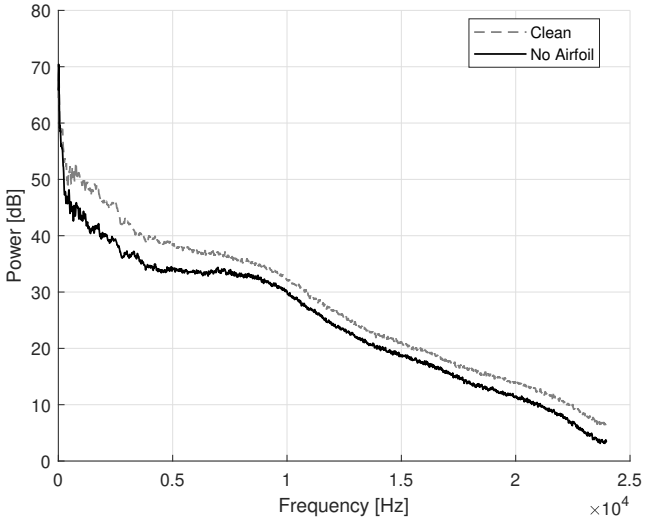

Figure 7.5: PSD comparison between Clean airfoil and the empty wind tunnel for the DU97-W-300 airfoil at $Re_c \approx 8 \times 10^5$ at $\alpha_t = 14°$

Taking a closer look at the frequencies where the airfoil produces noise using the beamforming algorithm in Figure 7.6. From the figure, it can bee seen that in the No Airfoil case, the noise has a lower power than that compared to the Clean case. Additionally, in the No airfoil case it can be seen that the noise is centered in the middle of the wind tunnel $y = 0$ m and becomes more intense in chord wise direction $x = 0$ m.

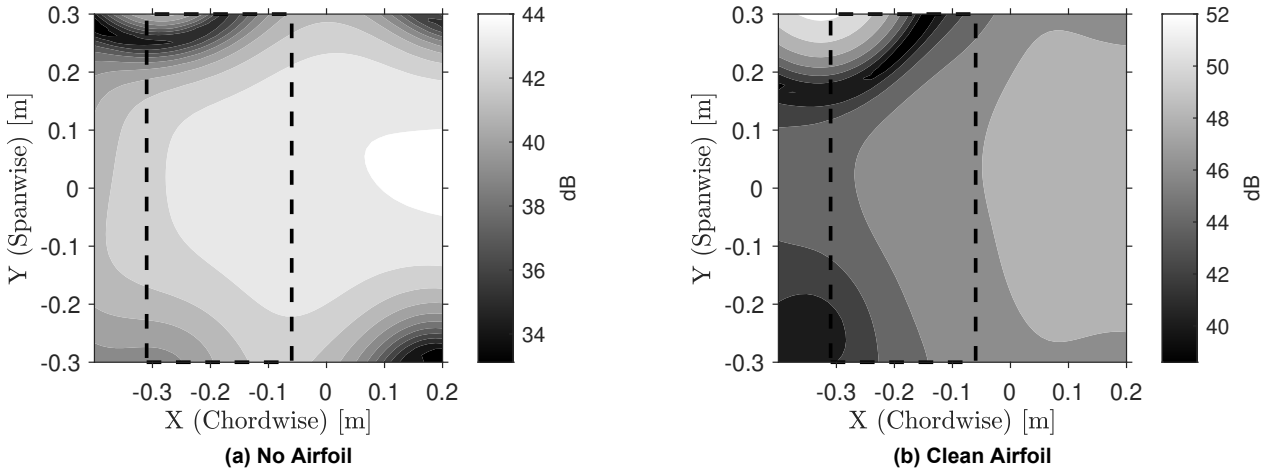

Figure 7.6: One-third octave beamforming maps comparing No Airfoil vs. Clean model of the DU97-W-300 airfoil at ($f_c = 3,175$ Hz, $Re_c \approx 8 \times 10^5$, $\alpha_t = 14°$)

What can be seen in both cases is that at the leading edge, where the airfoil contacts the wind tunnel, a noise source is located. This is present in both cases, the noise source is deemed to be a result of the construction of the wind tunnel.

Low frequency

As shown in the PSD's in Figure 7.4, the lower frequencies are the most powerful in all acoustic measurements, the difference between different erosion models is minimal, and thus what was concluded was that the low-frequency effects seen in the PSD's for all erosion models are that the noise is caused by the wind tunnel itself. This is corroborated by the Figure 7.7 where the beam forming plot at the frequency bin corresponding to the center frequency of 500 Hz.

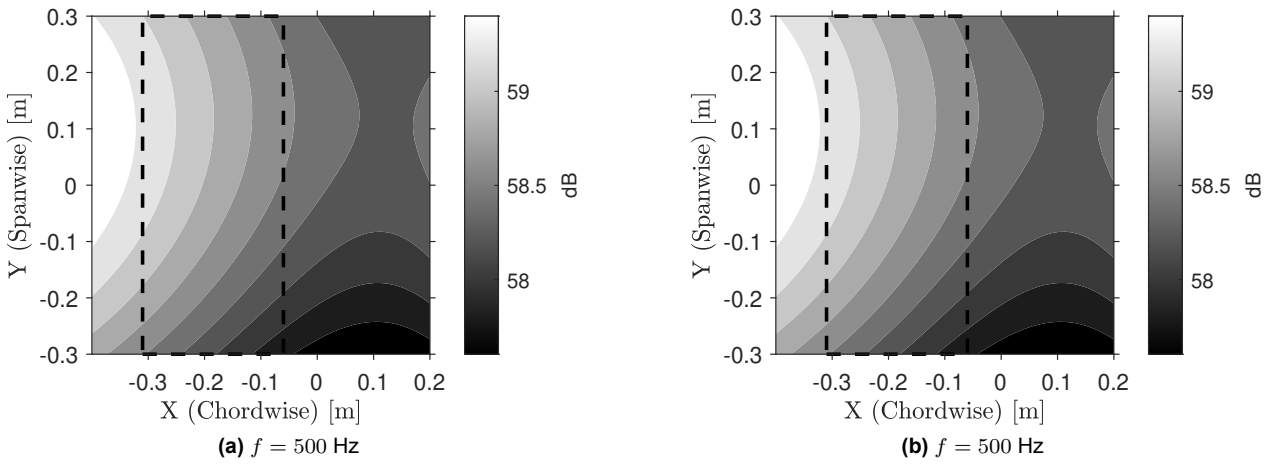

(a) $f = 500$ Hz **(b)** $f = 500$ Hz

Figure 7.7: One-third octave beamforming maps comparing No Airfoil vs. Clean model on the DU97-W-300 airfoil at ($f_c = 500$ Hz, $Re_c \approx 8 \times 10^5$, $\alpha_t = 14°$)

The wind tunnel itself produced a low frequency noise, the effects of the laminar boundary layer vortex shedding, and stall is hard to identify. This is predicted to occur at low frequencies, in the analysis of the lowest frequency bin; $f_c = 500$ Hz, because of this with the current algorithm there is not an ability to distinguish between lower frequency ranges, due to the block size.

Exit nozzle noise

The wind tunnel facility has both a closed test section and an open test section, which are placed one after another. At the point where the closed test section ends and the open test section begins, the flow experiences an abrupt change as the flow becomes unbounded in the Z direction. The transition from the closed wind tunnel section to the open section is shown in Figure 7.8

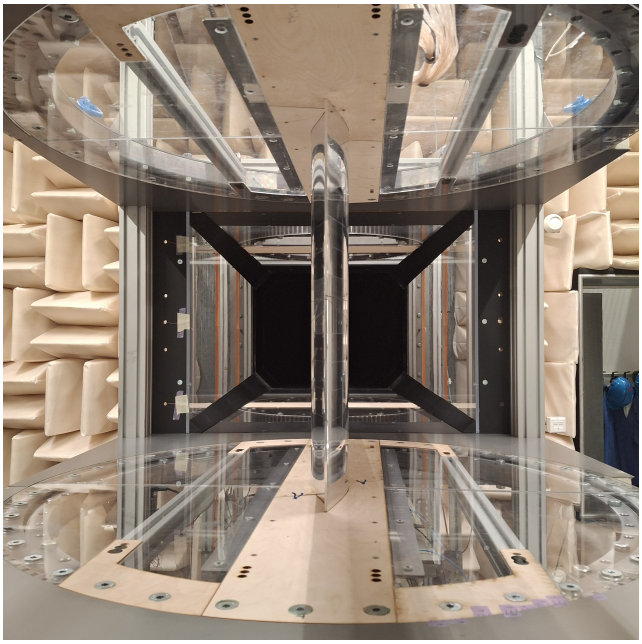

Figure 7.8: Illustration of abrupt change that causes wind tunnel noise

The low frequency noise as shown in all damage stages seems to originate from the wind tunnel itself, especially from the region upstream of the airfoil model, where the tunnel transitions from a closed section to an open section.

Noise source leading edge and wind tunnel
In many of the beamforming maps, a large peak at the top and bottom of the leading edge where the airfoil contacts the tunnel. These peaks cause significant noise to be produced. In the construction of the model, there was a small gap between the airfoil and the wind tunnel as shown in Figure 7.9.

Figure 7.9: Image of small gap between the airfoil and the wind tunnel

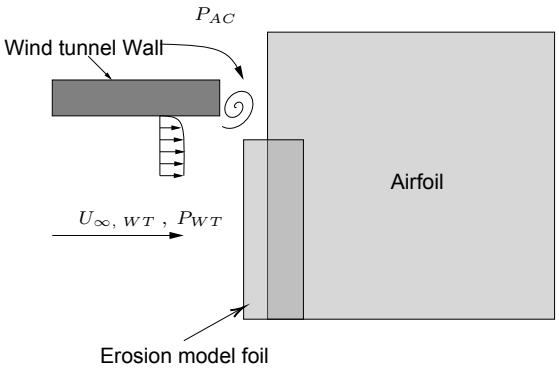

Figure 7.10: Flow behavior at gap between airfoil and wind tunnel

This gap could explain the noise generated at this position. Due to the wall, there is a boundary layer present at the point where the gap between the leading edge and the wind tunnel. Due to the length of the wind tunnel, and the imperfect transition between the closed and open test section. The flow at this section is likely turbulent. In addition to this, there is a static pressure difference at this point, the flow of the wind tunnel and the static pressure in the acoustic chamber are different from each other. Due to this pressure difference and the unsteady flow behavior in the turbulent boundary layer at the wall.

The noise that resulted at the gaps between the airfoil model and the wind tunnel mounting plates was over a wide range of frequencies mostly above $3,000$ Hz. In Figure 7.11 the noise source is shown at the leading and trailing edges where the airfoil comes into contact with the airfoil.

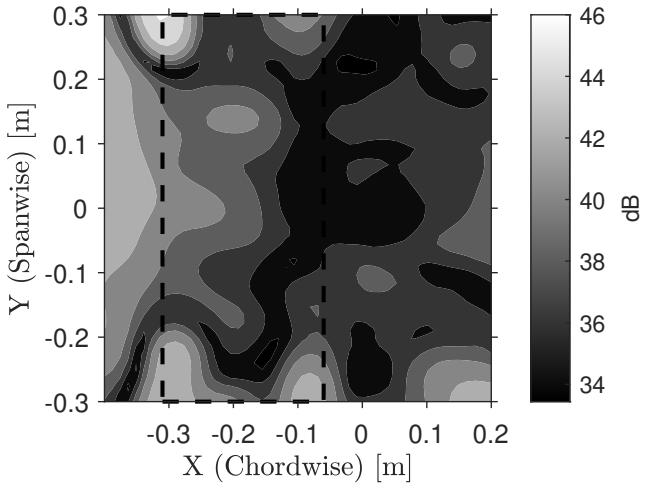

Figure 7.11: One-third octave beamforming maps of the Clean DU97-W-300 airfoil at ($f_c = 8,000$ Hz, $Re_c \approx 8 \times 10^5$, $\alpha_t = 14°$)

7.3.2. Acoustic effect No Damage model

To see the effect of the undamaged foil that was used to model the damage, the clean airfoil was compared to the No DMG model. What can be seen from these results in Figure 7.12 is that the general curve is quite similar to the airfoil. However, there is a difference in the power of the signal up to the frequencies of $8,000$ Hz where the power of the No DMG model is lower compared to that of where the Clean model airfoil. After that range, the power of the signal is slightly but consistently higher. At $f_c = 21,400$ Hz there is a peak for the No DMG case. The SPL of the clean airfoil compared to the No DMG model is slightly higher.

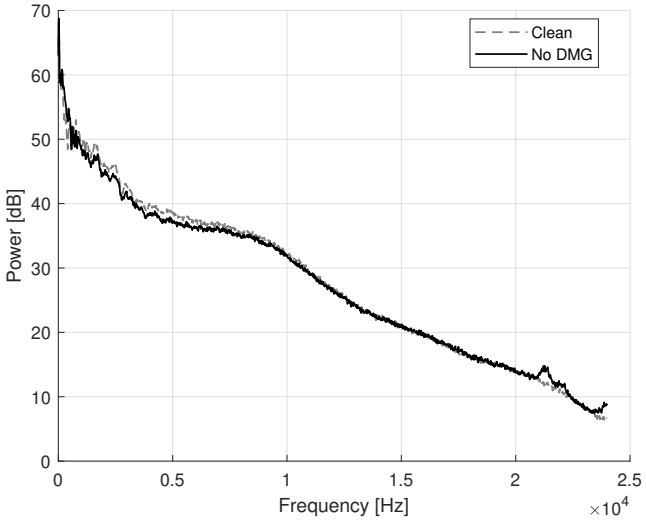

Figure 7.12: PSD comparison between Clean and No DMG erosion models on the DU97-W-300 airfoil at $Re_c \approx 8 \times 10^5$ $\alpha_t = 14°$

In Figure 7.13 the beamforming plot of the No DMG case and the Clean case are shown. What can be seen in 7.13a is that at the trailing edge of the No DMG foil a noise source is present. The noise source is located between $y = 0.05 - 0.23$ m. This noise source is not present in the clean airfoil case shown in Figure 7.13b.

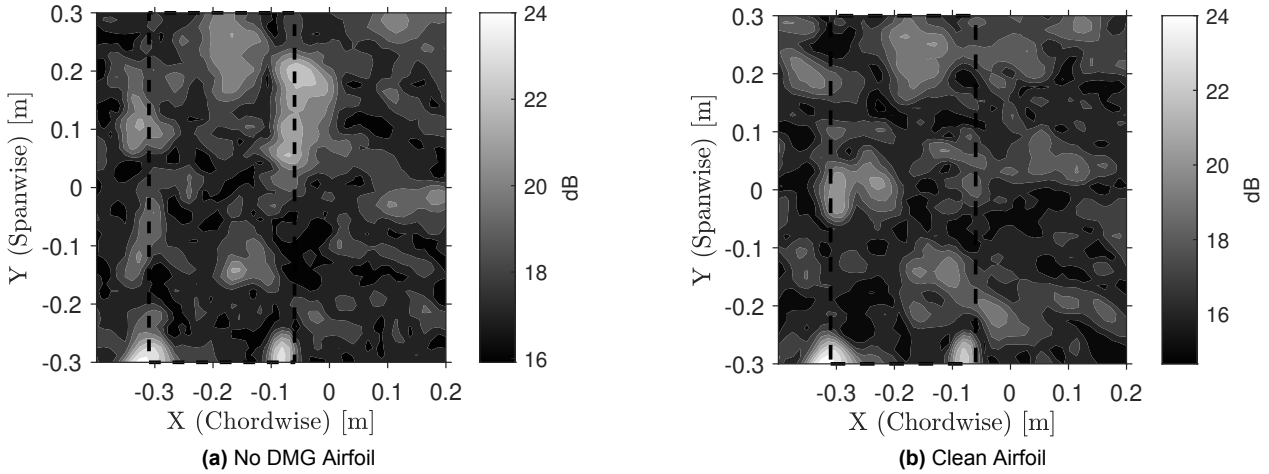

(a) No DMG Airfoil **(b)** Clean Airfoil

Figure 7.13: One-third octave beamforming maps comparing Clean vs. No Damage model on the DU97-W-300 airfoil at ($f_c = 20,159$ Hz, $Re_c \approx 8 \times 10^5$, $\alpha_t = 14°$)

As the noise source is not equally distributed over the entire trailing edge of the airfoil, the effect is not a result of the tape applied to the airfoil. However, in the application of the tape, a defect was found at this height, this can be seen in Figure 7.14 where an air bubble was present. Due to the effect found at this height and the effect shown in the beamforming there seems to be a correlation.

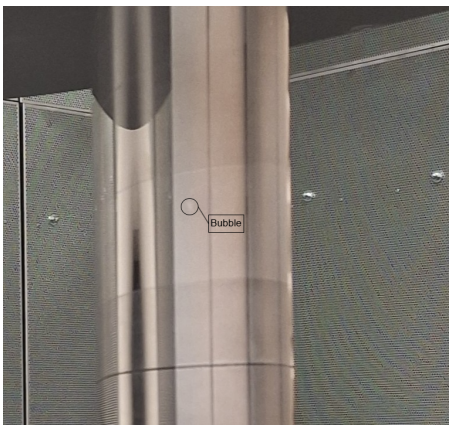

Figure 7.14: Defect in application

The turbulent boundary layer trailing edge noise of the No DMG model is better depicted in the Figure 7.15 where the beamforming plot at $f_c = 8,000$ Hz shown and compared to the Clean airfoil at the same conditions. What can be seen is that besides the increase in TE noise at the spanwise location of the defect, is that the general TE noise of the No DMG model does increase.

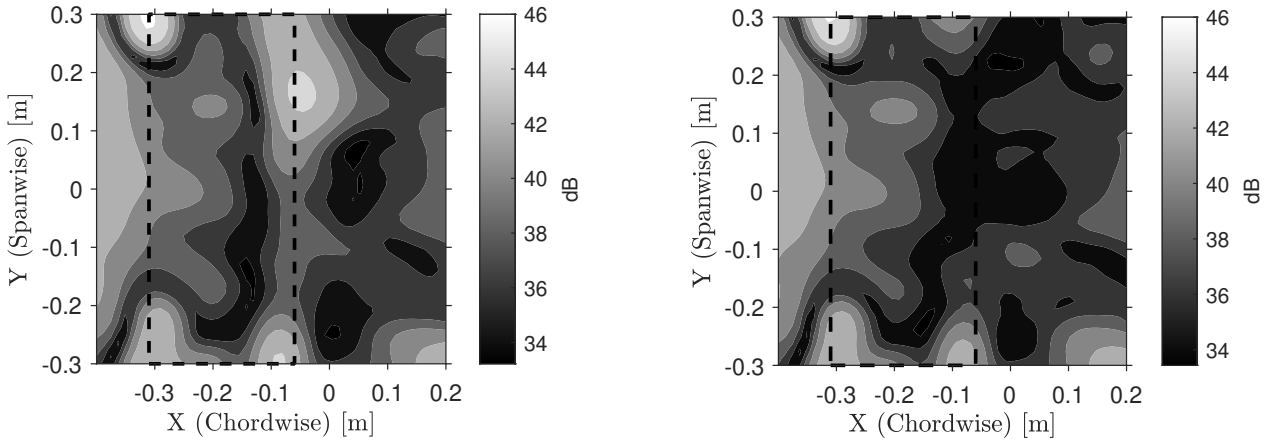

(a) No DMG Airfoil **(b)** Clean Airfoil

Figure 7.15: One-third octave beamforming maps comparing Clean vs. No Damage model on the DU97-W-300 airfoil at ($f_c = 8,000$ Hz, $Re_c \approx 8 \times 10^5$, $\alpha_t = 14°$)

7.3.3. Effect distributed roughness models P and PG

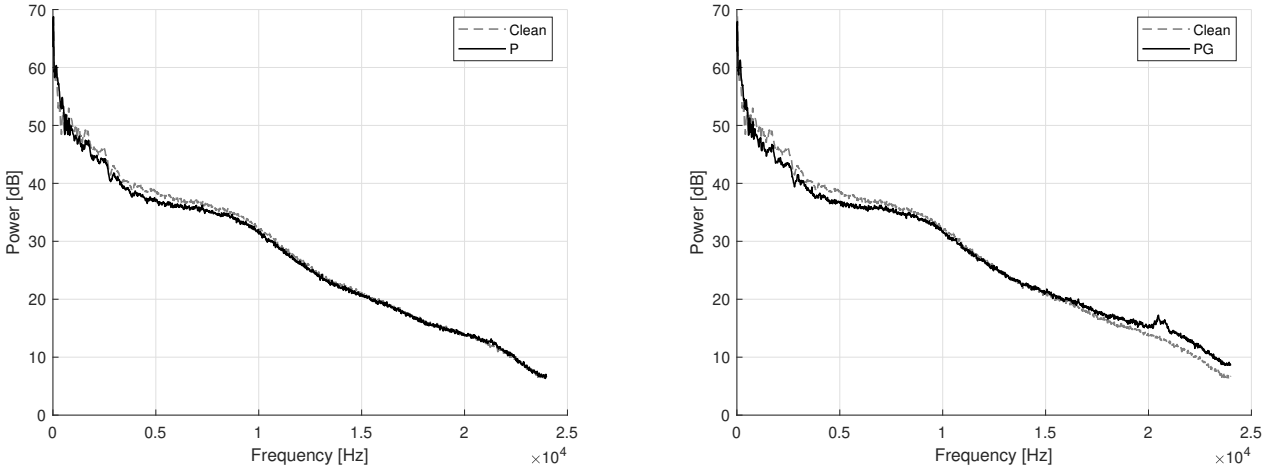

(a) A **(b)** Clean airfoil

Figure 7.16: PSD comparison between P and PG erosion models on the DU97-W-300 airfoil at $Re_c \approx 8 \times 10^5$ $\alpha_t = 14°$

In the Figure 7.16 the PSD for the erosion model P and PG are shown. Around $f_c = 20,159$ Hz the erosion model PG shows a distinctive peak. The beamforming map around this frequency bin is shown in 7.17. As shown in the figure, there is a distinctive region of noise originating from the leading edge of the airfoil, which is only present in the PG erosion case. The erosion model P and Clean model do not show any form of noise originating at the leading edge.

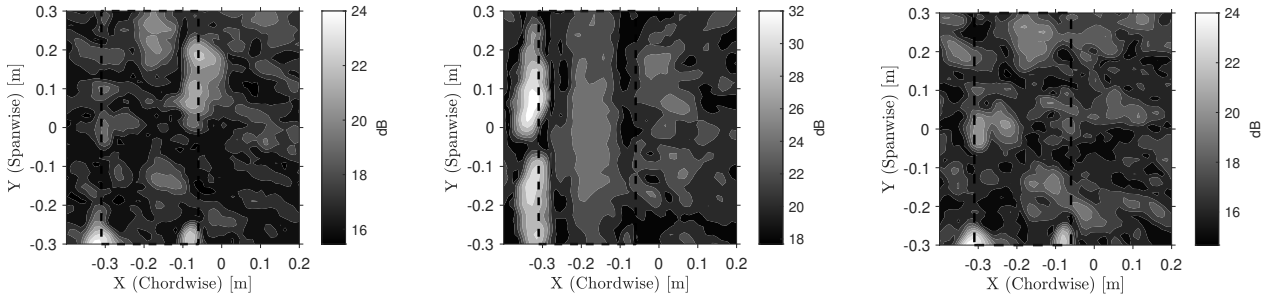

(a) Erosion model P **(b)** Erosion model PG **(c)** Erosion model Clean

Figure 7.17: One-third octave beamforming map comparison of P- vs. PG-erosion model vs. Clean on the DU97-W-300 airfoil at ($f_c = 20,159$ Hz, $Re_c \approx 8 \times 10^5$, $\alpha_t = 14°$)

Figure 7.18 shows the beamforming map for a frequency bin centered around $8,000$ Hz. At this frequency bin what can be seen is that the erosion stages P and PG both show higher trailing edge noise, which is most likely caused by the turbulent boundary layer. What can be concluded is that the turbulent boundary layer, trailing edge noise is more intense as a result of the LEE model.

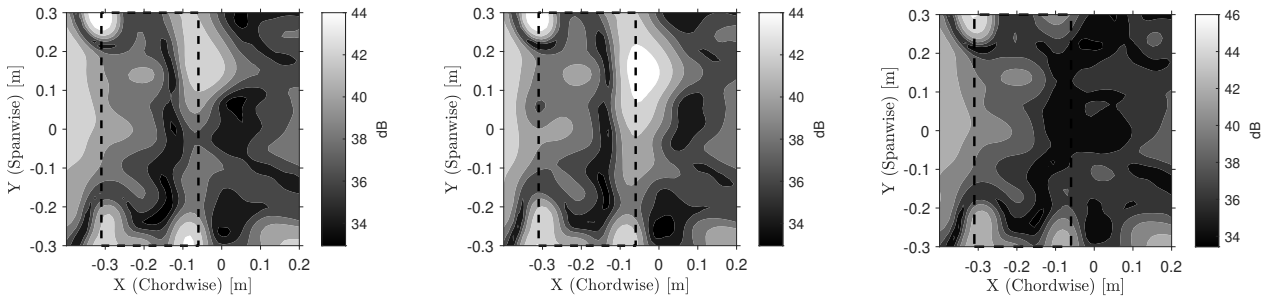

(a) Erosion model P **(b)** Erosion model PG **(c)** Erosion model Clean

Figure 7.18: One-third octave beamforming map comparison of P vs. PG erosion model vs. Clean DU97-W-300 airfoil at ($f_c = 8,000$ Hz , $Re_c \approx 8 \times 10^5$, $\alpha_t = 14°$)

7.3.4. Erosion model DL2

In Figure 7.19 the PSD of the DL2 erosion stage is shown. What can be clearly seen in the figure is a large peak in the power of the signal around 20 kHz. The frequency around 20 kHz has a power of 44 dB.

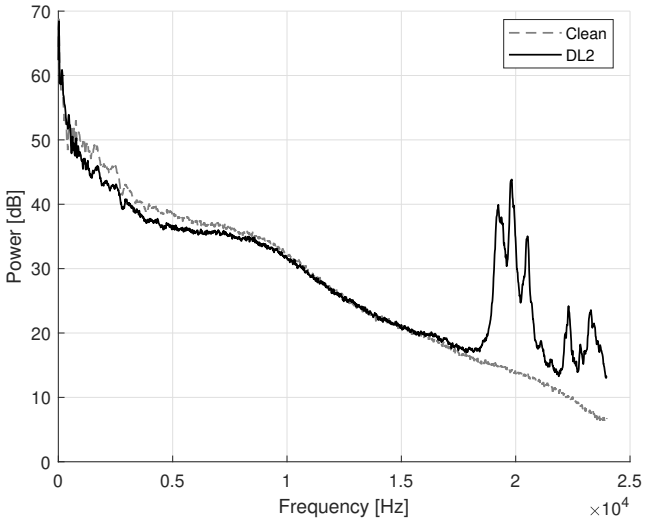

Figure 7.19: PSD comparison between Clean and DL4 at $Re_c \approx 8 \times 10^5$ $\alpha_t = 14°$

Figure 7.20 shows the one-third octave beamforming maps of both the DL2 and the Clean case. What can be seen is that the highest intensity of sound is originates where the leading edge of the airfoil meets the rotation disk of the wind tunnel. Besides this peak there are no distinctive noise patterns shown and because of this the increased power of the frequency is deemed to originate from the interaction between the wall and the airfoil. This behavior was also seen at for the peaks located between the frequencies of 18 kHz and 24 kHz.

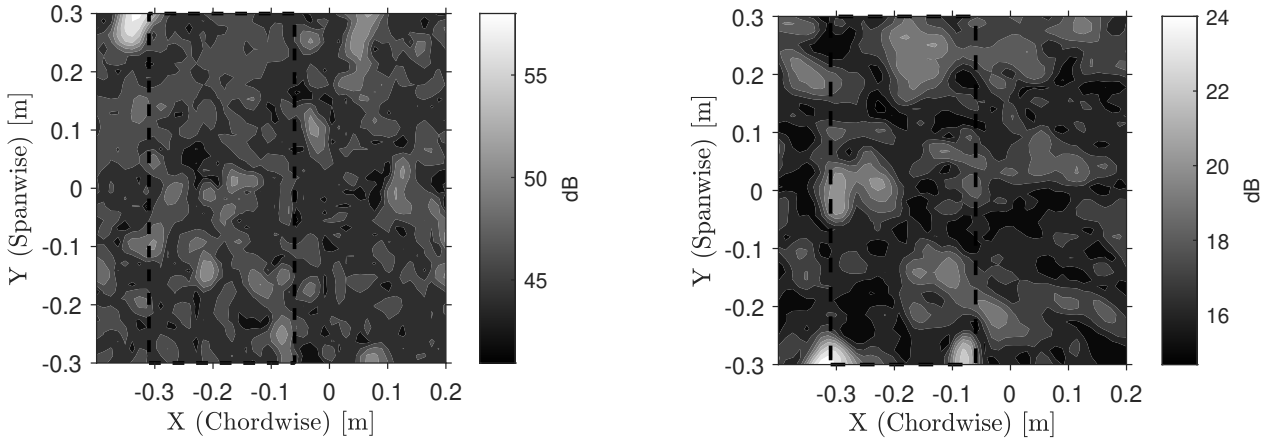

(a) Erosion stage DL2 **(b)** Erosion stage Clean

Figure 7.20: One-third octave beamforming maps comparing DL2 erosion model vs. Clean on the DU97-W-300 airfoil at ($f_c = 20,159Hz$, $Re_c \approx 8 \times 10^5$, $\alpha_t = 14°$)

Similar to the DL3 erosion model, the DL4 erosion model also shows an increase in trailing edge noise at $f_c = 8,000$ Hz, compared to that of the clean case. This is shown in Figure 7.21

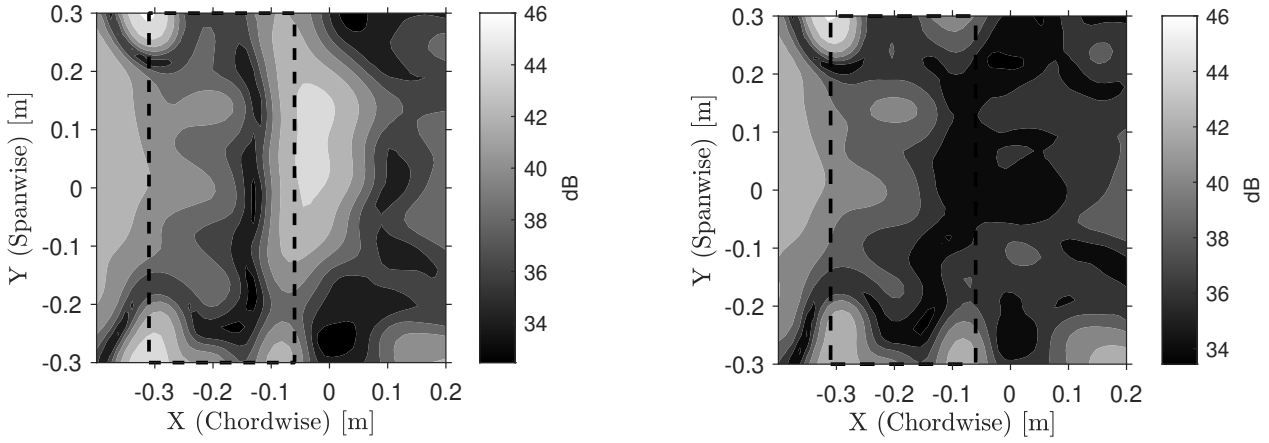

(a) Erosion model DL2 **(b)** Clean airfoil

Figure 7.21: One-third octave beamforming maps comparing DL2 erosion model vs. Clean on the DU97-W-300 airfoil at ($f_c = 8,000$ Hz , $Re_c \approx 8 \times 10^5$, $\alpha_t = 14°$)

7.3.5. Erosion model DL 3

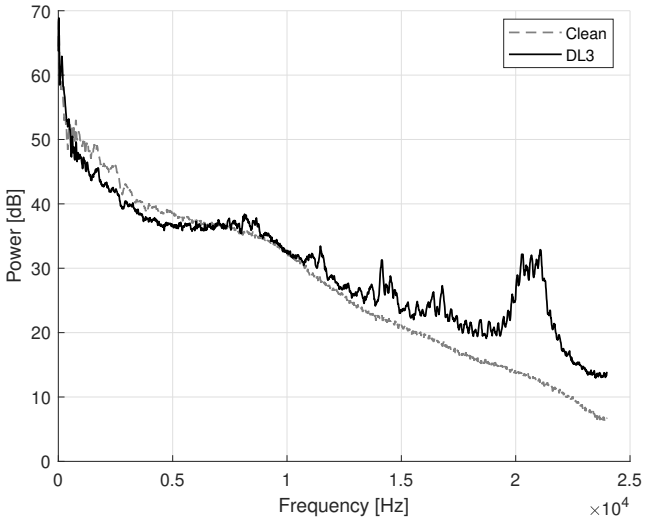

Figure 7.22: PSD comparison between Clean and DL3 erosion model at ($Re_c \approx 8 \times 10^5$, $\alpha_t = 14°$)

The PSD of the DL3 erosion stage measurement show peaks in power around the frequencies of 8,000 Hz, 11,400 Hz, 14,100 Hz, 16,800 Hz, and 20,600 Hz. In Figure 7.23 the third octave beamforming plot is shown of the DL3 and Clean condition at the frequency bin centered around $f_c =$ 12,699 Hz. This beamforming map is similar to the other peaks in the frequencies and can be found in the appendix E. Here, the peaks in the power signal at these frequencies do not show the power peaks distributed over the airfoil as a result of the damage model, but as a localized peak as a result of the interaction between the wind tunnel and the airfoil in combination with the damage model. The beamforming map reveals that this noise produced originates from the point where the leading edge of the airfoil is in contact with the wind tunnel itself. This is like a side effect of the tape mounted at the top to retain the foil, and thus, it is not a result of the LEE.

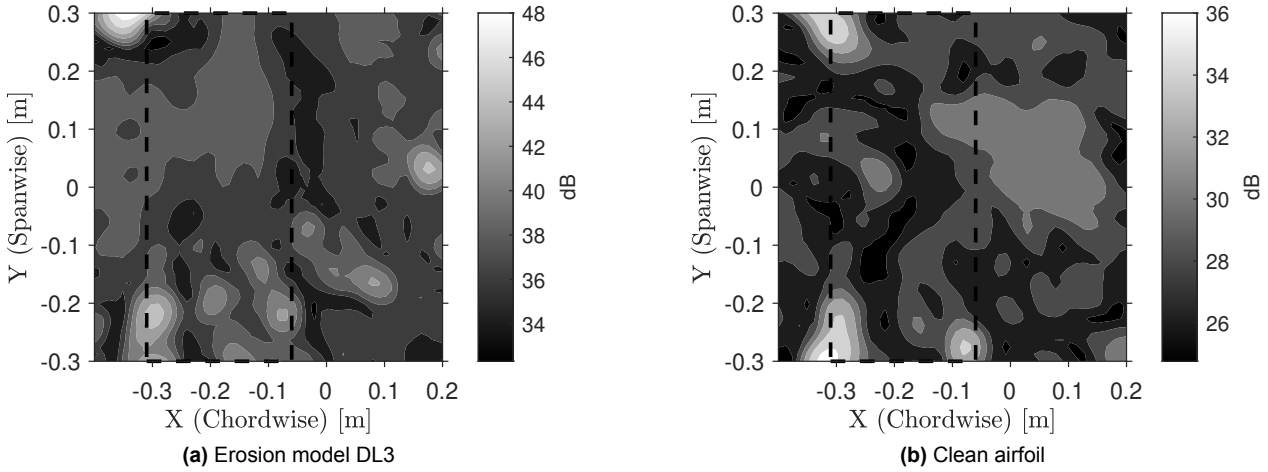

(a) Erosion model DL3 **(b)** Clean airfoil

Figure 7.23: One-third octave beamforming maps comparing DL3 erosion model vs. Clean on the DU97-W-300 airfoil at ($f_c = 12,699$ Hz , $Re_c \approx 8 \times 10^5$, $\alpha_t = 14°$)

What is not shown in the PSD plot in Figure 7.22 is a peak at the bin $f_c = 8,000$ Hz. In the beamforming maps of the P and PG erosion model this frequency bin showed the TBL-TE noise, This can also be seen for the DL3 in Figure 7.24 where two spots ar the trailing edge show increased power, what can be concluded for this is that the DL3 erosion model does increase the TBL-TE noise.

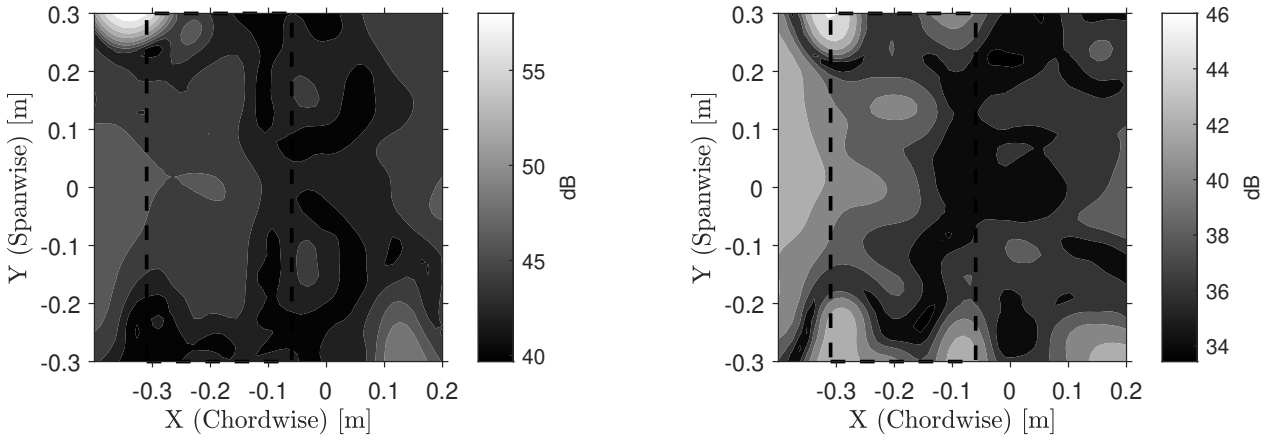

(a) Erosion model DL3 **(b)** Clean airfoil

Figure 7.24: One-third octave beamforming maps comparing DL3 erosion model vs. Clean on the DU97-W-300 airfoil at ($f_c = 8,000$ Hz , $Re_c \approx 8 \times 10^5$, $\alpha_t = 14°$)

The beamforming map for the center bin frequency of $f_c = 3,175$ Hz in Figure 7.25 shows that the LEE does exhibits a difference in trailing edge noise, which was not seen for the Clean case. Based on the frequency of this acoustic disturbance, the noise can be either a result of a TBL-TE noise or due to the bluntness of the trailing edge itself.
In the figure the Clean condition is shown, the noise at the trailing edge in the DL3 erosion model is higher than that in the clean case. The noise shown in the clean case after the trailing edge is also elevated and the region reaches the edge of the region of interest. Therefore, erosion model DL3 shows at this frequency bin the TBL-TE noise whereas the Clean case better depicts the trailing edge bluntness vortex shedding noise, as a larger region behind the airfoil.

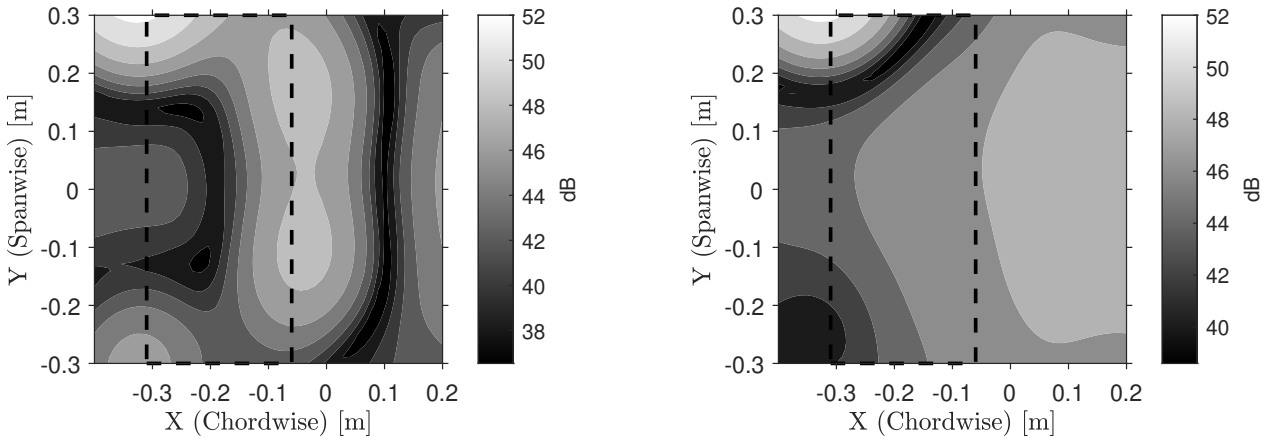

(a) Erosion model DL3 **(b)** Clean airfoil

Figure 7.25: One-third octave beamforming maps comparing DL3 erosion model vs. Clean on the DU97-W-300 airfoil at ($f_c = 3,175$ Hz , $Re_c \approx 8 \times 10^5$, $\alpha_t = 14°$)

7.3.6. Erosion model DL4

In Figure 7.26 the PSD plot comparing the Clean case and the DL4 case is shown. This case shows the largest deviation from the clean case out of all tested damage models. As shown in the plot the largest offset is present at the frequencies above 6000 Hz and remains high compared to the clean up to the Nyquist frequency.

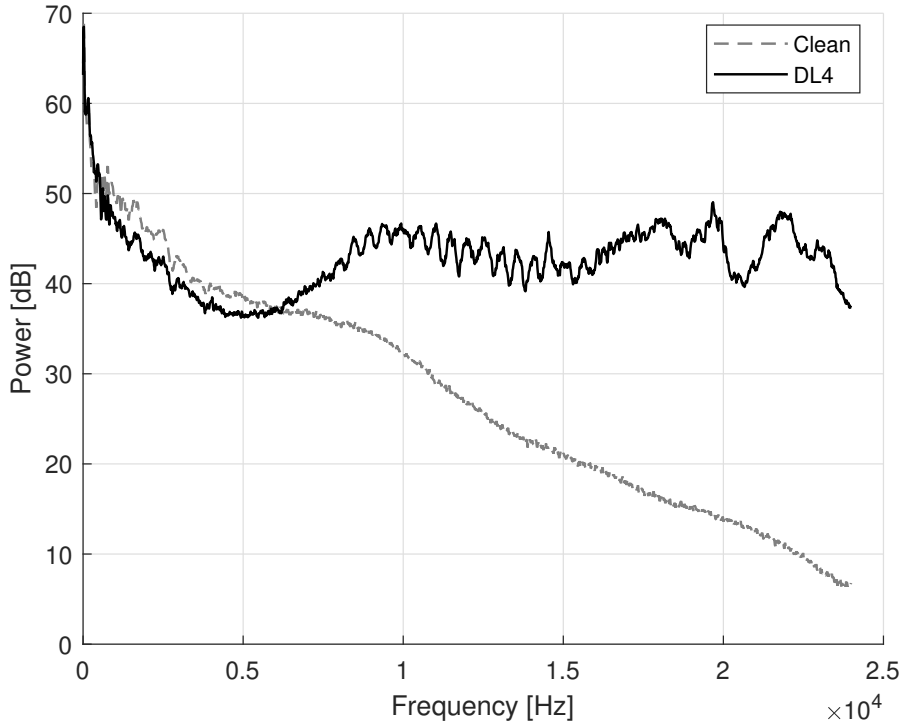

Figure 7.26: PSD comparison between Clean and DL4 at $Re_c \approx 8 \times 10^5$ $\alpha_t = 14°$

In Figure 7.27 beamforming images for the DL4 and the Clean case are shown. What can be clearly seen is that at the leading edge of the airfoil there is significant noise production within the third octave bin $f_c = 8,000$ Hz. The noise produced at the leading edge of the airfoil at a frequency around $8,000$ Hz and is not limited to the top and bottom of the airfoil, thus not an effect of the interaction between the wind tunnel and the airfoil.

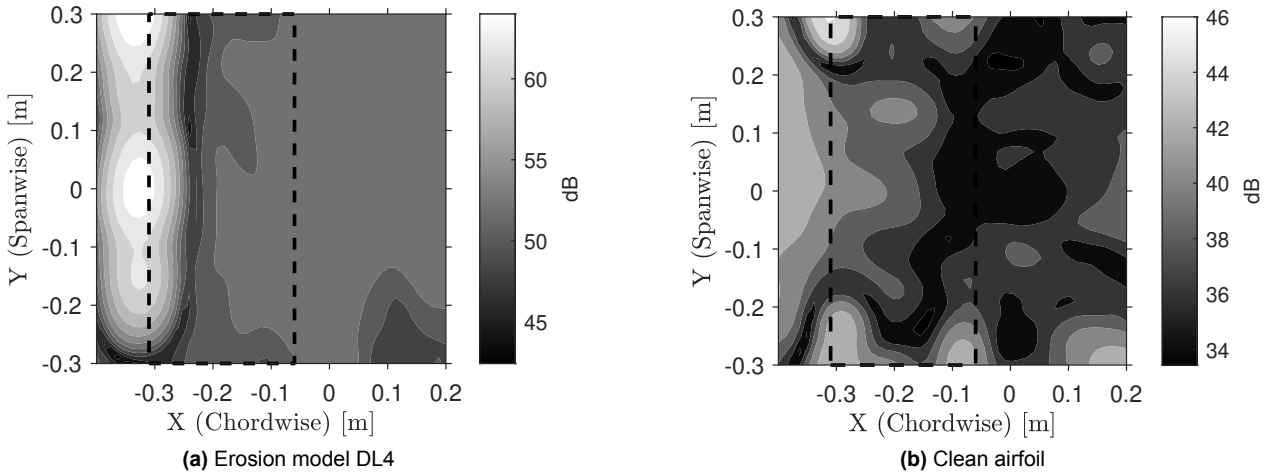

(a) Erosion model DL4

(b) Clean airfoil

Figure 7.27: One-third octave beamforming maps comparing DL4 erosion model vs. Clean on the DU97-W-300 airfoil at ($f_c = 8,000$ Hz , $Re_c \approx 8 \times 10^5$, $\alpha_t = 14°$)

Another elevated level in the PSD is around 16 kHz. Figure 7.28 shows the beamforming at this frequency.

Similarly to the result at $8,000$ Hz, the result shows that the erosion model DL4 produces significant noise at the leading edge of the airfoil comparable to that of the clean model. This pattern holds for the entire elevated range up to the Nyquist frequency. The results for all beamforming maps are shown in Appendix E.

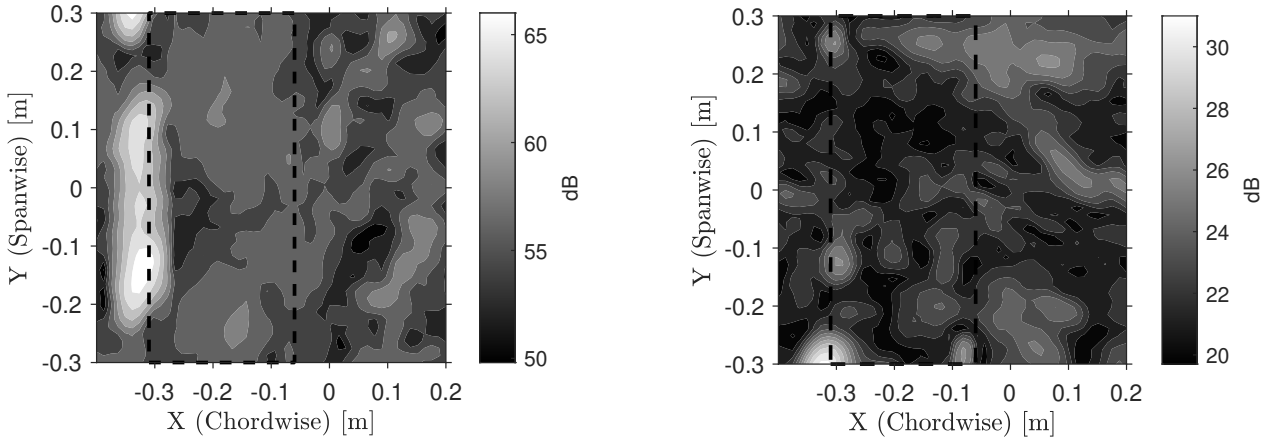

(a) Erosion model DL4 **(b)** Clean airfoil

Figure 7.28: One-third octave beamforming maps comparing DL4 erosion model vs. Clean on the DU97-W-300 airfoil at ($f_c = 16,000$ Hz , $Re_c \approx 8 \times 10^5$, $\alpha_t = 14°$)

For the frequencies above $8,000$ Hz, the beamforming maps are similar and show significant elevated power levels located at the leading edge of the airfoil. The power of the signal at the leading edge of the airfoil the noise at the trailing edge are more difficult to identify. However, when looking at a lower frequency bin $f_c = 1,587$ Hz, which is within the predictive bandwidth of the TBL-TE noise, an increase does show in noise at the trailing edge compared to the clean case.

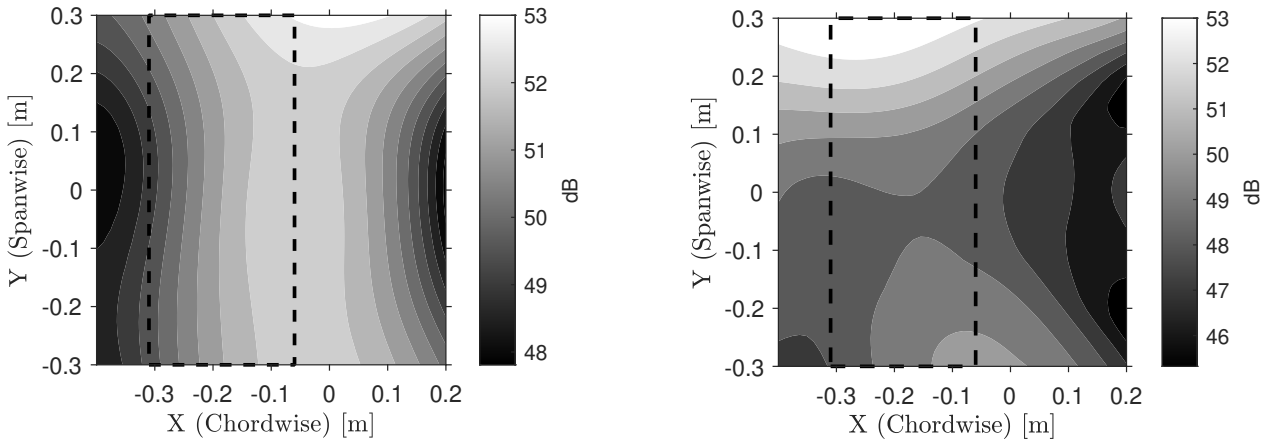

(a) Erosion model DL4 **(b)** Clean airfoil

Figure 7.29: One-third octave beamforming maps comparing DL4 erosion model vs. Clean on the DU97-W-300 airfoil at ($f_c = 1,587$ Hz , $Re_c \approx 8 \times 10^5$, $\alpha_t = 14°$)

7.3.7. Acoustic effect Re_k

In Figure 7.1 the sound pressure levels are shown, what can be seen is that the erosion models DL5 and DL6 have a lower SPL compared to the clean case as well as the DL3 case. A possibility for the SPL to be reduced is due to the turbulent boundary layer, where the flow is better able to adhere to the surface of the airfoil. Thereby, delaying boundary layer separation; however, because we are looking at the pressure side of the airfoil and separation most likely occurs on the suction side of the airfoil, and pressure distribution was not measured, this cannot be confirmed. The DL3, DL5 and DL6 erosion cases have the same delamination width, the difference between then being the depth of the features, and thereby increasing the value for Re_k.

The Figure 7.30 shows the PSD's of the three erosion models. The erosion models DL5 and DL6 do not show peaks as is present in the DL3 case. As discussed earlier, these peaks are not due to the erosion itself but a side effect of the erosion application and the interaction between the airfoil model and the wind tunnel wall.

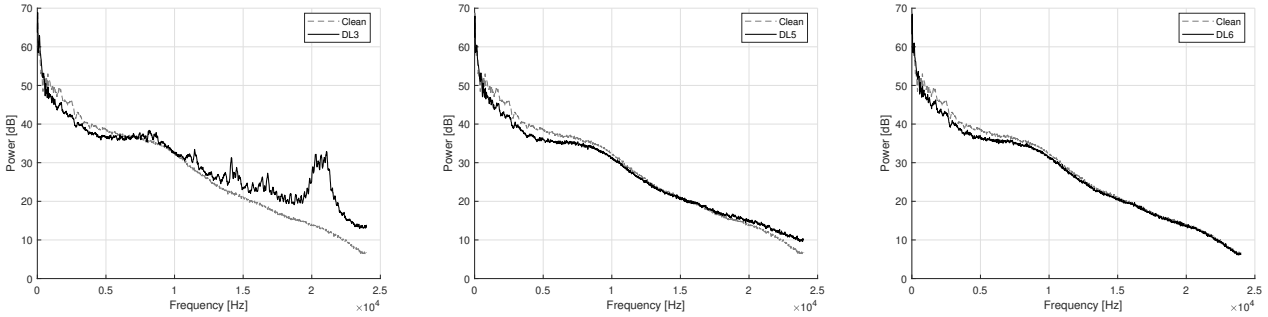

(a) Erosion model DL3 **(b)** Erosion model DL5 **(c)** Erosion model DL6

Figure 7.30: PSD comparison between DL3-, DL5- and DL6-erosion models at $Rec \approx 8 \times 10^5$ $\alpha_t = 14°$

Figure 7.31 shows the third octave beamforming maps for the bin $f_c = 4,000$ Hz for the erosion models DL3, DL5 and DL6. For all these cases, what can be seen is that noise is generated at the trailing edge. The power of the noise at the trailing edge does decrease as the Re_k decreases. The peak power at the trailing edge of airfoil is 48.6, 47 and 46 dB for the erosion models DL3, DL5 and DL6 respectively. This does indicate that the increased roughness does have an effect on TBL-TE noise.

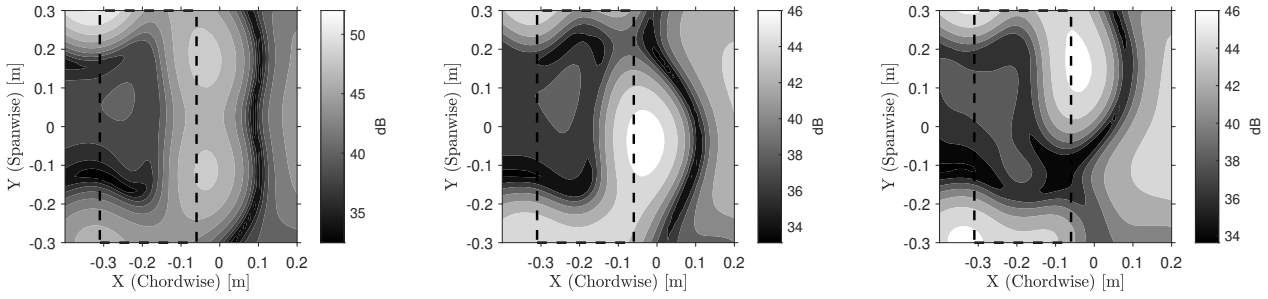

(a) Erosion model DL3 **(b)** Erosion model DL5 **(c)** Erosion model DL6

Figure 7.31: One-third octave beamforming maps comparing DL3-, DL5 and DL6 erosion models on the DU97-W-300 airfoil at ($f_c = 4,000$ Hz , $Re_c \approx 8 \times 10^5$, $\alpha_t = 14°$)

Part IV

Conclusion of results and future outlook

8

Conclusion and Discussion

This study was set up to investigate the impact of erosion of the leading edge of a wind turbine blade on acoustic noise signatures and whether it could be detected and quantified experimentally using acoustic measurement techniques. Thereby, employing the idea that these techniques could be used to evaluate the condition of the leading edge and aid in the maintenance of the turbine.
Using the aeroacoustic wind tunnel facility, wind tunnel experiments were performed on the DU97-W-300 airfoil, various damage models were constructed to attach to the leading edge of airfoil to simulate erosion conditions on the leading edge of the blade. Using a microphone array, the acoustic signatures of multiple erosion models were analyzed to quantify the aeroacoustic effects.

Acoustic measurement
The experiments showed that for the conditions tested at the anechoic wind tunnel facility, the different erosion models showed varying results and changed the acoustic signature of the airfoil. It was hypothesized that the erosion of the leading edge caused the boundary layer to transition and increase the noise at the trailing edge, and that the severity of the erosion increased the severity of the tripping effect of the boundary layer. The results show that this was the case, however, the models designed for this test were scaled and controlled and did not represent erosion as seen in the real world, since the experiments were conducted in an anechoic chamber the elevated acoustic signatures could be readily detected. A particularly interesting finding was the presence of leading edge noise in certain erosion models, particularly in erosion models DL4 and PG which aimed to show early stage delamination and pits and gouges defects. For some erosion models, it was found that the measured sound pressure level of the various damage stages caused a reduction in the overall sound pressure level. However, the measurements where affected by the gap between the airfoil and the tunnel itself this was a significant noise source.

Erosion models and scaling
The modeling of the erosion presented scaling challenges, where commonly the dimensionless number used for the scaling of airfoil experiments in wind tunnels is the chord based Reynolds number Re_c. The real world conditions of modern wind turbines achieve a Reynolds number far greater than is achievable in the acoustic wind tunnel at the University of Twente. Therefore, a different approach was taken in this research using the roughness height Reynolds number Re_k. In this approach, the flow of the wind tunnel was set at a certain value and the erosion features themselves where scaled to match the real world conditions.

Limitations
Airfoil
The airfoil used for the experiments was the DU97-W-300. This is an airfoil similar to that used in wind turbines, however, this type of airfoil is designed for a radial position closer to the root of the blade. The most noise is generated by the wind turbine is closer to the tip at a relative radial position around 90% of the blade. At this radial position the velocity of the blade is higher and the airfoils used at this position are generally thinner compared to that of the root. The DU97-W-300 has a relatively tick trailing edge, airfoils with a thinner trailing edge reduce the sound generated as a ticker trailing edge act as a bluff body making the scattering of the acoustics waves more efficient. Because of this the TBL-TE noise generated by the DU97-W-300 is easier to detect.

The airfoil was used because of the availability, and initially the scope of the project included the pressure measurements of the airfoil that this airfoil would allow for. But due to unforeseen challenges these measurements were unable to be preformed.

Setup challenges
The acoustic results showed challenges in the experimental setup itself, mainly the noise caused by the wind tunnel itself. What was seen was that the interaction between the airfoil and the wind tunnel caused significant noise sources where the leading edge of the airfoil and the tunnel met. This was likely due to the gap between the airfoil and the wind tunnel walls. Depending on the erosion model applied to the leading edge of the airfoil, the gap between the airfoil and the wind tunnel changed. For some erosion models specifically, the DL2 and DL3 case, significant peaks were noticed in the PSD of the measurements, but were determined to originate from the airfoil wind tunnel interaction.

Limited measurements
Because the study was limited to acoustic measurements, the effect of LEE was unable to measure the performance effects. Acoustic measurements alone could not determine whether the LEE caused by the separation of the flow.

Beamforming
The beamforming array was also placed on the pressure side of the airfoil, the reasoning behind this comes from a maintenance point of view, as a possible implementation of these techniques called for the placement of a microphone array on the tower structure of the wind turbine. The intensity of the noise is generally less on the pressure side of the airfoil. Besides this when a flow separation occurs, this tends to occur on the suction side of the airfoil, this could also result in noise but because we are looking at the pressure side, this could not be detected. The search grid used in the beamforming array focused on the trailing edge of the airfoil itself, and therefore, for the leading edge noise that was discovered in the erosion model DL4 and PG, the search grid was not in focus. The beamforming maps could likely have been improved by adjusting the grid to include this region more effectively.

Closing remarks
What was shown was that LEE does have an impact on the acoustic signature of the wind turbine blade and that it could possibly be used to a certain degree to evaluate the severity of the LEE of the wind turbine blade. As a common objection to the use of wind turbines is the noise they generate, research shows that the noise emitted by the wind turbine increases over time as a result of erosion. This can become a problem as during the installation of the wind turbine the noise generated might comply with the specifications and requirements set by regulatory agencies, but the degradation of the blade might result in noise that exceeds the limits set by authorities. For this reason, monitoring over the lifespan of the turbine can be useful for long-term compliance and acceptance by the surrounding communities. The results show that it is possible to detect leading edge erosion under the conditions tested in the experiments. However, these conditions do not perfectly emulate the operating conditions of a wind turbine. The simulation of the operating conditions of the wind turbine could not be scaled with the classical chord-based Reynolds number, therefore, instead of altering the flow conditions of the wind tunnel, the geometries of the simulated erosion were altered to match the roughness height Reynolds number Re_k. The significance of assessing the acoustic effects of erosion lies in its role within preliminary planning, where an acceptable noise level is established. However, it is possible that over time, noise levels may increase and potentially exceed these established thresholds.

9

Recommendations

This chapter provides a brief overview of the primary recommendations for the future continuation of this project.

Tunnel effects on acoustic measurements
During the wind tunnel experiment significant noise was noticed at the point where the airfoil meets the wind tunnel that is suspected to be a result of the gap between the two surfaces. This region could have been closed to eliminate the noise resulting from these gaps. This would have given better results for the sound pressure level, and the effect of Re_k on the acoustic signature would have been better.

Unperformed measurements critical to understanding LEE effects
During the thesis, the scope had to be reduced, and several valuable measurements were not carried out. The pressure distribution over the airfoil could have given insight into the possible suppression of the flow ever the airfoil. As each section of the wind turbine blade is designed to operate under maximum lift to drag ratio, the introduction of a surface disturbance at the leading edge might lead to flow separation (stall); by measuring the pressure distribution over the foil, this could have been determined using pressure measurements.
Hot wire measurements of the boundary layer at the trailing edge were also proposed. At the start of the project. By measuring this boundary layer thickness and the turbulence intensity, the effect of the LEE on the boundary layer could be compared using hot wire measurements.

Suboptimal airfoil choice
The DU97-W-300 airfoil used was also not ideal as the type of airfoil used in the experiments did not match the type of airfoil used at the radial position where erosion and noise are most prevalent at the leading edge. The use of a thinner airfoil, especially with a thinner trailing edge, may provide better insight in the origin of the type of noise lacking. As the expected frequencies for trailing edge bluntness vortex shedding and turbulent boundary layer trailing edge noise are both broadband noise that for the DU97-W-300 airfoil under these conditions are predicted to be in largely overlapping frequency ranges. The thick trailing edge of the airfoil used assisted in the sound generated at the trailing edge, for airfoils with thinner trailing edges the airfoil self noise might be more difficult to identify.

Scaling challenges
For LEE modeling, scaling was performed using the dimensionless number Re_k as the chord-based Reynolds number was unable to be achieved in the aeroacoustic wind tunnel facility at the University of Twente. This scaling is not perfect. Empirical models had to be used to approximate the velocity profile of the boundary layer and evaluate the velocity at the roughness height k. Furthermore, the depth scaling for the distributed roughness erosion models P and PG used the middle of the coverage of the features. For this scaling to be accurate using the Re_k the depth of each hole depending on the chord-wise position would have been specifically calculated. This was deemed impossible, as the construction of the erosion model was limited to the thickness of the adhesive foils used. This simplification was deemed to be acceptable as the depths were specified between a range of values.

More realistic delamination modeling
The shape of the erosion features was also simplified. The pits and gouges were modeled as cylinders, for pits that in real world conditions are relatively circular; the gouges, however, are often seen in real world conditions

as groves in the surface and are not circular. The delamination of the leading edge was modeled as a straight edge creating a curved trench-like shape. In real world conditions, the delamination does not present itself with a straight edge but has jagged edges. In addition to this, the delamination erosion feature does not exclusively exits on its own, as the erosion gradually worsens the surface overtime the surface of a delaminated surface will also include pits and gouges. In real erosion stages the boundary layer can be altered at the beginning of the leading edge, then the boundary layer will see another erosion feature , this interaction was not modeled as the erosion was scaled based on Re_k for a single erosion feature.

Alternative LEE monitoring methods

In addition to acoustic monitoring of wind turbine blades to assess the severity of leading edge erosion, another possible solution is to mount cameras to continuously monitor the state of blade degradation. These cameras could also be mounted on the tower structure of the wind turbine. To aid in the visual examination of the LEE the leading edge protection could be constructed using a layer approach. Where the LEE protection tape could be constructed of multiple colored layers of tape. In this idea, each colored layer corresponds to a certain depth, making visual damage inspection either by camera or by human inspection easy to quantify in terms of erosion depth.

References

[1] Centraal Bureau voor de Statistiek (CBS), *Elektriciteit; productie en verbruik, energiedragers*, https://opendata.cbs.nl/statline/#/CBS/nl/dataset/82610NED/table, Geraadpleegd op 15 juni 2025, 2024. [Online]. Available: https://opendata.cbs.nl/statline/#/CBS/nl/dataset/82610NED/table?ts=1617545569760.

[2] D. Maniaci, J. Paquette, and R. Clarke, "Technical report leading edge erosion classification system iea wind task 46 erosion of wind turbine blades technical report leading edge erosion classification system prepared for the international energy agency wind technology collaboration programme," 2022.

[3] F. Papi, G. Ferrara, and A. Bianchini, "Practical Considerations on Wind Turbine Blade Leading Edge Erosion Modelling and its Impact on Performance and Loads," en, *Journal of Physics: Conference Series*, vol. 1618, no. 5, p. 052 005, Sep. 2020, ISSN: 1742-6588, 1742-6596. DOI: 10.1088/1742-6596/1618/5/052005. [Online]. Available: https://iopscience.iop.org/article/10.1088/1742-6596/1618/5/052005 (visited on 05/09/2025).

[4] W. Han, J. Kim, and B. Kim, "Effects of contamination and erosion at the leading edge of blade tip airfoils on the annual energy production of wind turbines," en, *Renewable Energy*, vol. 115, pp. 817–823, Jan. 2018, ISSN: 09601481. DOI: 10.1016/j.renene.2017.09.002. [Online]. Available: https://linkinghub.elsevier.com/retrieve/pii/S0960148117308649 (visited on 05/26/2025).

[5] R. Kyle, F. Wang, and B. Forbes, "The effect of a leading edge erosion shield on the aerodynamic performance of a wind turbine blade," en, *Wind Energy*, vol. 23, no. 4, pp. 953–966, Apr. 2020, ISSN: 1095-4244, 1099-1824. DOI: 10.1002/we.2466. [Online]. Available: https://onlinelibrary.wiley.com/doi/10.1002/we.2466 (visited on 05/09/2025).

[6] A. Tempelis and L. Mishnaevsky, "Surface roughness evolution of wind turbine blade subject to rain erosion," en, *Materials & Design*, vol. 231, p. 112 011, Jul. 2023, ISSN: 02641275. DOI: 10.1016/j.matdes.2023.112011. [Online]. Available: https://linkinghub.elsevier.com/retrieve/pii/S0264127523004264 (visited on 05/09/2025).

[7] V. L. J. Junior, H. Basoalto, and M. Papaelias, "A damage mechanics approach for lifetime estimation of wind turbine gearbox materials," *International Journal of Fatigue*, vol. 137, p. 105 671, 2020.

[8] C. C. Koch and L. H. Smith, "Loss sources and magnitudes in axial-flow compressors," *Journal of Engineering for Power*, vol. 98, pp. 411–424, 3 Jul. 1976, ISSN: 0022-0825. DOI: 10.1115/1.3446202. [Online]. Available: https://dx.doi.org/10.1115/1.3446202.

[9] R. Ehrmann, B. Wilcox, E. White, and D. Maniaci, "Effect of Surface Roughness on Wind Turbine Performance," en, Tech. Rep. SAND–2017-10669, 1596202, 657342, Oct. 2017, SAND–2017–10 669, 1596202, 657342. DOI: 10.2172/1596202. [Online]. Available: https://www.osti.gov/servlets/purl/1596202/ (visited on 05/26/2025).

[10] A. K. Ravishankara and H. Özdemir, "E□ect of leading edge erosion on wind turbine aerodynamics," en,

[11] A. Shankar Verma, Z. Jiang, Z. Ren, *et al.*, "A probabilistic long□term framework for site□specific erosion analysis of wind turbine blades: A case study of 31 Dutch sites," en, *Wind Energy*, vol. 24, no. 11, pp. 1315–1336, Nov. 2021, ISSN: 1095-4244, 1099-1824. DOI: 10.1002/we.2634. [Online]. Available: https://onlinelibrary.wiley.com/doi/10.1002/we.2634 (visited on 05/09/2025).

[12] N. Dalili, A. Edrisy, and R. Carriveau, "A review of surface engineering issues critical to wind turbine performance," en, *Renewable and Sustainable Energy Reviews*, vol. 13, no. 2, pp. 428–438, Feb. 2009, ISSN: 13640321. DOI: 10.1016/j.rser.2007.11.009. [Online]. Available: https://linkinghub.elsevier.com/retrieve/pii/S1364032107001554 (visited on 05/28/2025).

[13] N. Hoksbergen, “Predicting rain erosion damage in wind turbine blade coating materials,” en, ISBN: 9789036557269, PhD, University of Twente, Enschede, The Netherlands, Oct. 2023. DOI: 10.3990/1.9789036557269. [Online]. Available: https://purl.org/utwente/doi/10.3990/1.9789036557269 (visited on 05/09/2025).

[14] D. Eisenberg, S. Laustsen, and J. Stege, “Wind turbine blade coating leading edge rain erosion model: Development and validation,” *Wind Energy*, vol. 21, no. 10, pp. 942–951, 2018. DOI: https://doi.org/10.1002/we.2200. eprint: https://onlinelibrary.wiley.com/doi/pdf/10.1002/we.2200. [Online]. Available: https://onlinelibrary.wiley.com/doi/abs/10.1002/we.2200.

[15] C. Spruce, “Power performance of active stall wind turbines with blade contamination,” in *Proceedings of the European Wind Energy Conference*, 2006.

[16] H. Law and V. Koutsos, “Leading edge erosion of wind turbines: Effect of solid airborne particles and rain on operational wind farms,” *Wind Energy*, vol. 23, no. 10, pp. 1955–1965, 2020.

[17] G. P. Corten and H. F. Veldkamp, “Insects can halve wind-turbine power,” *Nature*, vol. 412, no. 6842, pp. 41–42, 2001.

[18] M. Elhadi Ibrahim and M. Medraj, “Water Droplet Erosion of Wind Turbine Blades: Mechanics, Testing, Modeling and Future Perspectives,” en, *Materials*, vol. 13, no. 1, p. 157, Dec. 2019, ISSN: 1996-1944. DOI: 10.3390/ma13010157. [Online]. Available: https://www.mdpi.com/1996-1944/13/1/157 (visited on 05/28/2025).

[19] N. Hoksbergen, R. Akkerman, and I. Baran, “The springer model for lifetime prediction of wind turbine blade leading edge protection systems: A review and sensitivity study,” *Materials*, vol. 15, no. 3, p. 1170, 2022.

[20] H. Slot, E. Gelinck, C. Rentrop, and E. Van Der Heide, “Leading edge erosion of coated wind turbine blades: Review of coating life models,” *Renewable energy*, vol. 80, pp. 837–848, 2015.

[21] T. Adams, C. Grant, and H. Watson, “A simple algorithm to relate measured surface roughness to equivalent sand-grain roughness,” *Avestia Publishing International Journal of Mechanical Engineering and Mechatronics*, vol. 1, 1 2012. DOI: 10.11159/ijmem.2012.008.

[22] J. D. Anderson, *Fundamentals of Aerodynamics*, 6th ed. McGraw-Hill Education, 2016.

[23] J. B. Barlow, W. H. Rae, and A. Pope, *Low-speed wind tunnel testing*. Wiley, 1999, p. 713, ISBN: 0471557749.

[24] R. Antonia, S. Rajagopalan, C. Subramanian, and A. Chambers, “Reynolds-number dependence of the structure of a turbulent boundary layer,” *Journal of Fluid Mechanics*, vol. 121, pp. 123–140, 1982.

[25] A. M. O. SMITH and D. W. CLUTTER, “The smallest height of roughness capable of affecting boundary-layer transition,” *Journal of the Aerospace Sciences*, vol. 26, pp. 229–245, 4 Apr. 1959. DOI: 10.2514/8.8019.

[26] J. Nikuradse, “Laws of flow in rough pipes,” National Advisory Committee for Aeronautics, Washington, DC, Tech. Rep., 1950.

[27] L. F. Moody, “Friction factors for pipe flow,” *Transactions of the ASME*, vol. 66, no. 8, pp. 671–684, 1944.

[28] T. Brooks, M. Marcolini, and D. Pope, “Airfoil trailing edge flow measurements and comparison with theory, incorporating open wind tunnel corrections,” in *9th aeroacoustics conference*, 1984, p. 2266.

[29] L. Prandtl, “Über flüssigkeitsbewegung bei sehr kleiner reibung,” in *Verhandlungen des dritten Internationalen Mathematiker-Kongresses in Heidelberg*, English title: On the Motion of Fluids with Very Little Viscosity, 1904, pp. 484–491.

[30] J. D. Anderson, “Ludwig prandtl’s boundary layer,” *Physics today*, vol. 58, no. 12, pp. 42–48, 2005.

[31] H. Schlichting and K. Gersten, *Boundary-Layer Theory*. Springer Berlin Heidelberg, Oct. 2016, pp. 1–799, ISBN: 9783662529195. DOI: 10.1007/978-3-662-52919-5.

[32] M. Drela, “Assorted views on teaching of aerodynamics,” in *16th AIAA Applied Aerodynamics Conference*, Albuquerque, NM, USA, Jun. 1998. DOI: 10.2514/6.1998-2792. [Online]. Available: https://arc.aiaa.org/doi/abs/10.2514/6.1998-2792.

[33] F. R. Hama, “An efficient tripping device,” *Journal of the Aeronautical Sciences*, vol. 24, no. 3, pp. 236–237, 1957.

[34] A. M. O. Smith and D. W. Clutter, “The Smallest Height of Roughness Capable of Affecting Boundary-Layer Transition,” en, *Journal of the Aerospace Sciences*, vol. 26, no. 4, pp. 229–245, Apr. 1959, ISSN: 1936-9999. DOI: 10.2514/8.8019. [Online]. Available: https://arc.aiaa.org/doi/10.2514/8.8019 (visited on 05/09/2025).

[35] M. Sanders and L. de Santana, “Beamut user guide - version 1.0,” University of Twente, Department of Thermal and Fluid Engineering, Engineering Fluid Dynamics Research Group, Technical Report, Apr. 2019, Beamforming implementation and benchmark application.

[36] N. Curle, “The influence of solid boundaries upon aerodynamic sound,” *Proceedings of the Royal Society of London. Series A. Mathematical and Physical Sciences*, vol. 231, no. 1187, pp. 505–514, 1955.

[37] J. Wolfe, J. Smith, and A. Index, “A review of airfoil trailing edge noise and its prediction,” *Acoustics Australia*, vol. 36, no. 1, 2008.

[38] L. de Santana, “Fundamentals of acoustic beamforming,” *NATO Educational Notes EN-AVT-287*, vol. 4, 2017.

[39] P. D. Welch, “The use of fast fourier transform for the estimation of power spectra: A method based on time averaging over short, modified periodograms,” Naval Underwater Systems Center, Technical Report, 1967.

[40] T. F. Brooks and W. M. Humphreys, “A deconvolution approach for the mapping of acoustic sources (damas) determined from phased microphone arrays,” *Journal of sound and vibration*, vol. 294, no. 4-5, pp. 856–879, 2006.

[41] J. F. Manwell, J. G. McGowan, and A. L. Rogers, *Wind Energy Explained: Theory, Design and Application*, 2nd. John Wiley & Sons, 2009, ISBN: 9780470015001.

[42] J. Biesheuvel, “Sound propagation corrections in open jet wind tunnels,” English, PhD Thesis - Research UT, graduation UT, University of Twente, Netherlands, Oct. 2022, ISBN: 978-90-365-5454-1. DOI: 10.3990/1.9789036554541.

[43] B. S. Henderson, “Sound generation by flow over a cavity,” in *Fourth Computational Aeroacoustics (CAA) Workshop on Benchmark Problems*, Document ID 20040182307; acquired September 1, 2004, NASA Glenn Research Center; Ohio Aerospace Institute, Brook Park, OH, USA, Oct. 2004. [Online]. Available: https://ntrs.nasa.gov/api/citations/20040182307/downloads/20040182307.pdf.

[44] J. E. Rossiter, “Wind-tunnel experiments on the flow over rectangular cavities at subsonic and transonic speeds,” Aeronautical Research Council, Reports and Memoranda, United Kingdom, Tech. Rep. 3438, 1964, Available at Cranfield University AERADE Repository.

[45] N. Gaudern, “A practical study of the aerodynamic impact of wind turbine blade leading edge erosion,” in *Journal of Physics: Conference Series*, IOP Publishing, vol. 524, 2014, p. 012 031.

[46] A. Sareen, C. A. Sapre, and M. S. Selig, “Effects of leading edge erosion on wind turbine blade performance,” *Wind energy*, vol. 17, no. 10, pp. 1531–1542, 2014.

[47] I. F. Zidane, K. M. Saqr, G. Swadener, X. Ma, and M. F. Shehadeh, “On the role of surface roughness in the aerodynamic performance and energy conversion of horizontal wind turbine blades: A review: Effects of blade surface roughness on wind turbine performance,” en, *International Journal of Energy Research*, vol. 40, no. 15, pp. 2054–2077, Dec. 2016, ISSN: 0363907X. DOI: 10.1002/er.3580. [Online]. Available: https://onlinelibrary.wiley.com/doi/10.1002/er.3580 (visited on 05/09/2025).

[48] S. S. Perez-Moreno, K. Dykes, K. O. Merz, and M. B. Zaaijer, “Multidisciplinary design analysis and optimisation of a reference offshore wind plant,” *Journal of Physics: Conference Series*, vol. 1037,

no. 4, p. 042 004, Jun. 2018. DOI: 10.1088/1742-6596/1037/4/042004. [Online]. Available: https://dx.doi.org/10.1088/1742-6596/1037/4/042004.

[49] J. Jonkman, "Definition of a 5-mw reference wind turbine for offshore system development," *National Renewable Energy Lab*, 2009.

[50] I. Romero-Sanz and A. Matesanz, "Noise management on modern wind turbines," *Wind Engineering*, vol. 32, pp. 27–44, 2008.

[51] R. Gutiérrez, E. Llórente, F. Echeverría, and D. Ragni, "Wind tunnel tests for vortex generators mitigating leading-edge roughness on a 30% thick airfoil," en, *Journal of Physics: Conference Series*, vol. 1618, no. 5, p. 052 058, Sep. 2020, ISSN: 1742-6588, 1742-6596. DOI: 10.1088/1742-6596/1618/5/052058. [Online]. Available: https://iopscience.iop.org/article/10.1088/1742-6596/1618/5/052058 (visited on 05/09/2025).

[52] J. I. Bech, N. F.-J. Johansen, M. B. Madsen, Á. Hannesdóttir, and C. B. Hasager, "Experimental study on the effect of drop size in rain erosion test and on lifetime prediction of wind turbine blades," *Renewable Energy*, vol. 197, pp. 776–789, 2022.

[53] Y. A. de Valk, *A novel construction of wind tunnel models for wind energy applications*, Bachelor's thesis, University of Twente, Dec. 2019. [Online]. Available: http://essay.utwente.nl/81061/.

[54] L. D. de Santana, M. P. Sanders, C. H. Venner, and H. W. Hoeijmakers, "The utwente aeroacoustic wind tunnel upgrade," in *2018 AIAA/CEAS Aeroacoustics Conference*, 2018, p. 3136.

[55] D. Weihs, "On the polynomial approximation of boundary-layer flow profiles," *Applied Scientific Research*, vol. 31, pp. 253–266, 1975.

[56] J. Majdalani and L.-J. Xuan, "On the kármán momentum-integral approach and the pohlhausen paradox," *Physics of Fluids*, vol. 32, no. 12, 2020.

[57] CAE Software & Systems, *Noise Inspector Manual V2.0*, Version 2.0, CAE Software & Systems GmbH, Linteler Straße 23, 33334 Gütersloh, Germany, 2025. [Online]. Available: http://www.cae-systems.de.

[58] E. Sarradj, G. Herold, P. Sijtsma, *et al.*, "A microphone array method benchmarking exercise using synthesized input data," in *23rd AIAA/CEAS Aeroacoustics Conference*, AIAA Aviation Forum, Denver, CO, USA, 2017.

[59] T. F. Brooks, D. S. Pope, and M. A. Marcolini, "Airfoil self-noise and prediction," NASA Langley Research Center, Hampton, VA, Tech. Rep. NASA RP-1218, 1989. [Online]. Available: https://ntrs.nasa.gov/api/citations/19890016302/downloads/19890016302.pdf.

Part V

Appendices

A

Balance laws

This appendix shows the balance laws for the flow over the turbine blade.

A.1. Assumptions

By taking assumptions, the balance laws will be made for a model of the flow over a wind turbine blade. The model that will be looked at is the flow over a section of the wind turbine blade and the flow within the boundary layer.

- Steady state $\frac{\partial}{\partial t} = 0$
- Incompressible $\rho = const.$
- Two dimensional $\frac{\partial}{\partial z} = 0$
- Newtonian fluid

A.2. Mathematical definitions

Material Derivative

$$\frac{D\gamma}{Dt} = \frac{\partial \gamma}{\partial t} + \vec{u} \cdot \nabla \gamma \quad = \quad \frac{\partial \gamma}{\partial t} + (\vec{u} \cdot \vec{\nabla} \gamma) \quad = \quad \frac{\partial \gamma}{\partial t} + \sum_k u_k \frac{\partial \gamma}{\partial x_k} \tag{A.1}$$

Reynolds Transport Theorem

$$\frac{D}{Dt} \int_V \gamma \, dV = \frac{\partial}{\partial t} \int_V \gamma \, dV + \int_S \gamma u_n \, dS = \frac{\partial}{\partial t} \int_V \gamma \, dV + \int_S \rho V u_n \, dS \tag{A.2}$$

Gauss / Divergence theorem

$$\int_S \gamma \cdot \vec{n} \, dS = \int_V \vec{\nabla} \gamma \, dV \tag{A.3}$$

Dirac Delta

$$for \ (i = j) \quad \delta_{ij} = 1 \qquad\qquad for \ (i \neq j) \quad \delta_{ij} = 0 \tag{A.4}$$

A.3. Governing equations

In this section we will look at the governing equations of the problem so we can better identify the properties we would like to measure, what variables should be kept constant and what variabels we would like to change.

A.3.1. Mass Balance

$$\dot{m} = \frac{d}{dt} \int \rho \, dV = 0 \tag{A.5}$$

Using the Reynolds transport theorem we get:

$$\dot{m} = \int_{V_c(t)} \frac{\partial \rho(\vec{x}, t)}{\partial t} dV + \int_{S(t)} \rho \vec{u} \cdot \vec{n} \, dS = 0 \tag{A.6}$$

Using the Divergence Theorem results in:

$$\dot{m} = \int_{V_c(t)} \frac{\partial \rho(\vec{x}, t)}{\partial t} \, dV + \int_{V_c(t)} \nabla \cdot (\rho \vec{u}) dV \tag{A.7}$$

Because the flow is assumed to be steady and incompressible, the mass balance simplifies to:

$$\dot{m} = \rho \int_{V_c(t)} \nabla \cdot \vec{u} dV = 0 \tag{A.8}$$

Because this is valid for any control volume, the integral has to be zero everywhere

$$\dot{m} = \rho \left(\frac{du}{dx} + \frac{dv}{dy} \right) = 0 \tag{A.9}$$

Because the density can not be zero the terms witin the bracket must be thus:

$$\boxed{\left(\frac{du}{dx} + \frac{dv}{dy} \right) = 0} \tag{A.10}$$

Or in index notation:

$$\frac{\partial u_i}{\partial x_i} = 0 \tag{A.11}$$

A.3.2. Momentum Balance

From Newton's second law we get

$$\vec{F} = m\vec{a} = \sum_i \vec{F}_{\text{ext}} = \sum_i \left(\vec{F}_{\text{surface}} + \vec{F}_{\text{body}}\right) \tag{A.12}$$

For a fluid it can be written to:

$$\frac{d}{dt}\int_{V_c(t)} \rho\vec{u} = \int_{S(t)} \underline{\underline{\sigma}} \cdot \vec{n}\, ds + \int_{V_c(t)} \rho\vec{g}\, dV \tag{A.13}$$

The first term can be expanded into:

$$\frac{d}{dt}\int_{V_c(t)} \rho\vec{u}\, dV = \int_{V_c(t)} \rho\frac{\partial\vec{u}}{\partial t}\, dV + \int_{S_c(t)} \rho\vec{u}(\vec{u}\cdot\vec{n})\, dS = \int_{V_c(t)} \frac{\partial}{\partial t}(\rho\vec{u}) + \nabla\cdot(\rho\vec{u}\vec{u})\, dV \tag{A.14}$$

$$\frac{d}{dt}\int_{V_c(t)} \rho u_i = \int_{V_c(t)} \frac{\partial}{\partial t}(\rho u_i) + \frac{\partial}{\partial x_j}(\rho u_i u_j)\, dV \tag{A.15}$$

The surface force term can be expanded into:

$$\int_{S_c(t)} \underline{\underline{\sigma}} \cdot \vec{n}\, dS = \int_{V_c(t)} \nabla\cdot\underline{\underline{\sigma}}\, dV = \int_{V_c(t)} \frac{\partial}{\partial x_j}(\sigma_{ij})\, dV \tag{A.16}$$

Reducing this term using the mass balance equation we get

$$\sigma_{ij} = -p\delta_{ij} + \tau_{ij} = -p\delta_{ij} + \mu\left(\frac{\partial u_i}{\partial x_j} + \frac{\partial u_j}{\partial x_i}\right) \tag{A.17}$$

Now that we have everything in a volume integral we gan write the momentum equation as:

$$\int_{V_{c(t)}} \frac{\partial}{\partial t}(\rho u_i) + \frac{\partial}{\partial x_j}(\rho u_i u_j)\, dV = \int_{V_{c(t)}} \left(\frac{\partial}{\partial x_j}\left(-p\delta_{ij} + \mu\left(\frac{\partial}{\partial x_j} + \frac{\partial u_j}{\partial x_i}\right)\right) + \rho g_i\right) dV \tag{A.18}$$

Setting the first time dependent term to zero as the problem is steady state and taking out of the integral we get the differential form

$$\frac{\partial}{\partial x_j}(\rho u_i u_j) = \frac{\partial}{\partial x_j}(-p\delta_{ij}) + \mu\left(\frac{\partial^2 u_i}{\partial x_j^2} + \frac{\partial^2 u_j}{\partial x_i^2}\right) + \rho g_j \tag{A.19}$$

The first term can be rewritten to

$$\frac{\partial}{\partial x_k}(\rho u_i u_k) = \rho\left(\frac{\partial}{\partial x_k}(u_i u_k)\right) = \rho\left(\frac{du_i}{dx_k}u_k + \frac{\partial u_k}{\partial x_k}u_i\right) = \rho u_k\frac{\partial u_i}{\partial x_k} \tag{A.20}$$

The viscous term can be rewritten to

$$\frac{\partial^2 u_j}{\partial x_j \partial x_i} = \frac{\partial}{\partial x_i}(\nabla\cdot\vec{u}) = 0 \tag{A.21}$$

Now in differential form the momentum equation becomes:

$$\boxed{\rho\, u_j\frac{\partial u_i}{\partial x_j} = -\frac{\partial p}{\partial x_i} + \mu\,\frac{\partial^2 u_i}{\partial x_j^2} + \rho\, g_i.} \tag{A.22}$$

Momentum in X direction
Filling in the equation found for the momentum in x direction we get

$$0 = u\frac{\partial u}{\partial x} + v\frac{\partial u}{\partial y} + \frac{1}{\rho}\frac{\partial p}{\partial x} - \nu\left(\frac{\partial^2 u}{\partial x^2} + \frac{\partial^2 u}{\partial y^2}\right) \tag{A.23}$$

By non-dimentionalizing the equation, by writing the velocity and pressure components as a function of the mean value and a fluctuating component, for the values; $u = U + u'$, $v = V + v'$,$p = P + p'$,

$$0 = Uu'\frac{\partial u'}{\partial cx'}, Vv'\frac{\partial u'}{\partial \delta y'} + \frac{P}{\rho c}\frac{\partial p'}{\partial x'} - \frac{\mu}{\rho}\left(\frac{\partial^2 u'}{\partial c^2 x'^2} + \frac{\partial^2 u'}{\partial \delta'^2 y^2}\right) \tag{A.24}$$

Taking U^2/c out of the equation

$$0 = \frac{U^2}{c}\left(u'\frac{\partial u'}{\partial x'} + \frac{Vc}{U\delta}v'\frac{\partial u'}{\partial y'} + \frac{P}{\rho U^2}\frac{\partial p'}{\partial x'} - \frac{\mu}{\rho}\frac{c}{U^2}\left(\frac{U}{c^2}\frac{\partial^2 u'}{\partial x'^2} + \frac{U}{\delta^2}\frac{\partial^2 u'}{\partial y'^2}\right)\right) \tag{A.25}$$

Taking $\frac{1}{\delta^2}$ out of bracket we get:

$$0 = \frac{U^2}{c}\left(u'\frac{\partial u'}{\partial x'} + \frac{Vc}{U\delta}v'\frac{\partial u'}{\partial y'} + \frac{P}{\rho U^2}\frac{\partial p'}{\partial x'} - \frac{\mu}{\rho}\frac{c}{U}\frac{1}{\delta^2}\left(\frac{\delta^2}{c^2}\frac{\partial^2 u'}{\partial x'^2} + \frac{\partial^2 u'}{\partial y'^2}\right)\right) \tag{A.26}$$

Multiplying the viscous term by c^2/c^2

$$0 = \frac{U^2}{c}\left(u'\frac{\partial u'}{\partial x'} + \frac{Vc}{U\delta}v'\frac{\partial u'}{\partial y'} + \frac{P}{\rho U^2}\frac{\partial p'}{\partial x'} - \frac{\mu}{\rho}\frac{c}{U}\frac{c^2}{c^2}\frac{1}{\delta^2}\left(\frac{\delta^2}{c^2}\frac{\partial^2 u'}{\partial x'^2} + \frac{\partial^2 u'}{\partial y'^2}\right)\right) \tag{A.27}$$

$$0 = \frac{U^2}{c}\left(u'\frac{\partial u'}{\partial x'} + \frac{Vc}{U\delta}v'\frac{\partial u'}{\partial y'} + \frac{P}{\rho U^2}\frac{\partial p'}{\partial x'} - \frac{\mu}{\rho Uc}\left(\frac{c^2}{\delta^2}\right)\left(\frac{\delta^2}{c^2}\frac{\partial^2 u'}{\partial x'^2} + \frac{\partial^2 u'}{\partial y'^2}\right)\right) \tag{A.28}$$

From the mass balance

$$\frac{\partial u}{\partial x} + \frac{\partial v}{\partial y} = 0 \quad \rightarrow \quad 0 = \frac{U}{c} + \frac{V}{\delta} \quad \rightarrow \quad 1 = \frac{VC}{U\delta} \tag{A.29}$$

By taking the term out of the brackets and

$$0 = u'\frac{\partial u'}{\partial x'} + v\frac{\partial u'}{\partial y'} + \frac{P}{\rho u^2}\frac{\partial p'}{\partial x'} - Re_c^{-1}\left(\frac{c^2}{\delta^2}\right)\left(\frac{\delta^2}{c^2}\frac{\partial^2 u'}{\partial x'^2} + \frac{\partial^2 u'}{\partial y'^2}\right) \tag{A.30}$$

For the order of magnitude of the terms in this problem to make sense

$$\mathcal{O}(1) = \left(\frac{P}{\rho U^2}\right) \quad \Rightarrow \quad P = \rho U^2 \tag{A.31}$$

Simplifying the equation to:

$$0 = u'\frac{\partial u'}{\partial x'} + v\frac{\partial u'}{\partial y'} + \frac{\partial p'}{\partial x'} - Re_c^{-1}\left(\frac{c^2}{\delta^2}\right)\left(\frac{\delta^2}{c^2}\frac{\partial^2 u'}{\partial x'^2} + \frac{\partial^2 u'}{\partial y'^2}\right) \tag{A.32}$$

The order of the term $Re_c^{-1}\left(\frac{c^2}{\delta^2}\right) = \mathcal{O}(1)$,similar to the pressure term this means that the order size of the length ratios should corrosond to theat of the chord based Reynold's number

$$\mathcal{O}\left(Re_c^{-1}\left(\frac{c}{\delta}\right)^2\right) = 1 \quad \rightarrow \quad Re_c^{-1}\left(\frac{c}{\delta}\right)^2 = 1 \quad \rightarrow \quad Re_c^{1/2}\frac{c}{\delta} \quad \rightarrow \quad \delta = c\,Re_c^{-1/2} \tag{A.33}$$

$$0 = u' \frac{\partial u'}{\partial x'} + v \frac{\partial u'}{\partial y'} + \frac{\partial p'}{\partial x'} - \left(Re_c^{-1} \frac{\partial^2 u'}{\partial x'^2} + \frac{\partial^2 u'}{\partial y'^2} \right) \tag{A.34}$$

Here we can see that when the Reynolds number is sufficiently large enough the term $\frac{\partial^2 u'}{\partial x'^2}$ becomes insignificant. Therefore by removing this term and going back to the dimentinal parameters we get the reduced momentum equation for a boundary layer:

$$u \frac{\partial u}{\partial x} + v \frac{\partial u}{\partial y} + \frac{1}{\rho} \frac{\partial p}{\partial x} = \frac{\mu}{\rho} \frac{\partial^2 u}{\partial y^2} \tag{A.35}$$

As discussed we want to see the impact of leading edge erosion on the boundary layer and the resulting turbulence. The hypothesis is that the surface roughness affects development of the boundary layer and therefore produce an aeroacoustic signal. Looking at the reduced equation we can see that the term μ which changes based on the leading edge errosion can have affect on the pressure in chord wise direction and the velocity profile in the boundary layer. When the assumption is made that the density ρ is constant and the problem is steady.

Momentum in Y direction
Filling in the equation found for the momentum in y direction we get

$$0 = u \frac{\partial v}{\partial x} + v \frac{\partial v}{\partial y} + \frac{1}{\beta} \frac{\partial p}{\partial y} - \frac{\mu}{\beta} \left(\frac{\partial^2 v}{\partial x^2} + \frac{\partial^2 v}{\partial y^2} \right) \tag{A.36}$$

Non-dimentionalizing the equation:

$$0 = U u' \frac{\partial v' V}{\partial c x'} + V v' \frac{\partial v' V}{\partial \delta y'} + \frac{P}{\rho} \frac{\partial p'}{\partial \delta y'} - \frac{\mu}{\rho} \left(\frac{\partial^2 v' V}{\partial c^2 x'^2} + \frac{d^2 v' V}{d \delta^2 y'^2} \right) \tag{A.37}$$

$$0 = U u' \frac{\partial v' V}{\partial c x'} + V v' \frac{\partial v' V}{\partial \delta y'} + \frac{P}{\rho} \frac{\partial p'}{\partial \delta y'} - \frac{\mu}{\rho} V \left(\frac{1}{c^2} \frac{\partial^2 v'}{\partial x'^2} + \frac{1}{\delta^2} \frac{\partial^2 v'}{\partial y'^2} \right) \tag{A.38}$$

$$0 = \frac{V^2}{\delta} \left(\frac{U \delta}{V c} u' \frac{\partial v'}{\partial x'} + v' \frac{\partial v'}{\partial y'} + \frac{P}{\rho V^2} \frac{\partial p'}{\partial y'} + \frac{\mu \delta}{\rho V c} \frac{1}{\delta^2} \left(\frac{\delta^2}{c^2} \frac{\partial^2 v'}{\partial x'^2} \cdot \frac{\partial^2 v'}{\partial y'^2} \right) \right) \tag{A.39}$$

$$\frac{P}{\rho V^2} = \frac{P}{\rho U^2} \frac{c^2}{\delta^2} \tag{A.40}$$

$$\frac{\mu \delta}{\rho V} \cdot \frac{1}{\delta^2} = \frac{\mu}{\rho \delta} = \frac{\mu c}{\rho U \delta^2} = \frac{\mu c}{\rho U \delta^2} \cdot \frac{c^2}{c^2} = \frac{\mu c}{\rho U \delta c} \cdot \frac{c}{\delta} = \frac{\mu}{\rho U c} \cdot \frac{c^2}{\delta^2} = Re_c \cdot \left(\frac{C}{\delta} \right)^2 \tag{A.41}$$

$$0 = \frac{V^2}{\delta} \left(u' \frac{\partial v'}{\partial x'} + v' \frac{\partial v'}{\partial y'} - \frac{P}{\rho U^2} \frac{c^2}{\delta^2} \frac{\partial p'}{\partial y'} + \frac{\mu}{\rho U c} \frac{c^2}{\delta^2} \left(\frac{\delta^2}{c^2} \frac{\partial^2 v'}{\partial x'^2} + \frac{\partial^2 v'}{\partial y'^2} \right) \right) \tag{A.42}$$

$$0 = u' \frac{\partial v'}{\partial x'} + v' \frac{\partial v'}{\partial y'} + \frac{P}{\rho U^2} \frac{c^2}{\delta^2} \frac{\partial p'}{\partial y'} - \frac{\mu}{\rho U c} \left(\frac{\partial^2 v'}{\partial x'^2} + \frac{c^2}{\delta^2} \frac{\partial^2 v'}{\partial y'^2} \right) \tag{A.43}$$

$$0 = u' \frac{\partial v'}{\partial x'} + v' \frac{\partial v'}{\partial y'} + \mathsf{Re}_c \frac{\partial p'}{\partial y'} - \mathsf{Re}_c^{-1} \left(\frac{\partial^2 v'}{\partial x'^2} + \mathsf{Re}_c \frac{\partial^2 v'}{\partial y'^2} \right) \tag{A.44}$$

$$0 = \mathsf{Re}_c^{-1} \left(u' \frac{\partial v'}{\partial x'} + v' \frac{\partial v'}{\partial y'} \right) + \frac{\partial p'}{\partial y'} - \mathsf{Re}_c^{-1} \left(\mathsf{Re}_c^{-1} \frac{\partial^2 v'}{\partial x'^2} + \frac{\partial^2 v'}{\partial y'^2} \right) \tag{A.45}$$

Therefore if the Reynolds number is sufficiently large enough all terms except the pressure term become insignificant resulting in the following:

$$\boxed{0 = \frac{\partial p}{\partial y}} \tag{A.46}$$

This shows that there is no pressure gradient in the y direction of the boundary layer

The boundary layer equations
Boundary layer mass balance

$$\boxed{\left(\frac{\partial u}{\partial x} + \frac{\partial v}{\partial y}\right) = 0} \tag{A.47}$$

Boundary layer momentum balance X direction

$$\boxed{u\frac{\partial u}{\partial x} + v\frac{\partial u}{\partial y} + \frac{1}{\rho}\frac{\partial p}{\partial x} = \frac{\mu}{\rho}\frac{\partial^2 u}{\partial y^2}} \tag{A.48}$$

Boundary layer momentum balance Y direction

$$\boxed{0 = \frac{\partial p}{\partial y}} \tag{A.49}$$

B

Conventional frequency domain beamforming

Conventional frequency domain beamforming using a microphone array is a commonly used method to identify acoustic sources. The idea behind this method is relatively simple, difference between microphone signals in phase or in time due to the physical separation between the microphones can be used to find the location where the sound is coming from. This is done through constructive or destructive interference. The method works in a few steps:

1. Transformation to the frequency domain

Each microphone records a pressure signal in the time domain $p(t)$, which is transformed to the frequency domain using a Fourier transform. This allows for analysis of both amplitude and phase content at each frequency:

$$\tilde{p} = \int_{-\infty}^{\infty} p(t)\, e^{i\omega t}\, dt \tag{B.1}$$

This step is typically calculated using the Fast Fourier Transform (FFT), providing the complex frequency-domain signal for each microphone.

2. Steering vector

For each search grid point $\vec{\xi}_j$, the phase shift a is applied to each microphone signal to account for the time delay. The relative time delay $\tau_{j,n}$ between the n^{th} microphone and the reference microphone $n = 0$ is given by:

$$\tau_{j,n} = \frac{r_{j,n} - r_{j,0}}{a} \tag{B.2}$$

Where $r_{j,n} = \left|\vec{x}_n - \vec{\xi}_j\right|$ denotes the distance between microphone n and search location j, and a is the speed of sound. The corresponding frequency-domain steering vector is shown in equation B.3

$$g_{j,n}(\omega_k) = e^{i2\pi f \tau_{j,n}} \tag{B.3}$$

This vector aligns the phases of the microphone signals assuming a source at $\vec{\xi}_j$.

3. Beamforming algorithm

Beamformer signal $Z_j(\omega)$ for a given search location j and frequency ω is calculated as shown in Equation B.4.

$$Z_j(\omega) = \frac{1}{N} \sum_{n=1}^{N} \frac{r_{j,0}}{r_{j,n}}\, \tilde{p}_n\, e^{-i\omega\tau_{j,n}} \tag{B.4}$$

This formulation includes a spherical spreading correction via the ratio $r_{j,0}/r_{j,n}$, accounting for distance-related attenuation. Using the Hermite transpose (†) of the steering vector (transposed complex conjugate), the equation can be written as:

$$Z_j(\omega_k) = g^\dagger_{j,n}(\omega_k)\, \tilde{p}_n(\omega_k) \tag{B.5}$$

Or written in the form per frequency bin k:

$$Z_{j,k} = g^\dagger_{j,n,k}\, \tilde{p}_{n,k} \tag{B.6}$$

4. Output power estimation

The acoustic power at position j and frequency bin k is calculated using $|Z_{j,k}|^2$. This can be rewritten into:

$$\begin{aligned} P_{j,k} &= |Z_{j,k}|^2 \\ &= Z_{j,k} Z^*_{j,k} \\ &= \left(g^\dagger_{j,n,k}\, \tilde{p}_{n,k}\right) \left(g^\dagger_{j,n,k}\, \tilde{p}_{n,k}\right)^* \\ &= g^\dagger_{j,n,k} \left(\tilde{p}_{n,k}\, \tilde{p}^\dagger_{n,k}\right) g_{j,n,k} \end{aligned} \tag{B.7}$$

The term $\tilde{p}_{n,k}\, \tilde{p}^\dagger_{n,k}$ is the cross-spectral matrix (CSM), which captures the correlation of the microphone signals and shown in Equation B.8.

$$\text{CSM} = \tilde{p}_{n,k}\, \tilde{p}^\dagger_{n,k} \tag{B.8}$$

5. Source strength estimation

Finally, the strength A of a source at each search grid point can be calculated using the CSM and the steering vectors as shown in Equation B.9

$$A = \frac{\boldsymbol{g}^* \,\text{CSM}\, \boldsymbol{g}}{\left(\boldsymbol{g}^\dagger \boldsymbol{g}\right)^2} \tag{B.9}$$

This formulation offers a quantitative measure of source intensity and is often used for source ranking or thresholding in acoustic imaging.

C

Construction erosion model

C.1. Layer material

For the construction of the damage model self-adhesive plastic foils were used. The thickness of the foil used including the adhesive layer is $0.2\ mm$ and is made of PVC plastic.

C.2. Modeling of pit and gouge erosion features

To apply the erosion characteristics to the foil, the position of the defect locations as shown in figures C.2, C.3, and C.4, a caliper was used to measure the locations of the defects.

The pits and gouges are modeled as cylinders, the calculated diameter of the pits and gouges was 1.9 and 4.9 respectively. Using a lathe, punches were created, this was done by taking a rod and drilling a hole at the end, the tip of the punch was tapered, and a late and a grind stone was used to sharpen the tip. Because the size of the drill bits available where limited, the diameter of the holes created was 2 and 5 mm for the pit and gouge respectively.

Using the marked location on the defects and a punch and hammer was used to apply the defect to the adhesive foil. For the PG damage model, where both pits and gouges are present, the distribution and locations are combined to build the model.

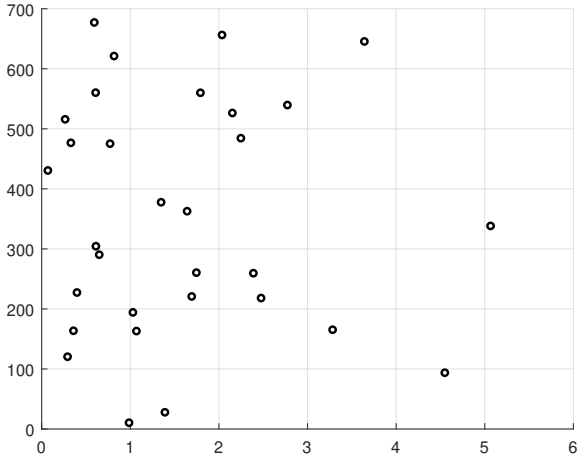

(a) Locations pits upper foil for erosion model P

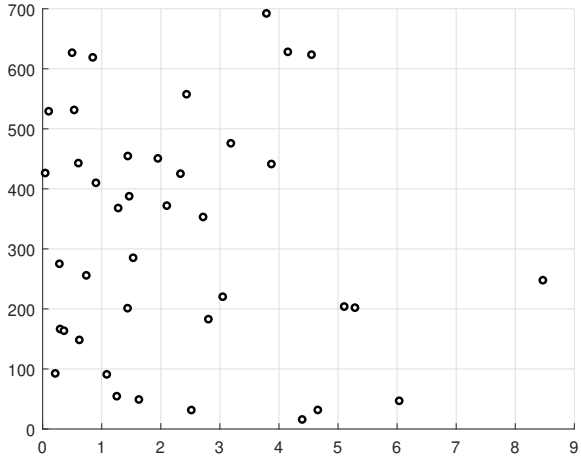

(b) Locations pits upper foil for erosion stage P

Figure C.2: Locations pits for erosion model P

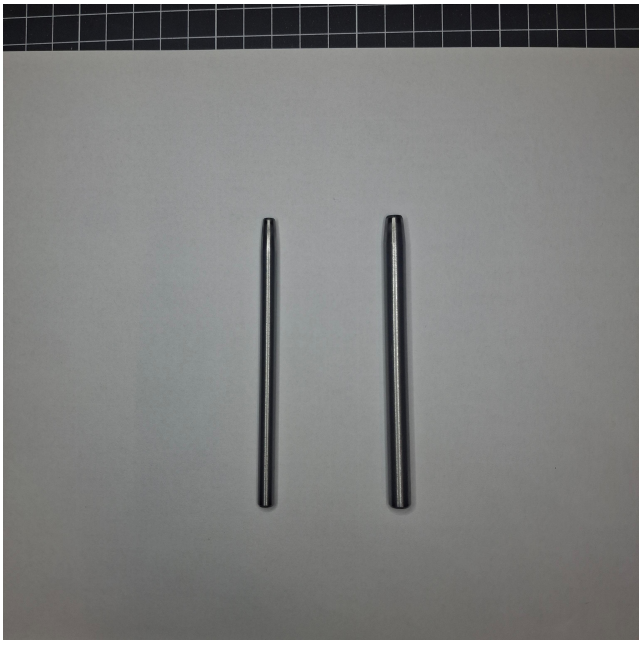

Figure C.1: Punches for the modeling of pits and gouges

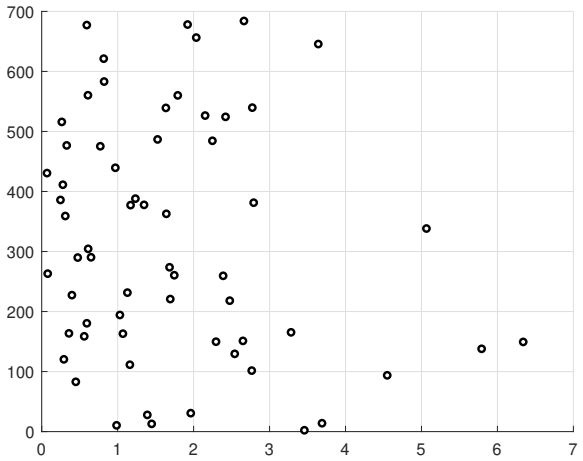

(a) Locations pits upper foil for erosion stage PG

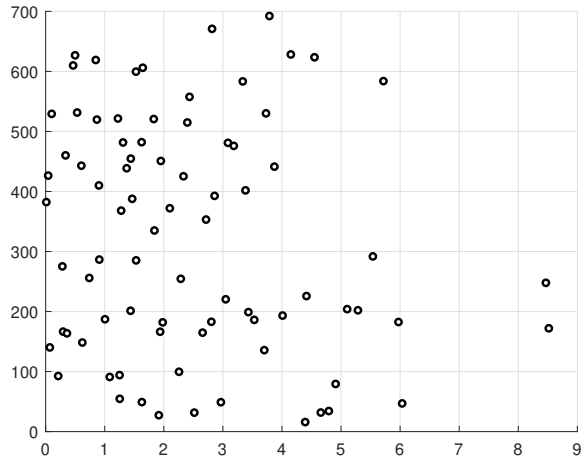

(b) Locations pits upper foil for erosion model PG

Figure C.3: Locations pits for erosion model PG

The Figure C.4, the position of the gouges are depicted.

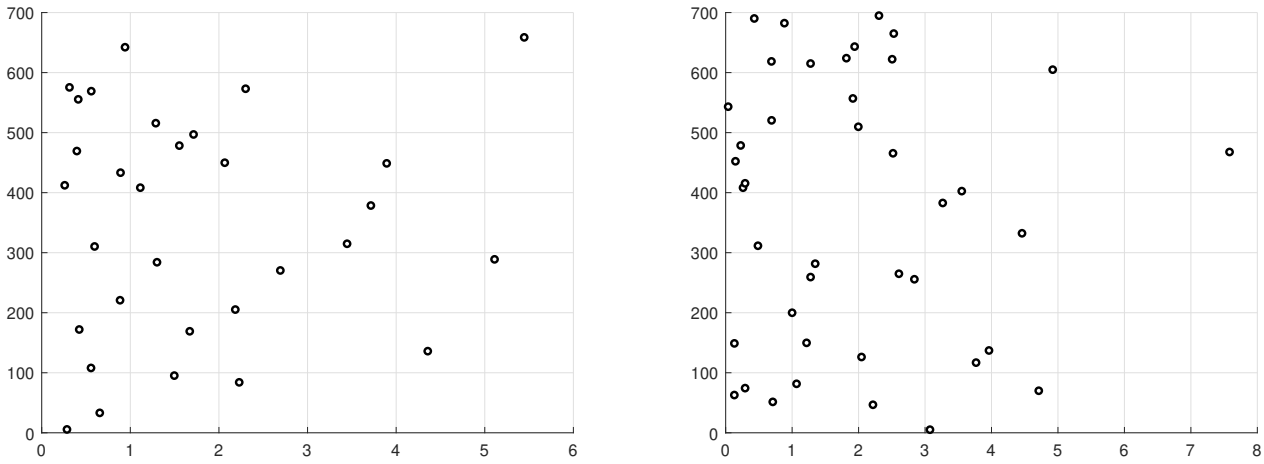

(a) Locations gouges upper foil

(b) Locations gouges upper foil

Figure C.4: Locations gouges for erosion model PG

C.3. Modeling of delamination erosion features

For the construction of the delamination features, as shown in the section 4.3.6, a straight bar was used as a guide to cut the adhesive foil. Using a caliper to measure the adhesive foil to the correct width, the bar was clamped down on the table and the cut was made with a knife to cut the strips.

(a) Straight bar used for clamping

(b) Positioning straight bar

Figure C.5: Construction setup cutting bar

D

XFOIL comparison

D.1. Pressure distribution and shape factor over the chord DU97-W-300 airfoil at $Re_c = 6 \times 10^5$, $\alpha_t = 14°$

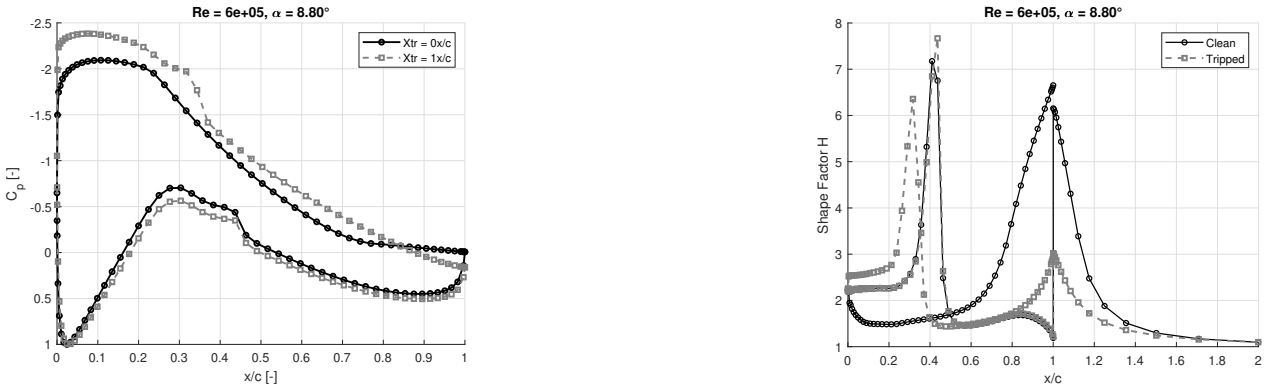

(a) Pressure distribution over chord

(b) Shape factor H over chord

Figure D.1: XFOIL clean and tripped flow over DU97-W-300 airfoil at $Re_c = 6 \times 10^5$, $\alpha_t = 14°$

D.2. Pressure distribution and shape factor over the chord DU97-W-300 airfoil at $Re_c = 7 \times 10^5$, $\alpha_t = 14°$

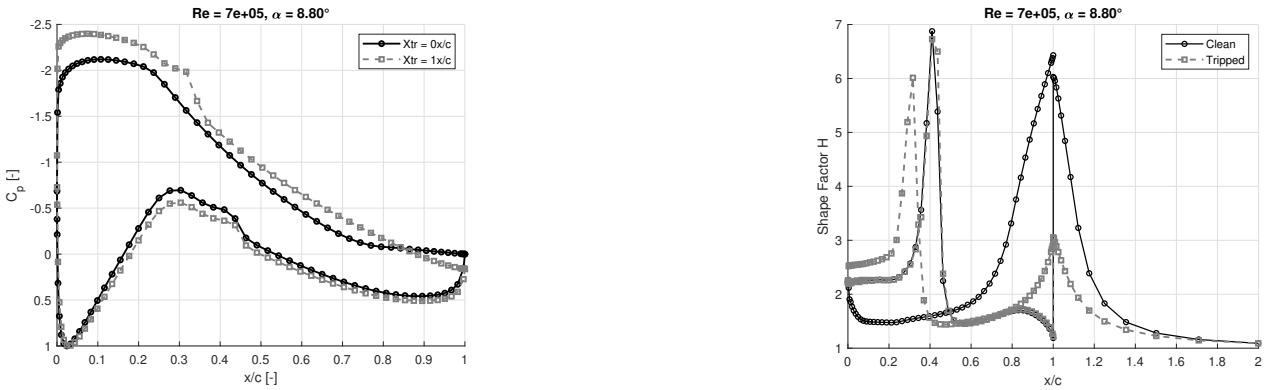

(a) Pressure distribution over chord

(b) Shape factor H over chord

Figure D.2: XFOIL untripped and tripped flow over DU97-W-300 airfoil at $Re_c = 6 \times 10^5$, $\alpha_t = 14°$

D.3. Pressure distribution and shape factor over the chord DU97-W-300 airfoil at $Re_c = 8 \times 10^5$, $\alpha_t = 14°$

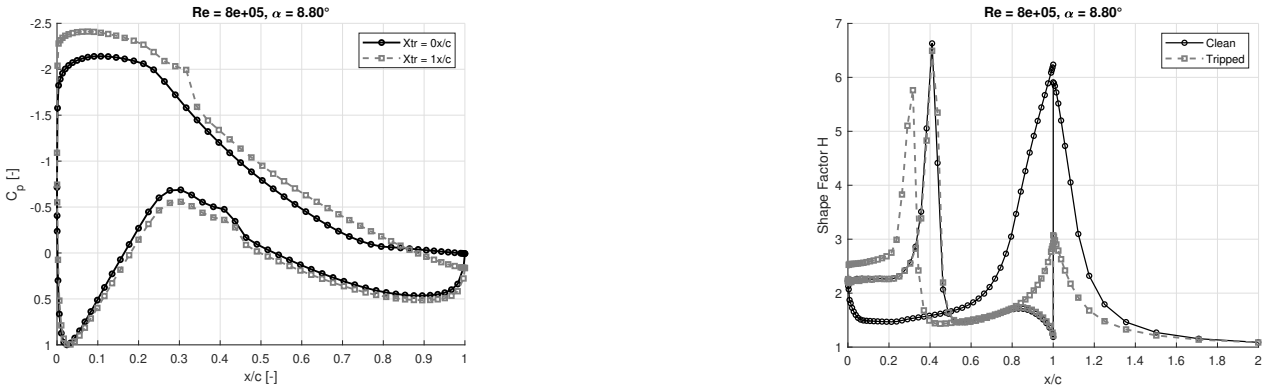

(a) Pressure distribution over chord

(b) Shape factor H over chord

Figure D.3: XFOIL clean and tripped flow over DU97-W-300 airfoil at $Re_c = 6 \times 10^5$, $\alpha_t = 14°$

E

Beamforming results

E.1. Beamforming results – Clean airfoil

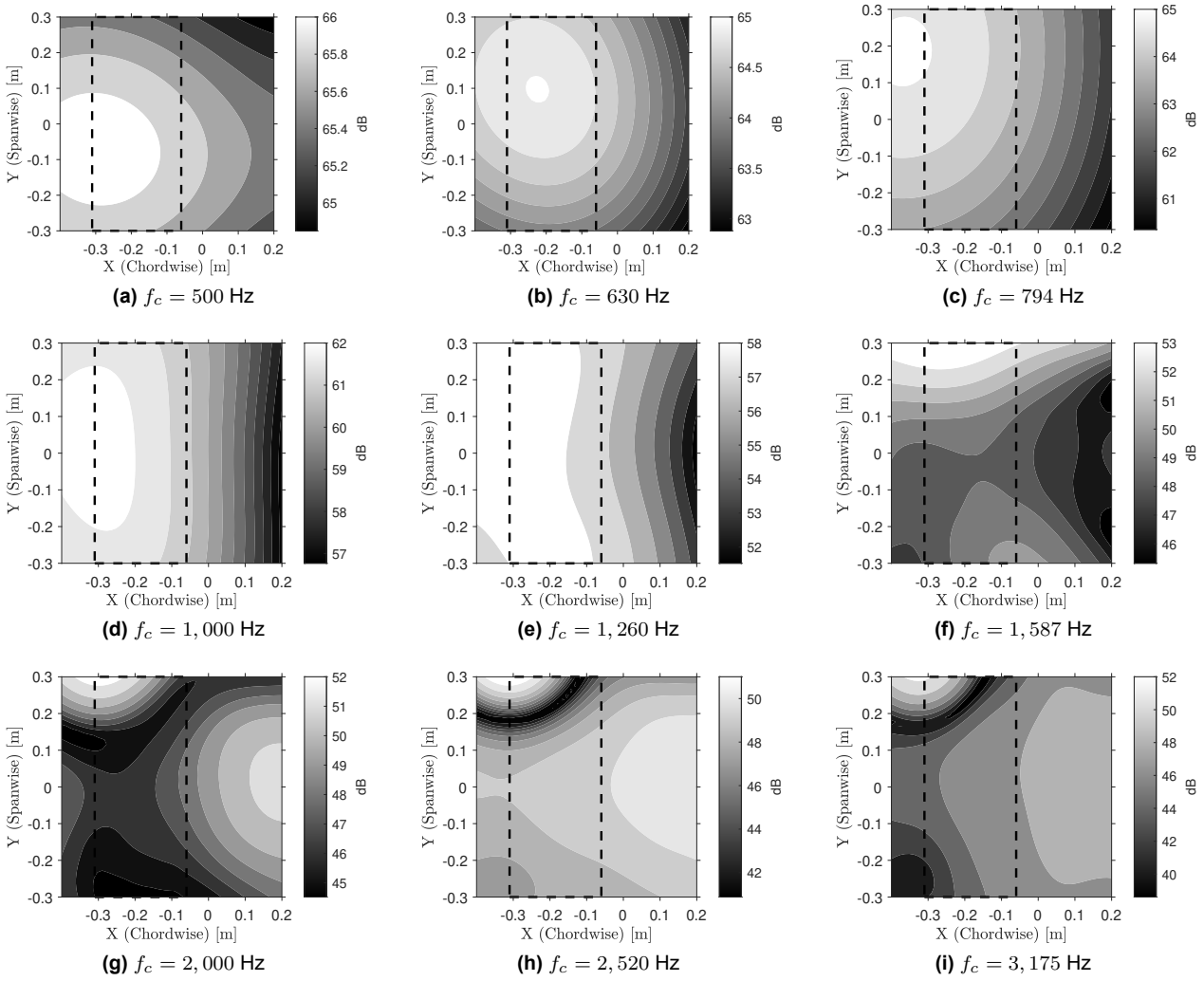

(a) $f_c = 500$ Hz **(b)** $f_c = 630$ Hz **(c)** $f_c = 794$ Hz

(d) $f_c = 1,000$ Hz **(e)** $f_c = 1,260$ Hz **(f)** $f_c = 1,587$ Hz

(g) $f_c = 2,000$ Hz **(h)** $f_c = 2,520$ Hz **(i)** $f_c = 3,175$ Hz

Figure E.1: Beamforming results for Clean airfoil test for the frequency bins $f_c = 500$ Hz $- 3,175$ Hz, $\alpha_t = 14°$, and $Re_c \approx 8 \times 10^5$.

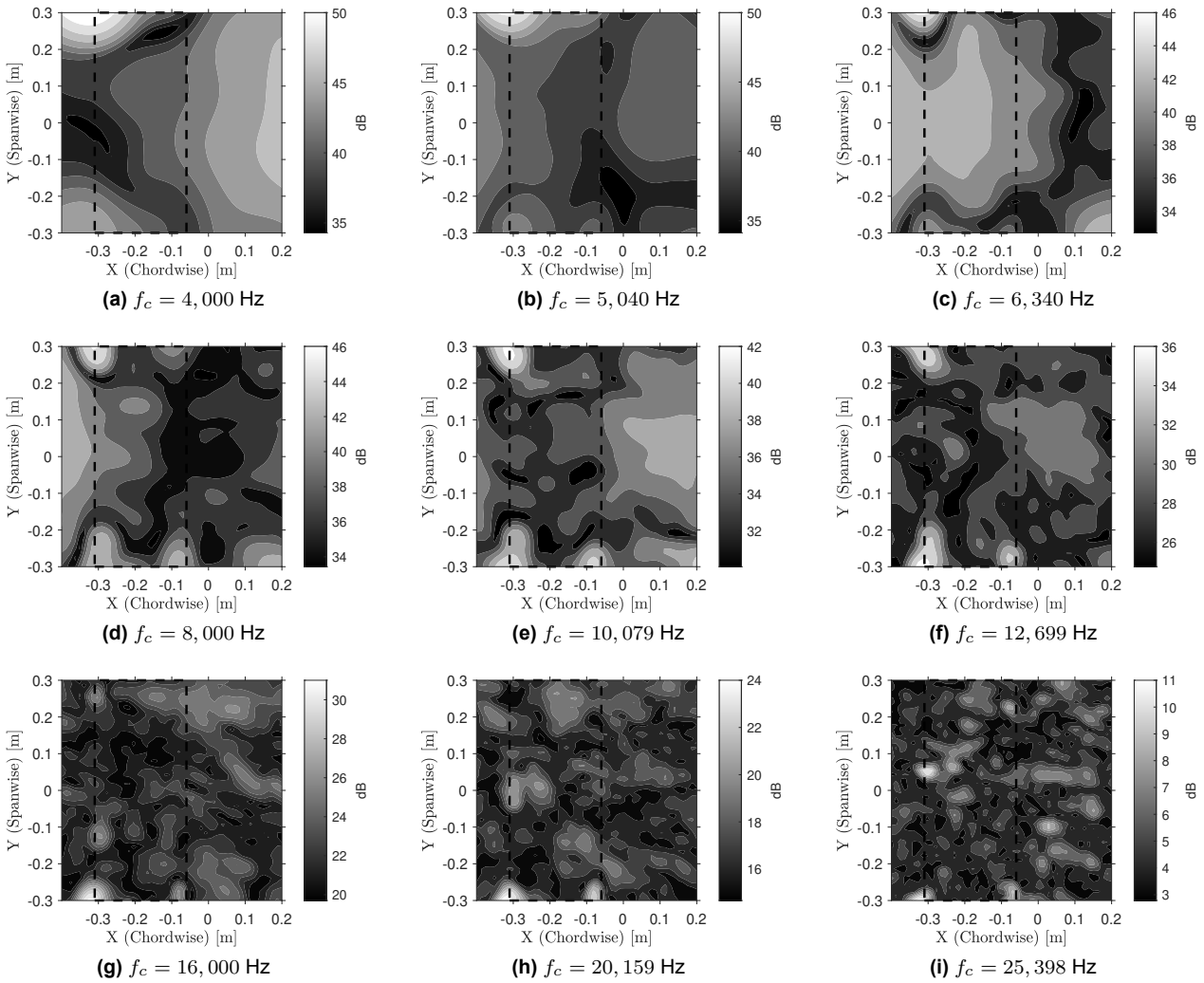

(a) $f_c = 4,000$ Hz **(b)** $f_c = 5,040$ Hz **(c)** $f_c = 6,340$ Hz

(d) $f_c = 8,000$ Hz **(e)** $f_c = 10,079$ Hz **(f)** $f_c = 12,699$ Hz

(g) $f_c = 16,000$ Hz **(h)** $f_c = 20,159$ Hz **(i)** $f_c = 25,398$ Hz

Figure E.2: Beamforming results for Clean airfoil test for the frequency bins $f_c = 4,000$ Hz $- 25,398$ Hz, $\alpha_t = 14°$, and $Re_c \approx 8 \times 10^5$.

E.2. Beamforming results – No Airfoil

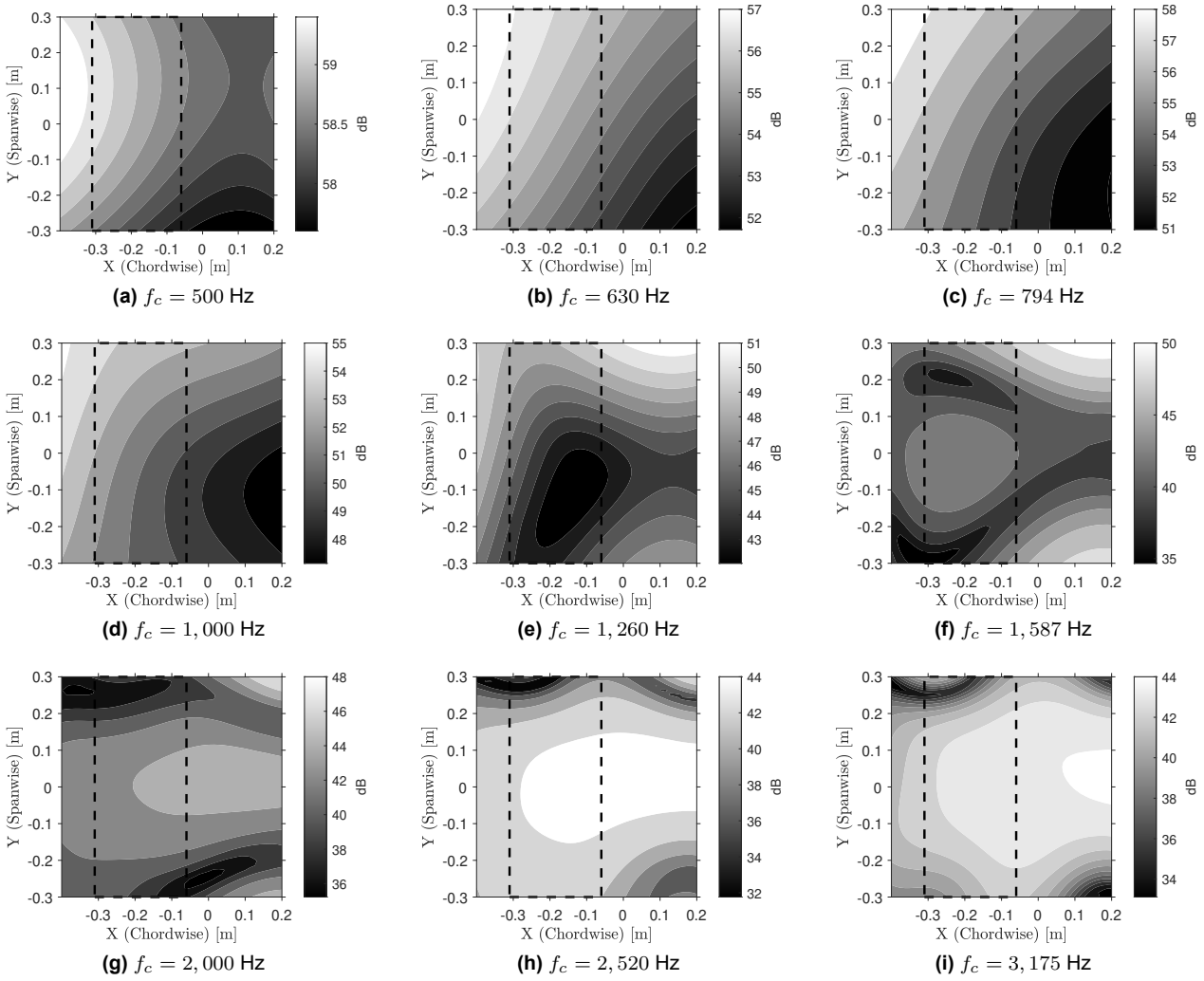

(a) $f_c = 500$ Hz **(b)** $f_c = 630$ Hz **(c)** $f_c = 794$ Hz

(d) $f_c = 1,000$ Hz **(e)** $f_c = 1,260$ Hz **(f)** $f_c = 1,587$ Hz

(g) $f_c = 2,000$ Hz **(h)** $f_c = 2,520$ Hz **(i)** $f_c = 3,175$ Hz

Figure E.3: Beamforming results for No Airfoil test for the frequency bins $f_c = 500$ Hz,–, $3,175$ Hz, $\alpha_t = 14°$, and $Re_c \approx 8 \times 10^5$.

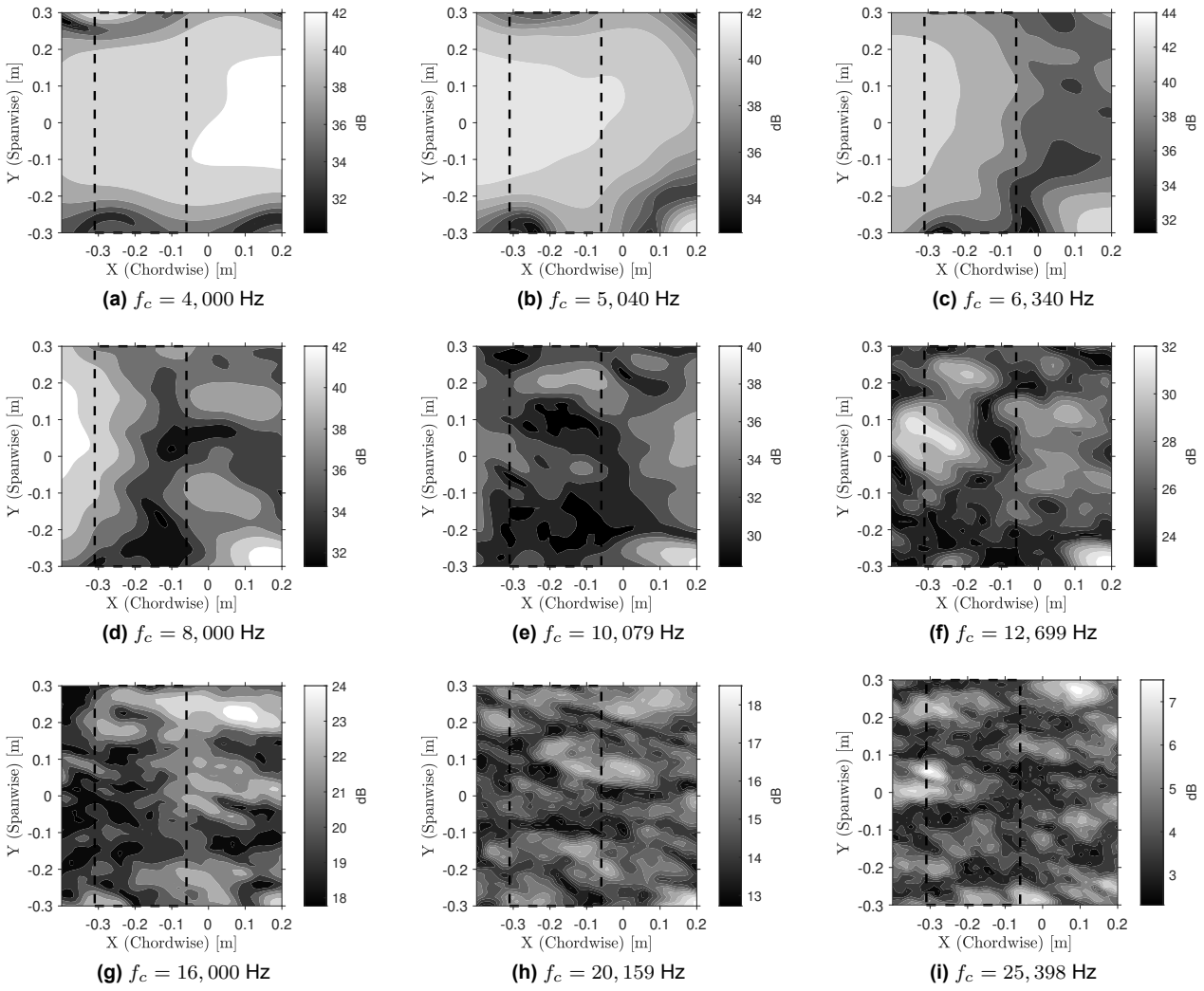

(a) $f_c = 4,000$ Hz **(b)** $f_c = 5,040$ Hz **(c)** $f_c = 6,340$ Hz

(d) $f_c = 8,000$ Hz **(e)** $f_c = 10,079$ Hz **(f)** $f_c = 12,699$ Hz

(g) $f_c = 16,000$ Hz **(h)** $f_c = 20,159$ Hz **(i)** $f_c = 25,398$ Hz

Figure E.4: Beamforming results for No Airfoil test for the frequency bins $f_c = 4,000$ Hz $- 25,398$ Hz, $\alpha_t = 14°$, and $Re_c \approx 8 \times 10^5$.

E.3. Beamforming results – erosion model DL2

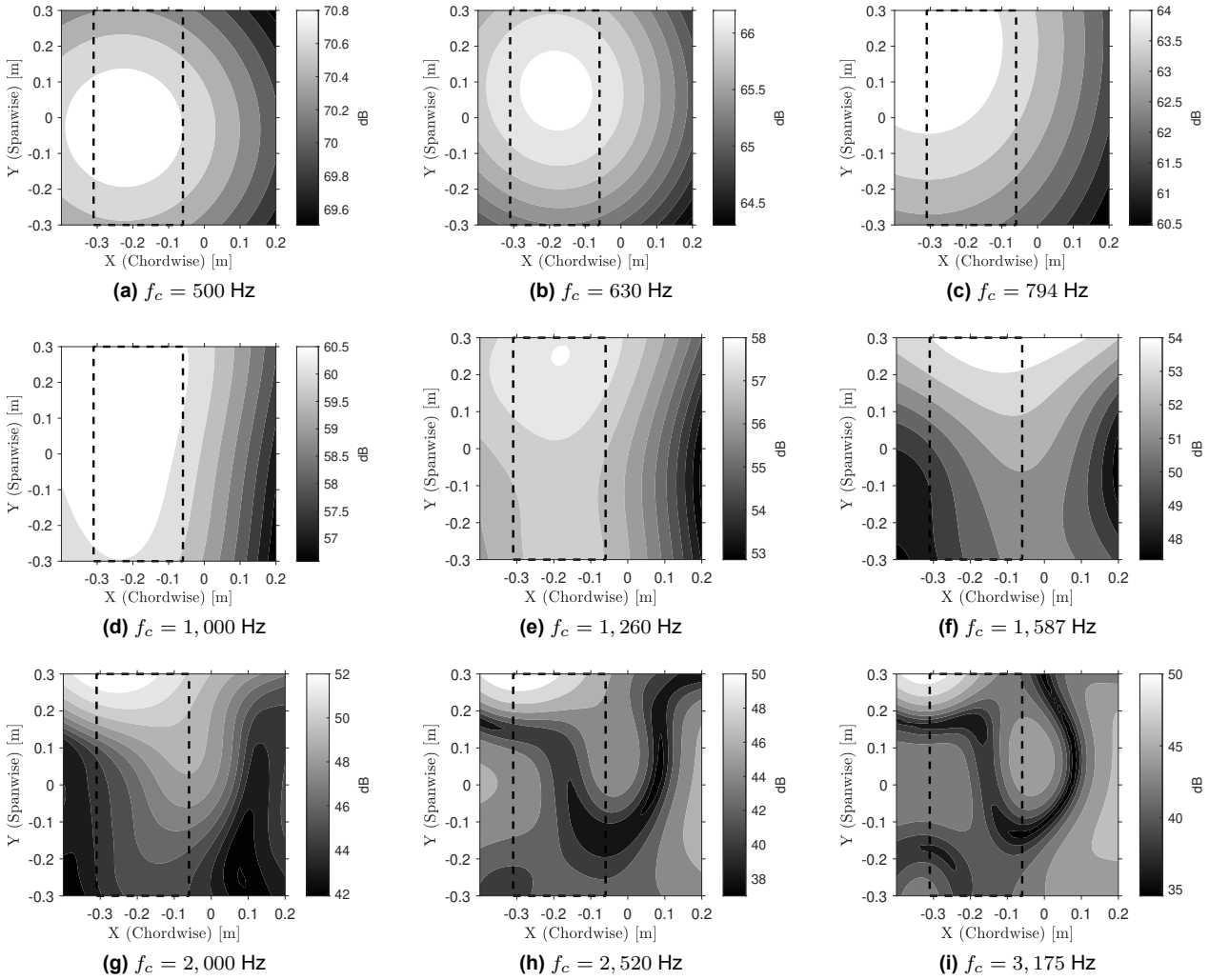

(a) $f_c = 500$ Hz **(b)** $f_c = 630$ Hz **(c)** $f_c = 794$ Hz

(d) $f_c = 1,000$ Hz **(e)** $f_c = 1,260$ Hz **(f)** $f_c = 1,587$ Hz

(g) $f_c = 2,000$ Hz **(h)** $f_c = 2,520$ Hz **(i)** $f_c = 3,175$ Hz

Figure E.5: Beamforming results for erosion model DL2 for the frequency bins $f_c = 500$ Hz $- 3,175$ Hz, $\alpha_t = 14°$, and $Re_c \approx 8 \times 10^5$.

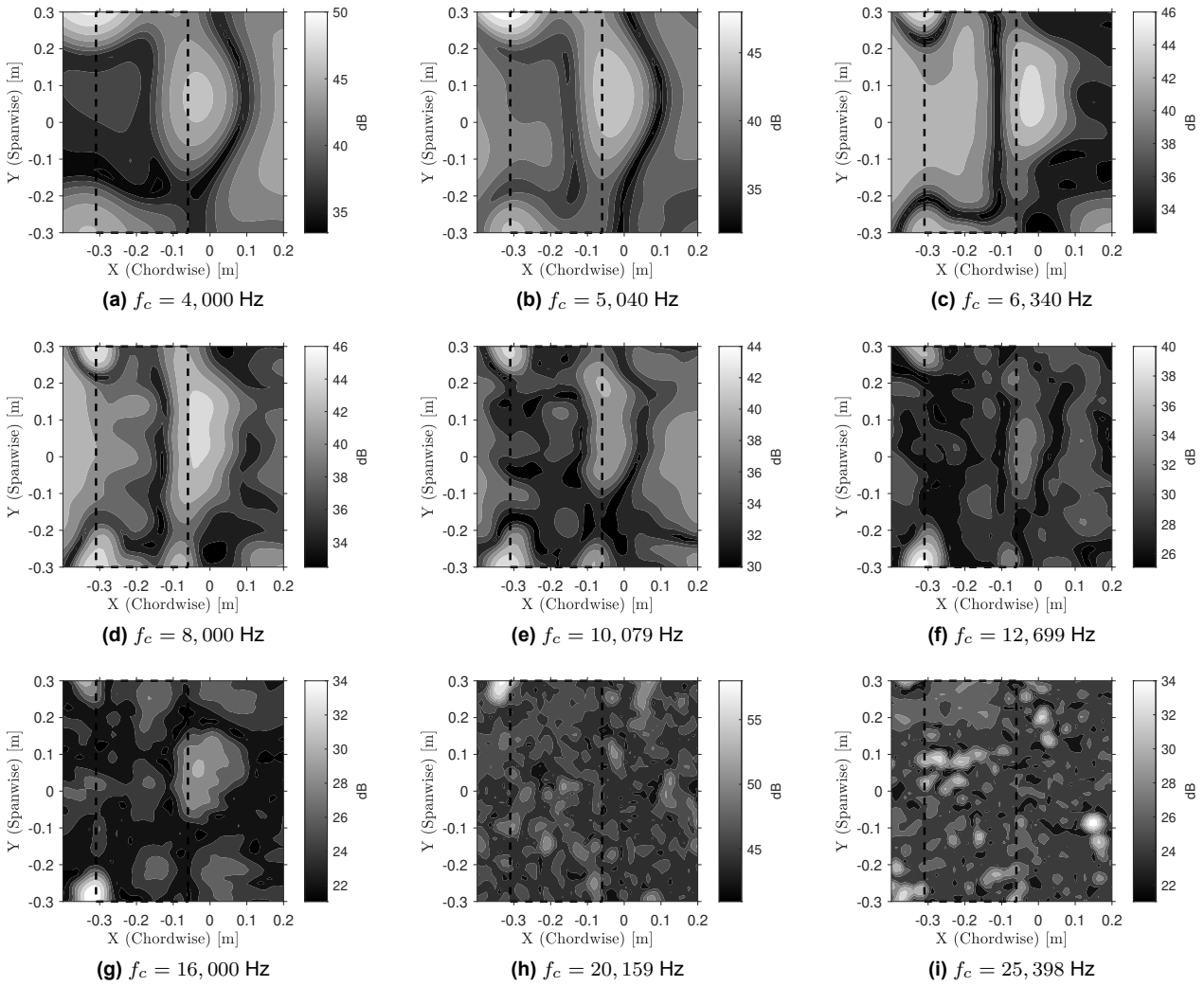

(a) $f_c = 4,000$ Hz **(b)** $f_c = 5,040$ Hz **(c)** $f_c = 6,340$ Hz

(d) $f_c = 8,000$ Hz **(e)** $f_c = 10,079$ Hz **(f)** $f_c = 12,699$ Hz

(g) $f_c = 16,000$ Hz **(h)** $f_c = 20,159$ Hz **(i)** $f_c = 25,398$ Hz

Figure E.6: Beamforming results for erosion model DL2 for the frequency bins $f_c = 4,000$ Hz $- 25,398$ Hz, $\alpha_t = 14°$, and $Re_c \approx 8 \times 10^5$.

E.4. Beamforming results – erosion model DL3

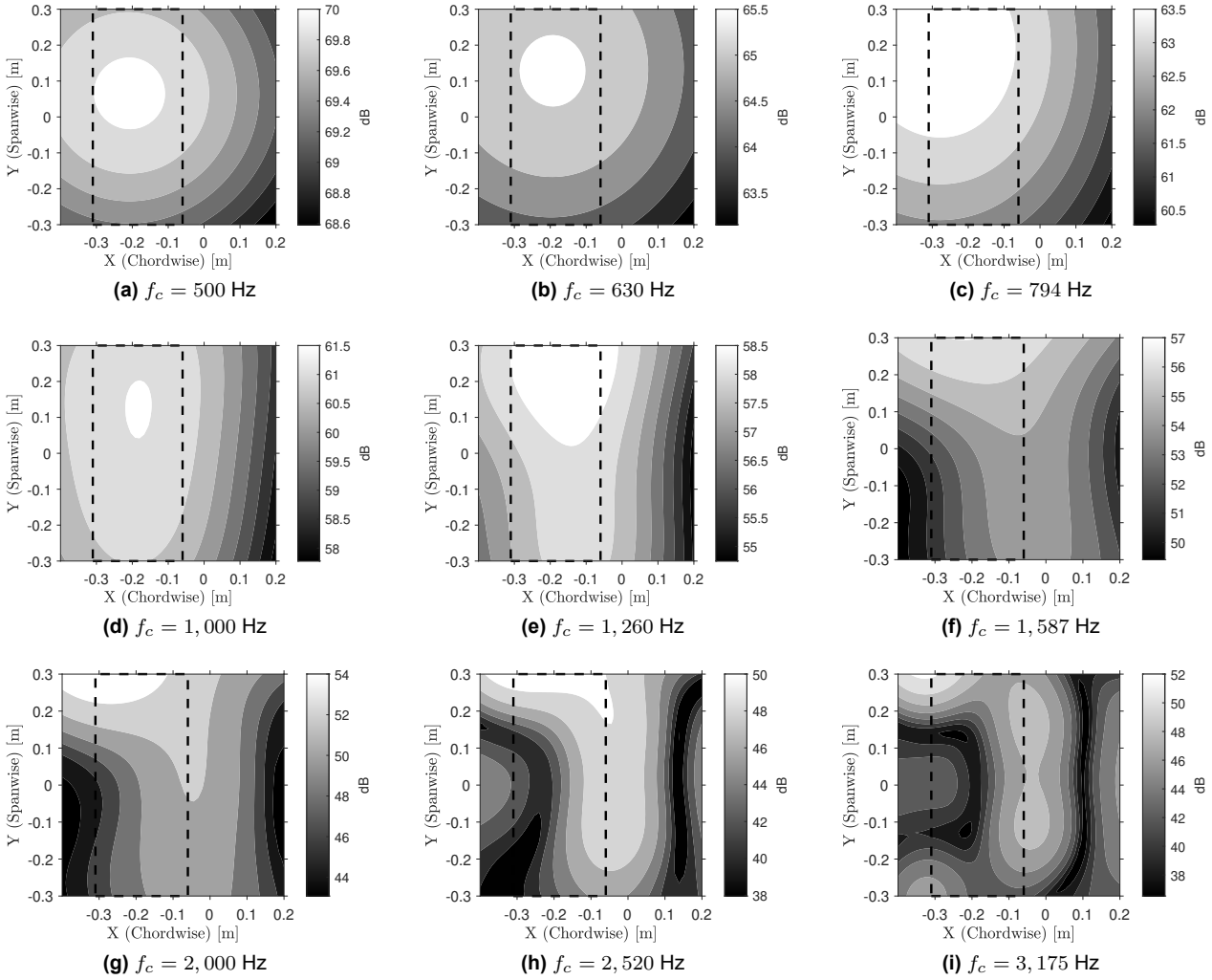

(a) $f_c = 500$ Hz **(b)** $f_c = 630$ Hz **(c)** $f_c = 794$ Hz

(d) $f_c = 1,000$ Hz **(e)** $f_c = 1,260$ Hz **(f)** $f_c = 1,587$ Hz

(g) $f_c = 2,000$ Hz **(h)** $f_c = 2,520$ Hz **(i)** $f_c = 3,175$ Hz

Figure E.7: Beamforming results for erosion model DL3 for the frequency bins $f_c = 500$ Hz $- 3,175$ Hz, $\alpha_t = 14°$, and $Re_c \approx 8 \times 10^5$.

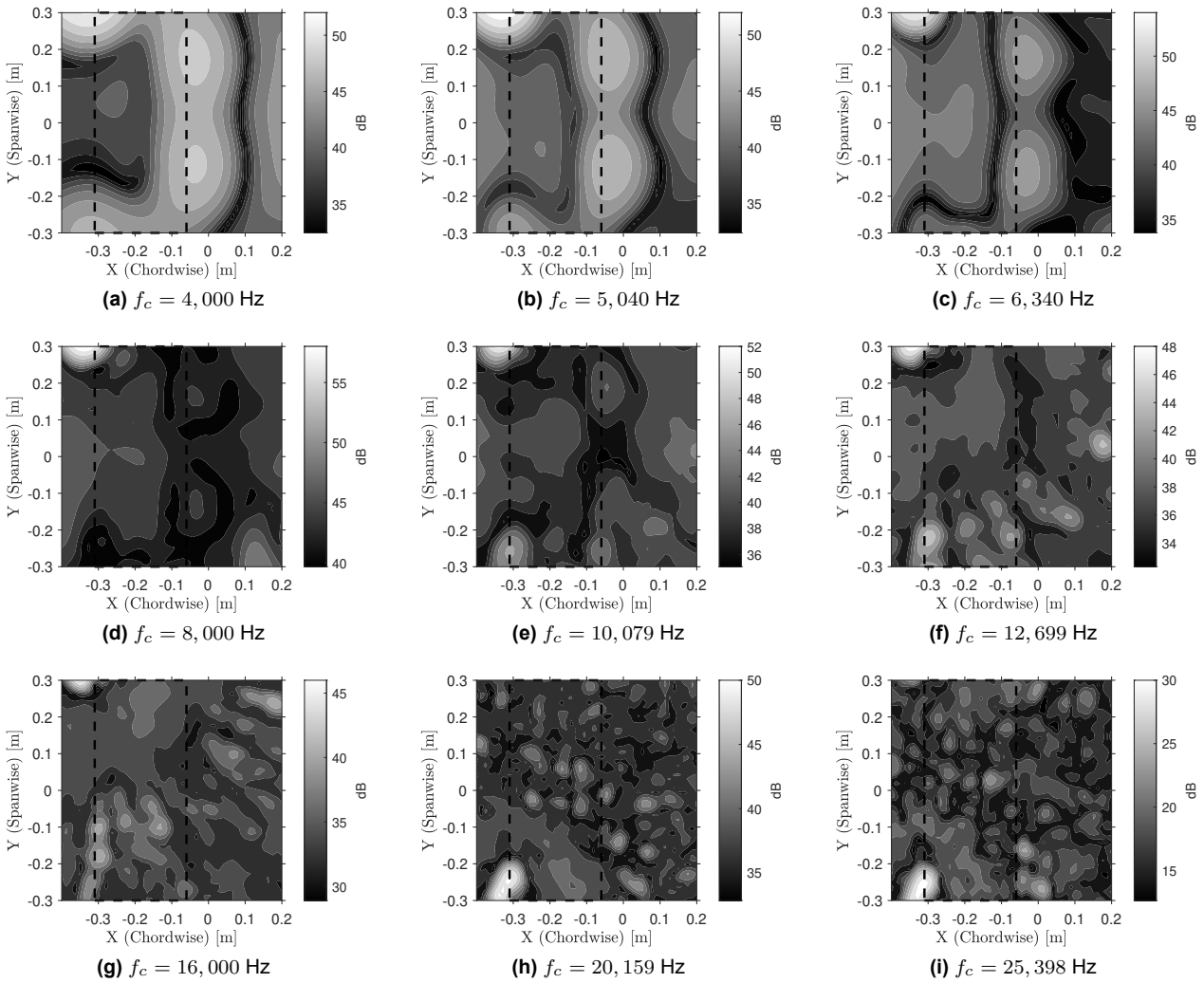

(a) $f_c = 4,000$ Hz **(b)** $f_c = 5,040$ Hz **(c)** $f_c = 6,340$ Hz

(d) $f_c = 8,000$ Hz **(e)** $f_c = 10,079$ Hz **(f)** $f_c = 12,699$ Hz

(g) $f_c = 16,000$ Hz **(h)** $f_c = 20,159$ Hz **(i)** $f_c = 25,398$ Hz

Figure E.8: Beamforming results for erosion model DL3 for the frequency bins $f_c = 4,000$ Hz $- 25,398$ Hz, $\alpha_t = 14°$, and $Re_c \approx 8 \times 10^5$.

E.5. Beamforming results – erosion model DL4

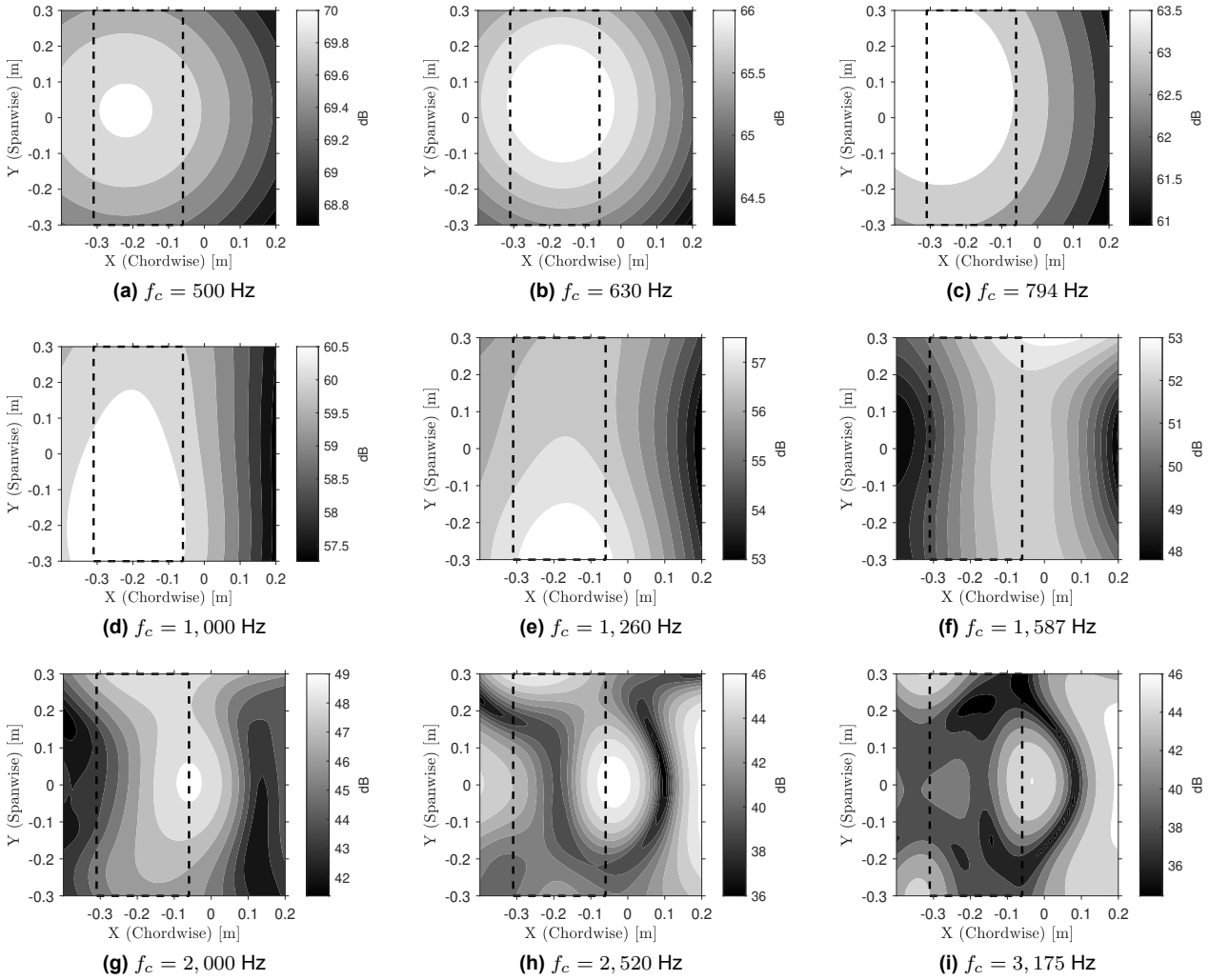

(a) $f_c = 500$ Hz **(b)** $f_c = 630$ Hz **(c)** $f_c = 794$ Hz

(d) $f_c = 1,000$ Hz **(e)** $f_c = 1,260$ Hz **(f)** $f_c = 1,587$ Hz

(g) $f_c = 2,000$ Hz **(h)** $f_c = 2,520$ Hz **(i)** $f_c = 3,175$ Hz

Figure E.9: Beamforming results for erosion model DL4 for the frequency bins $f_c = 500$ Hz $- 3,175$ Hz, $\alpha_t = 14°$, and $Re_c \approx 8 \times 10^5$.

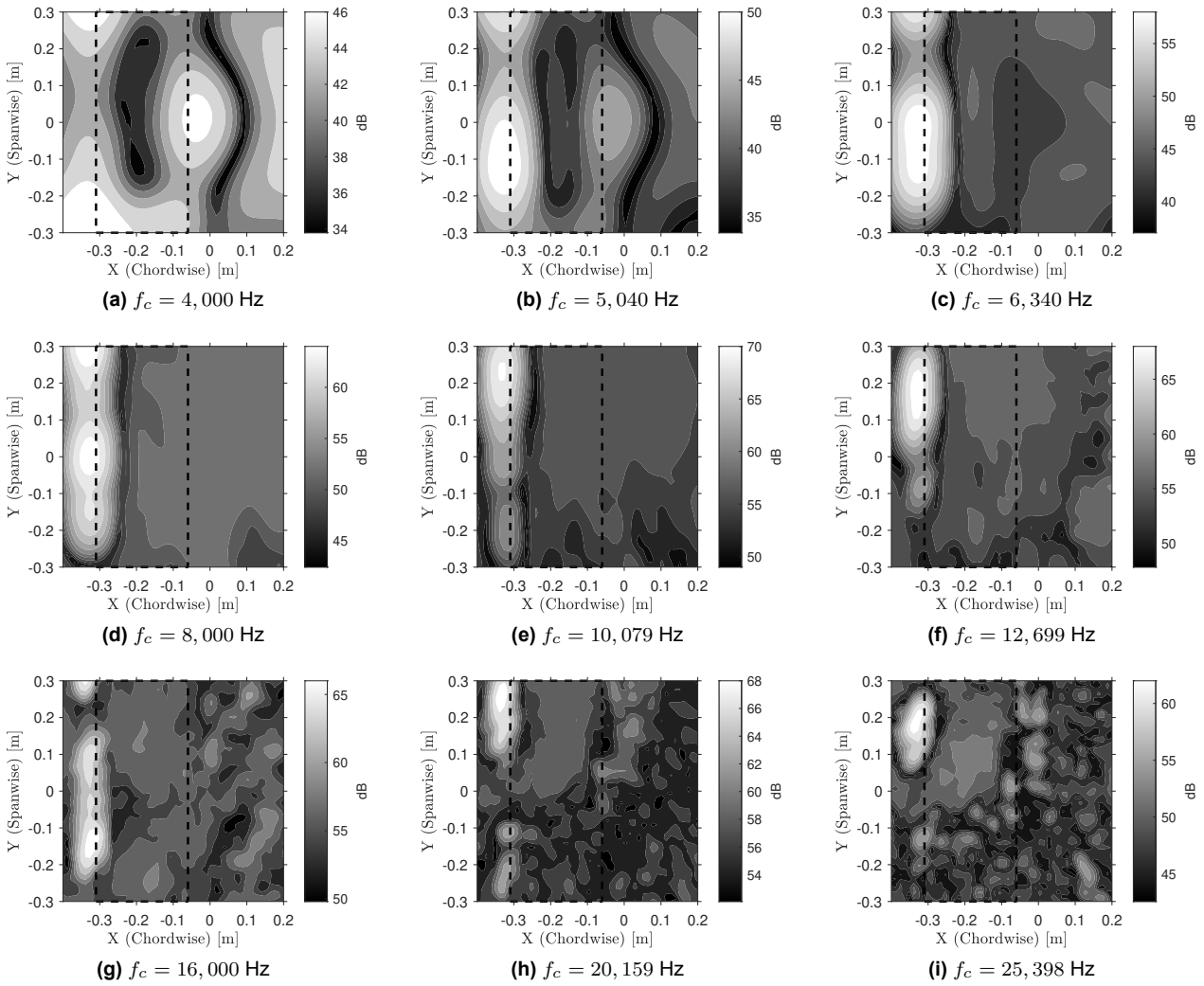

(a) $f_c = 4,000$ Hz **(b)** $f_c = 5,040$ Hz **(c)** $f_c = 6,340$ Hz

(d) $f_c = 8,000$ Hz **(e)** $f_c = 10,079$ Hz **(f)** $f_c = 12,699$ Hz

(g) $f_c = 16,000$ Hz **(h)** $f_c = 20,159$ Hz **(i)** $f_c = 25,398$ Hz

Figure E.10: Beamforming results for erosion model DL4 for the frequency bins $f_c = 4,000$ Hz $- 25,398$ Hz, $\alpha_t = 14°$, and $Re_c \approx 8 \times 10^5$.

E.6. Beamforming results – erosion model DL5

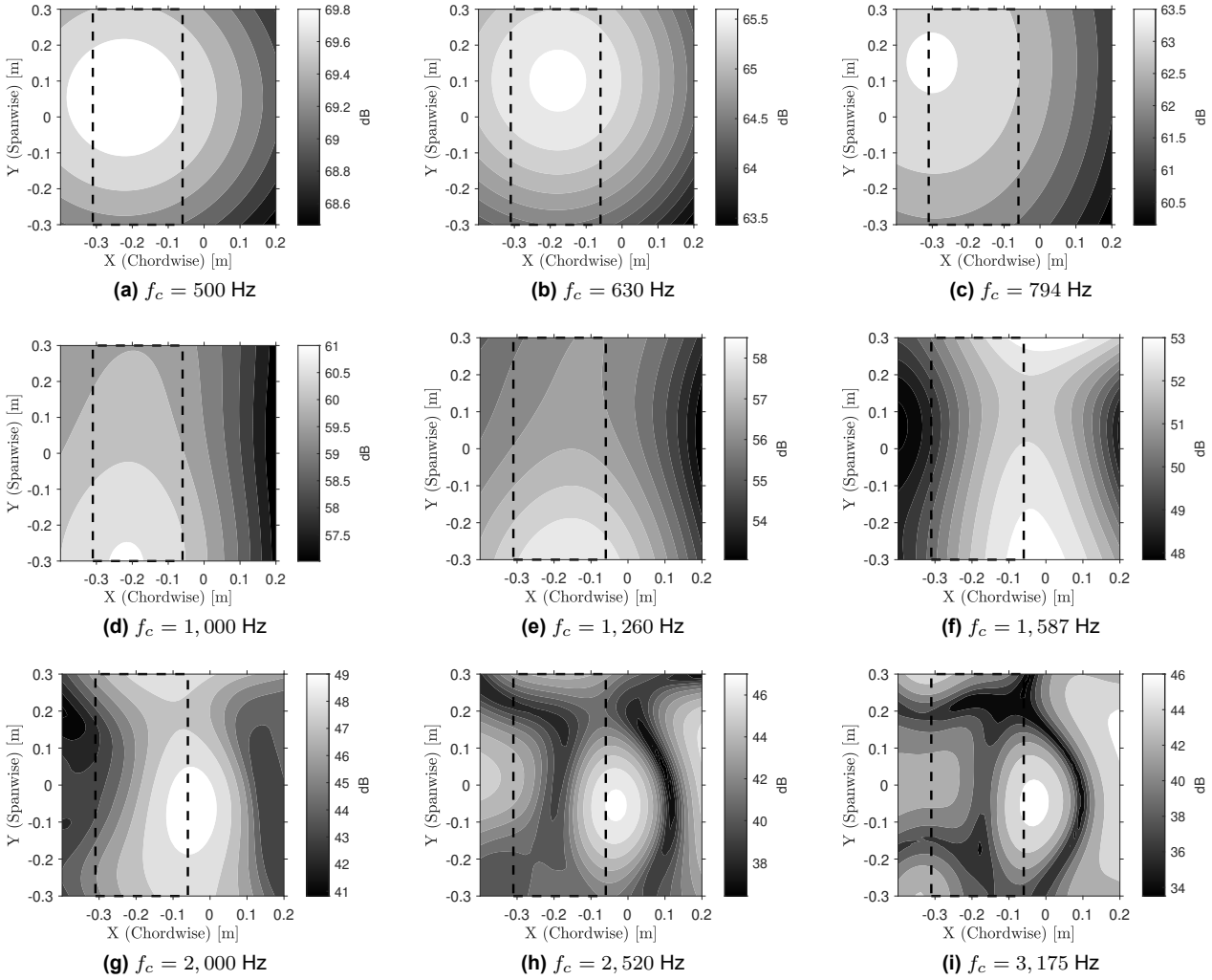

(a) $f_c = 500$ Hz **(b)** $f_c = 630$ Hz **(c)** $f_c = 794$ Hz

(d) $f_c = 1,000$ Hz **(e)** $f_c = 1,260$ Hz **(f)** $f_c = 1,587$ Hz

(g) $f_c = 2,000$ Hz **(h)** $f_c = 2,520$ Hz **(i)** $f_c = 3,175$ Hz

Figure E.11: Beamforming results for erosion model DL5 for the frequency bins $f_c = 500$ Hz $- 3,175$ Hz, $\alpha_t = 14°$, and $Re_c \approx 8 \times 10^5$.

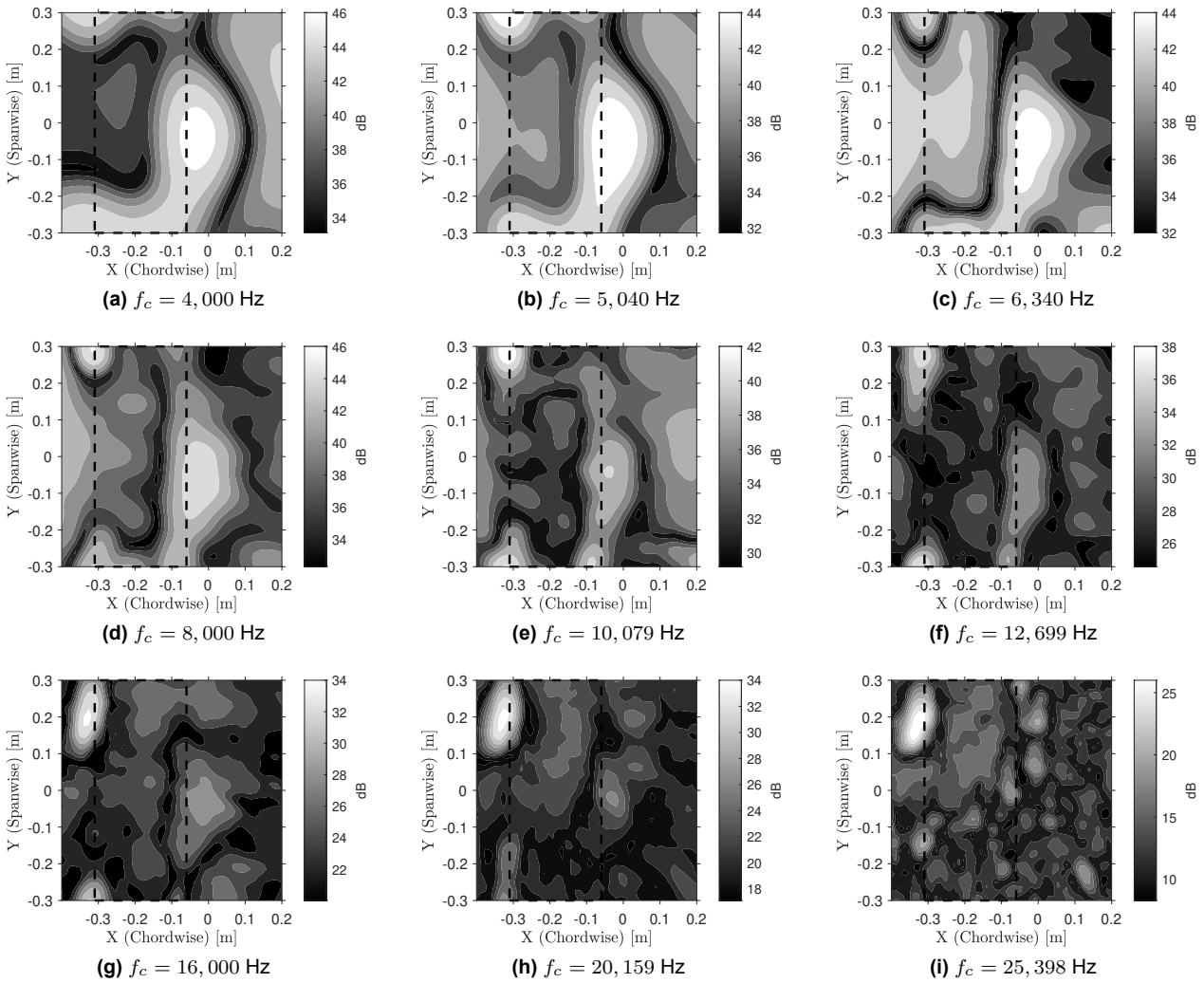

(a) $f_c = 4,000$ Hz **(b)** $f_c = 5,040$ Hz **(c)** $f_c = 6,340$ Hz

(d) $f_c = 8,000$ Hz **(e)** $f_c = 10,079$ Hz **(f)** $f_c = 12,699$ Hz

(g) $f_c = 16,000$ Hz **(h)** $f_c = 20,159$ Hz **(i)** $f_c = 25,398$ Hz

Figure E.12: Beamforming results for erosion model DL5 for the frequency bins $f_c = 4,000$ Hz $- 25,398$ Hz, $\alpha_t = 14°$, and $Re_c \approx 8 \times 10^5$.

E.7. Beamforming results – erosion model DL6

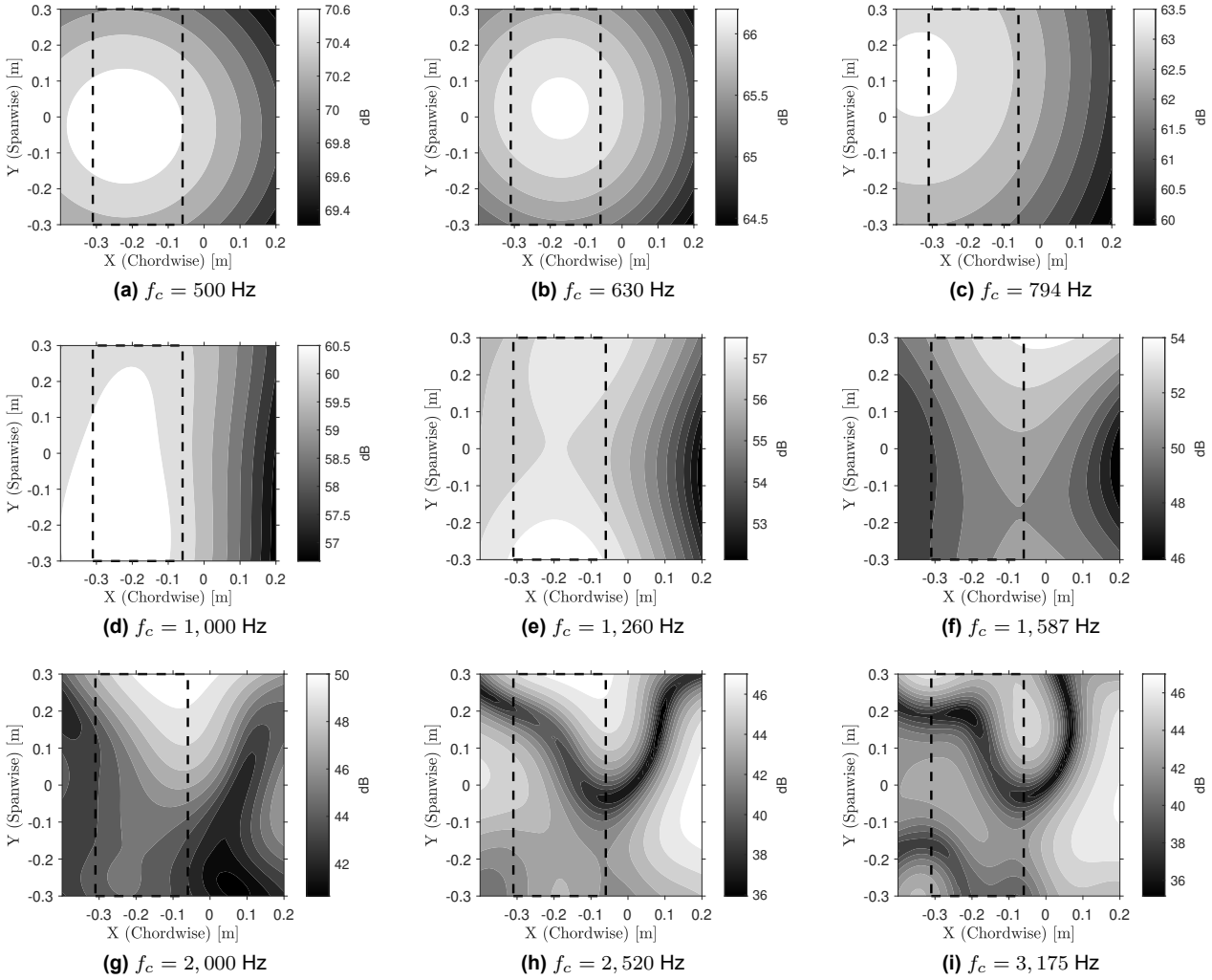

(a) $f_c = 500$ Hz **(b)** $f_c = 630$ Hz **(c)** $f_c = 794$ Hz

(d) $f_c = 1,000$ Hz **(e)** $f_c = 1,260$ Hz **(f)** $f_c = 1,587$ Hz

(g) $f_c = 2,000$ Hz **(h)** $f_c = 2,520$ Hz **(i)** $f_c = 3,175$ Hz

Figure E.13: Beamforming results for erosion model DL6 for the frequency bins $f_c = 500$ Hz $- 3,175$ Hz, $\alpha_t = 14°$, and $Re_c \approx 8 \times 10^5$.

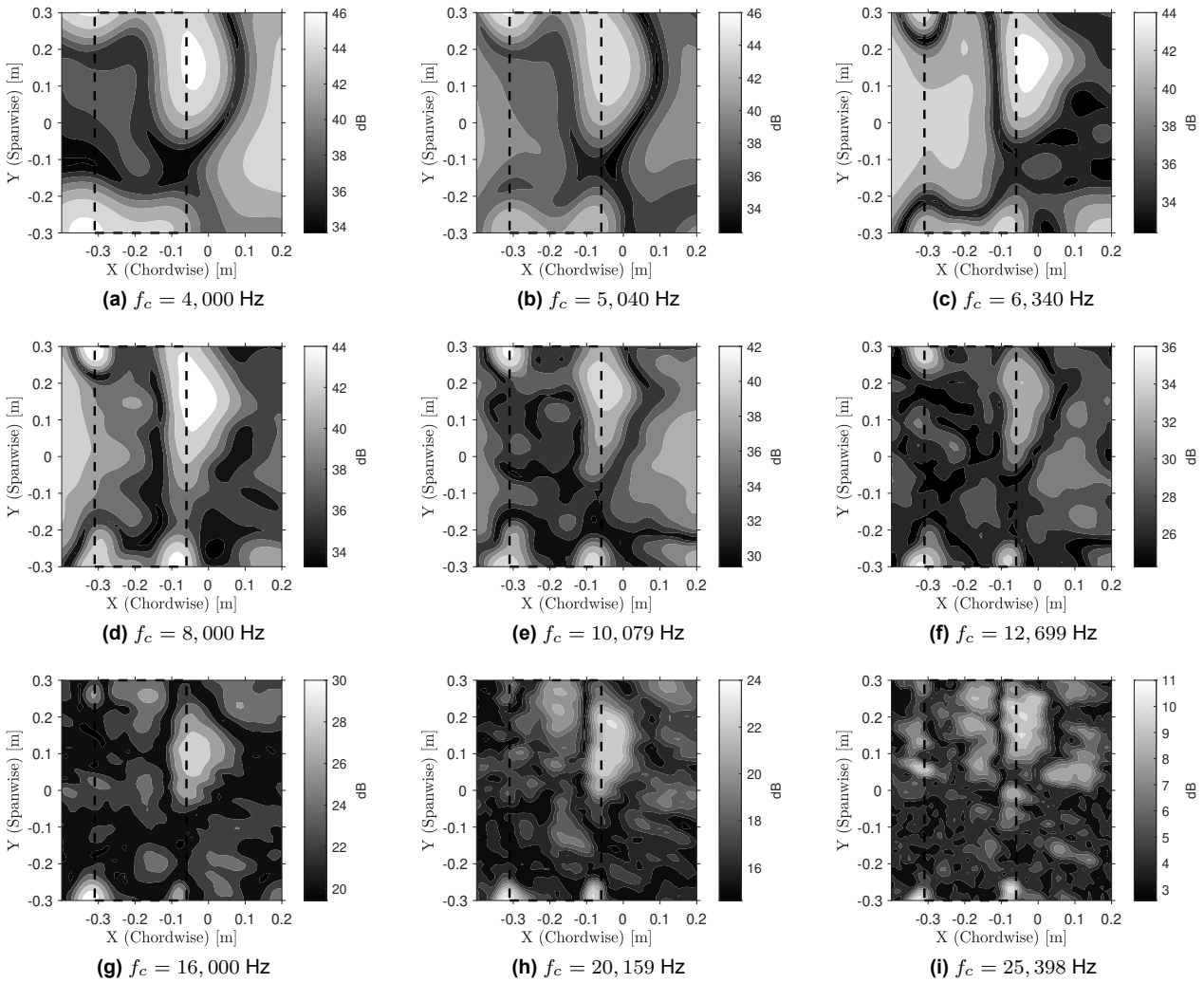

(a) $f_c = 4,000$ Hz **(b)** $f_c = 5,040$ Hz **(c)** $f_c = 6,340$ Hz

(d) $f_c = 8,000$ Hz **(e)** $f_c = 10,079$ Hz **(f)** $f_c = 12,699$ Hz

(g) $f_c = 16,000$ Hz **(h)** $f_c = 20,159$ Hz **(i)** $f_c = 25,398$ Hz

Figure E.14: Beamforming results for erosion model DL6 for the frequency bins $f_c = 4,000$ Hz $- 25,398$ Hz, $\alpha_t = 14°$, and $Re_c \approx 8 \times 10^5$.

E.8. Beamforming results – erosion model P

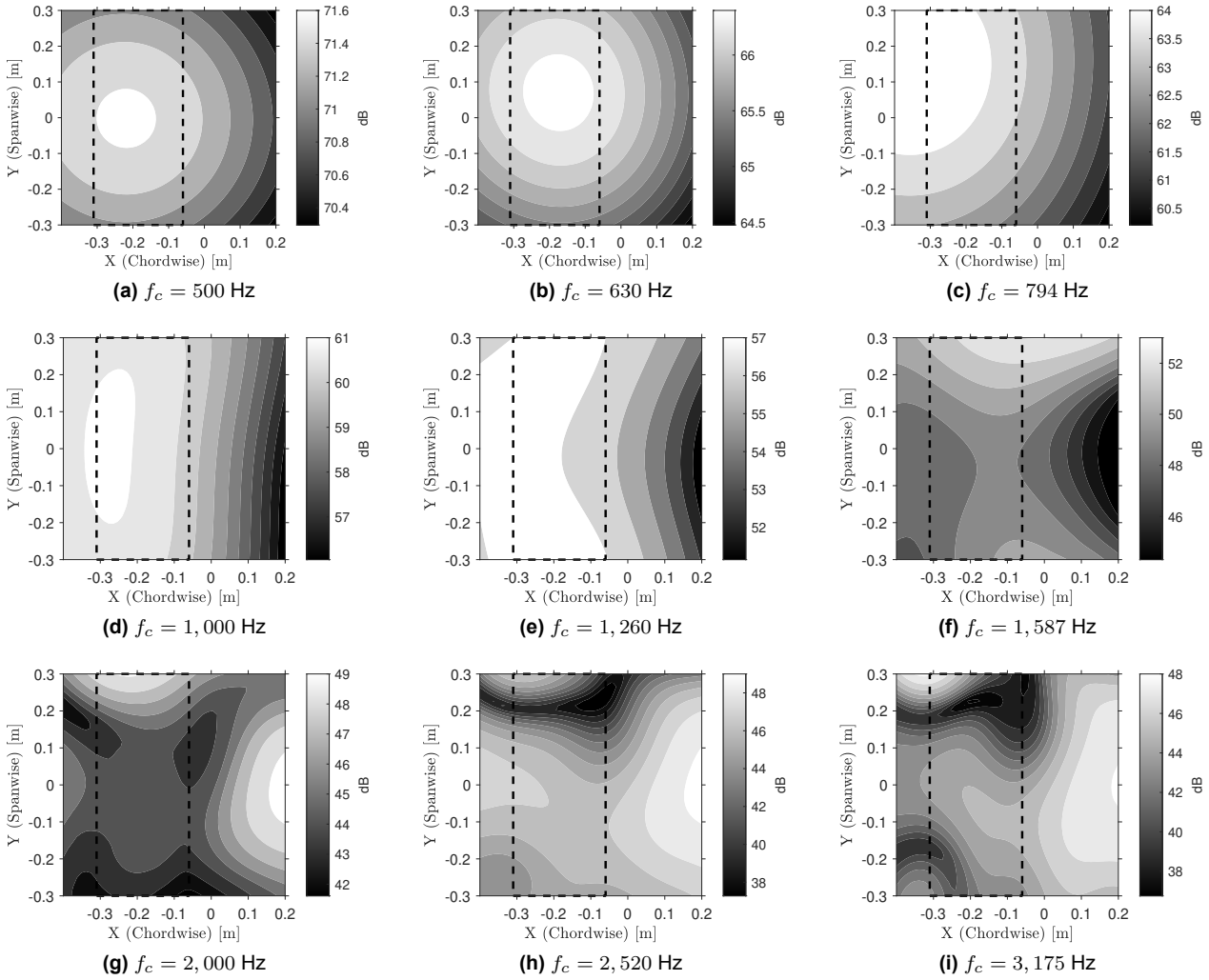

(a) $f_c = 500$ Hz **(b)** $f_c = 630$ Hz **(c)** $f_c = 794$ Hz

(d) $f_c = 1,000$ Hz **(e)** $f_c = 1,260$ Hz **(f)** $f_c = 1,587$ Hz

(g) $f_c = 2,000$ Hz **(h)** $f_c = 2,520$ Hz **(i)** $f_c = 3,175$ Hz

Figure E.15: Beamforming results for erosion model P for the frequency bins $f_c = 500$ Hz $- 3,175$ Hz, $\alpha_t = 14°$, and $Re_c \approx 8 \times 10^5$.

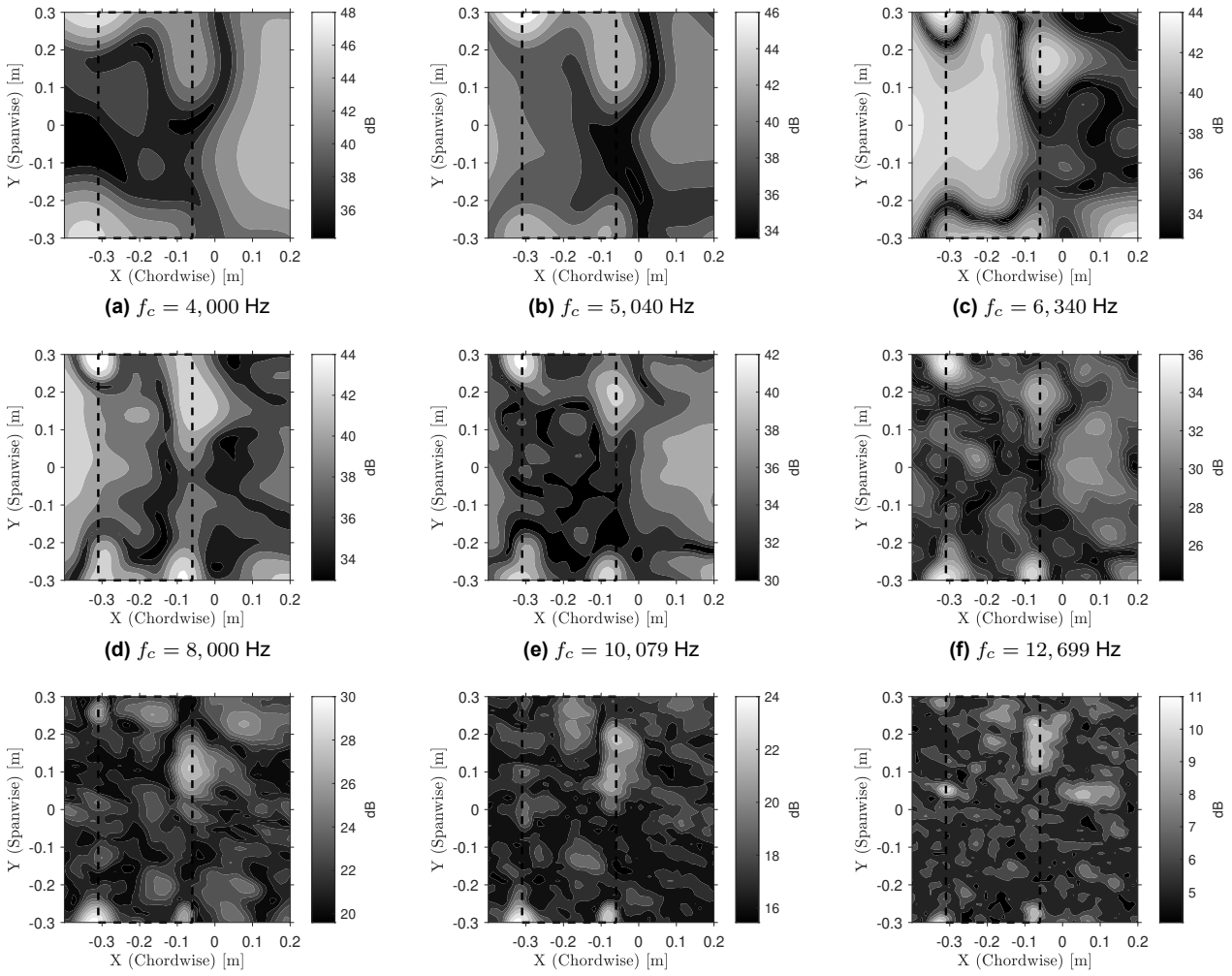

(a) $f_c = 4,000$ Hz **(b)** $f_c = 5,040$ Hz **(c)** $f_c = 6,340$ Hz

(d) $f_c = 8,000$ Hz **(e)** $f_c = 10,079$ Hz **(f)** $f_c = 12,699$ Hz

(g) $f_c = 16,000$ Hz **(h)** $f_c = 20,159$ Hz **(i)** $f_c = 25,398$ Hz

Figure E.16: Beamforming results for erosion model P for the frequency bins $f_c = 4,000$ Hz $- 25,398$ Hz, $\alpha_t = 14°$, and $Re_c \approx 8 \times 10^5$.

E.9. Beamforming results – erosion model PG

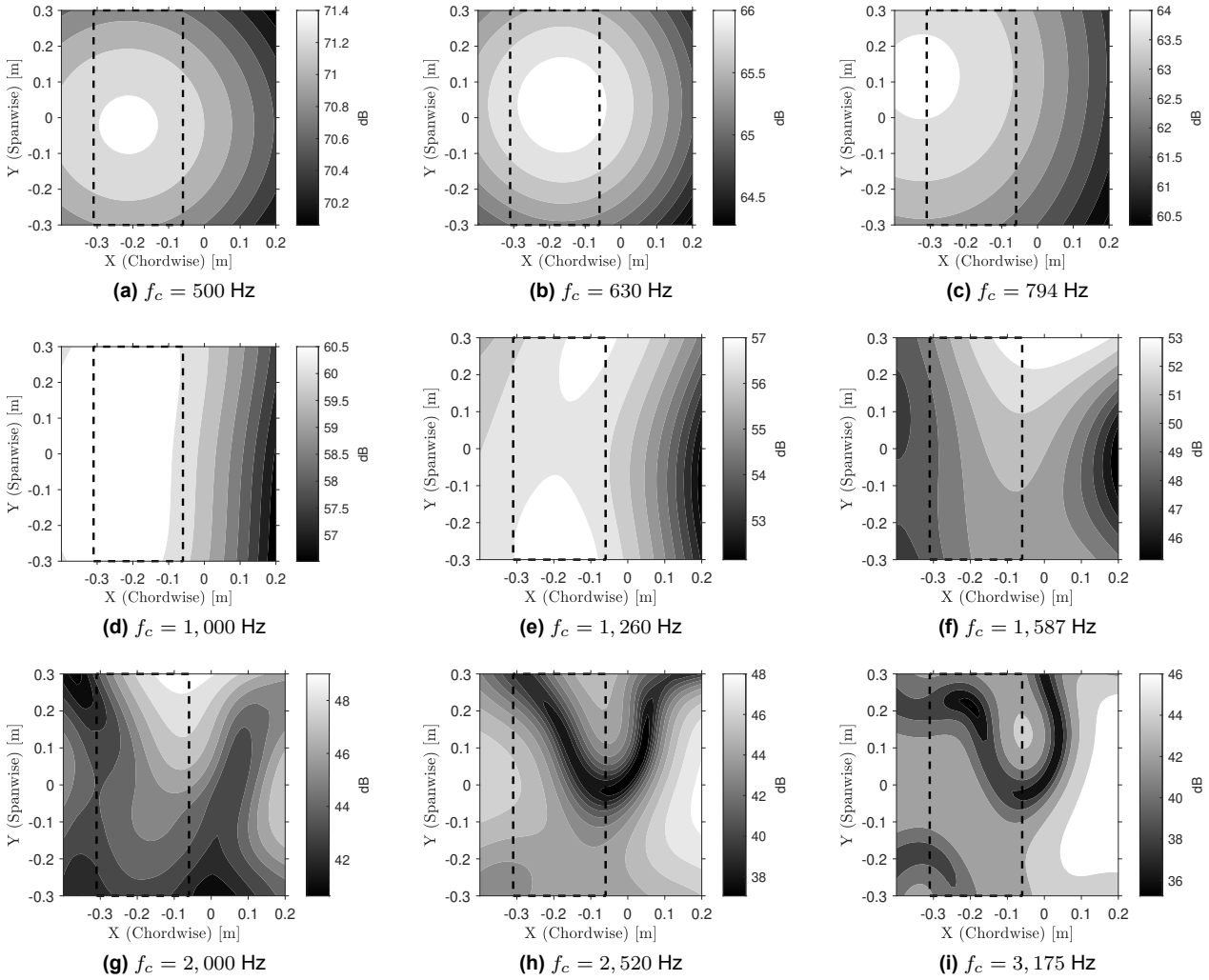

(a) $f_c = 500$ Hz **(b)** $f_c = 630$ Hz **(c)** $f_c = 794$ Hz

(d) $f_c = 1,000$ Hz **(e)** $f_c = 1,260$ Hz **(f)** $f_c = 1,587$ Hz

(g) $f_c = 2,000$ Hz **(h)** $f_c = 2,520$ Hz **(i)** $f_c = 3,175$ Hz

Figure E.17: Beamforming results for erosion model PG for the frequency bins $f_c = 500$ Hz $- 3,175$ Hz, $\alpha_t = 14°$, and $Re_c \approx 8 \times 10^5$.

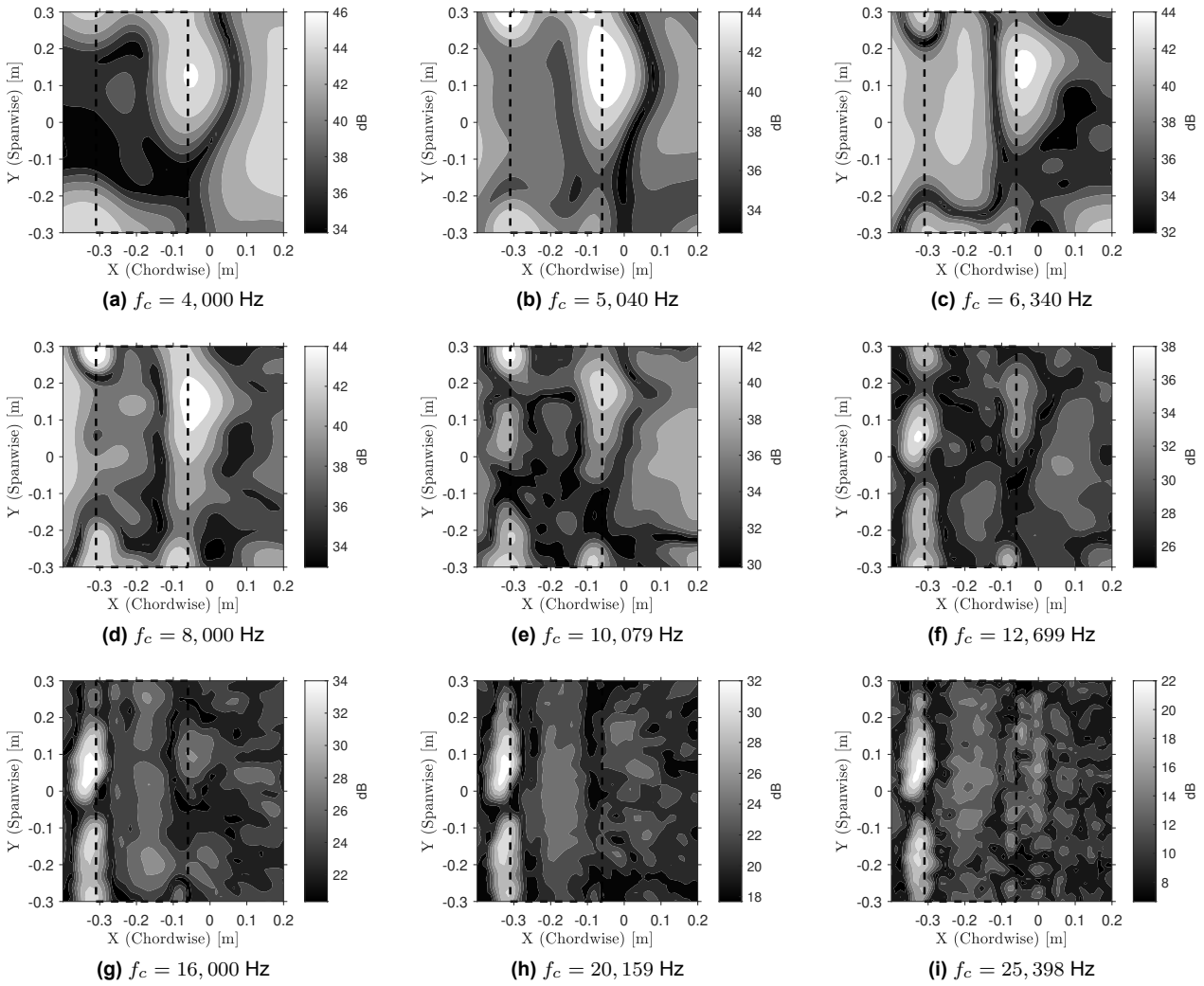

(a) $f_c = 4,000$ Hz **(b)** $f_c = 5,040$ Hz **(c)** $f_c = 6,340$ Hz

(d) $f_c = 8,000$ Hz **(e)** $f_c = 10,079$ Hz **(f)** $f_c = 12,699$ Hz

(g) $f_c = 16,000$ Hz **(h)** $f_c = 20,159$ Hz **(i)** $f_c = 25,398$ Hz

Figure E.18: Beamforming results for erosion model PG for the frequency bins $f_c = 4,000$ Hz $- 25,398$ Hz, $\alpha_t = 14°$, and $Re_c \approx 8 \times 10^5$.

F

PSD comparison

F.1. PSD all erosion models at $Re_c \approx 6 \times 10^5$, $\alpha_t = 14°$

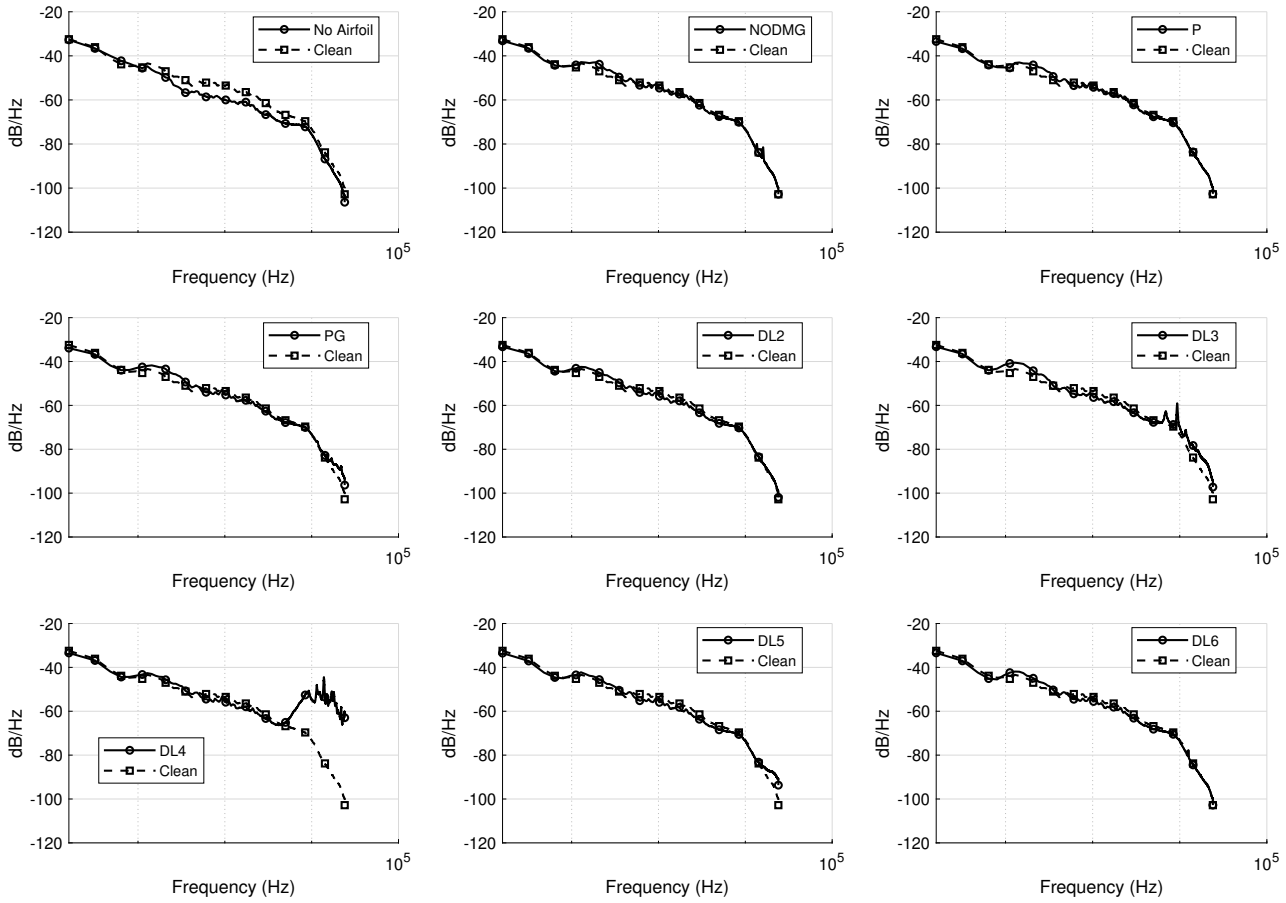

Figure F.1: PSD of all erosion models at $Re_c \approx 6 \times 10^5$, $\alpha_t = 14°$

F.2. $Re_c \approx 7 \times 10^5$, $\alpha_t = 14°$

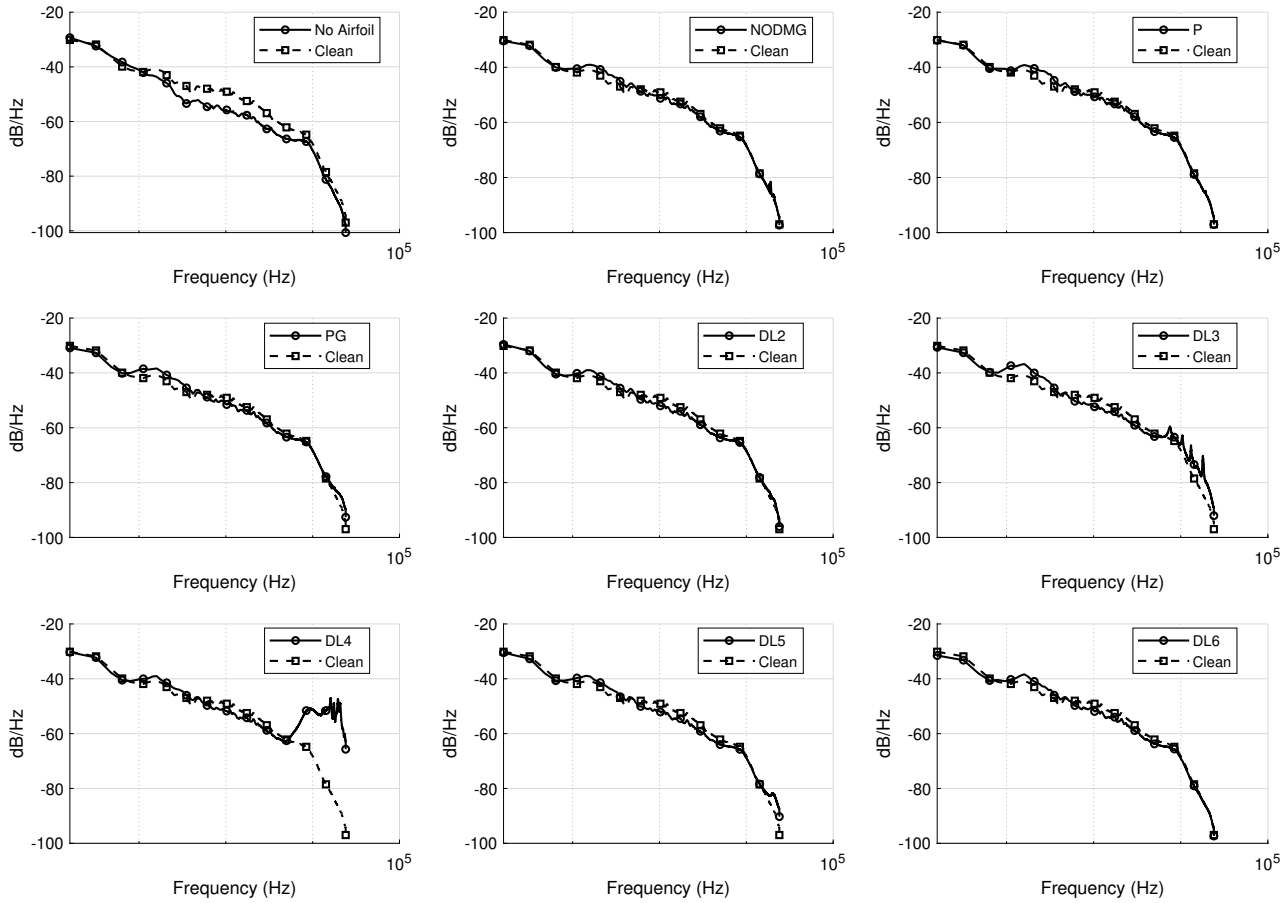

Figure F.2: PSD of all erosion models at $Re_c \approx 7 \times 10^5$, $\alpha_t = 14°$

F.3. $Re_c \approx 8 \times 10^5$, $\alpha_t = 14°$

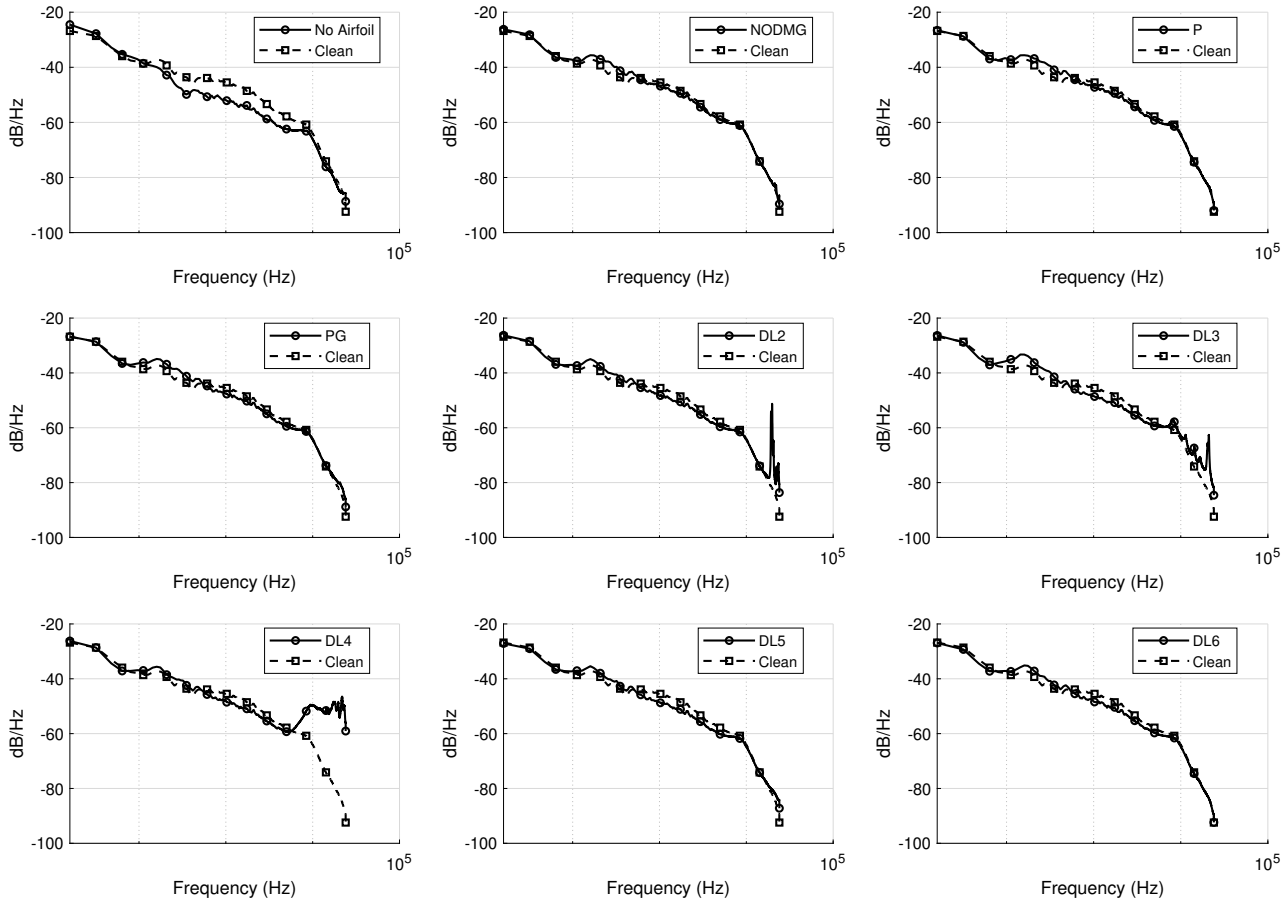

Figure F.3: PSD of all erosion models at $Re_c \approx 8 \times 10^5$, $\alpha_t = 14°$

G

Calibration reports

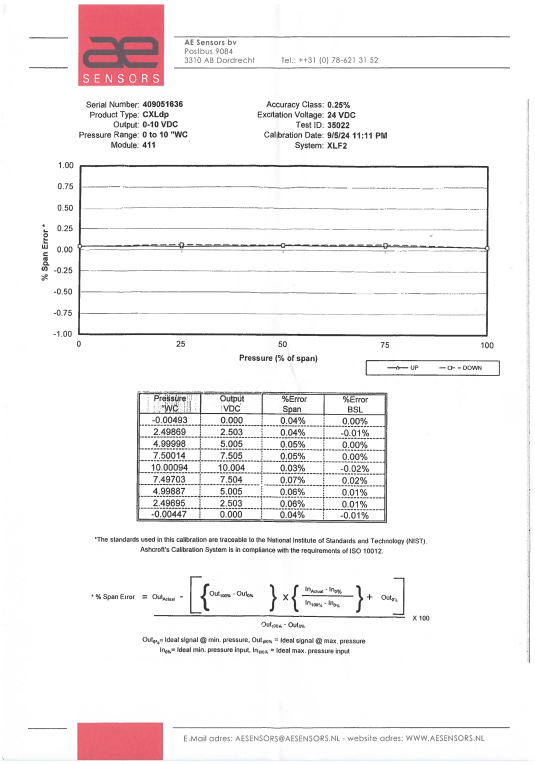

AE Sensors bv
Postbus 9084
3310 AB Dordrecht
Tel.: ++31 (0) 78-621 31 52

Serial Number: **409051636**
Product Type: **CXLdp**
Output: **0-10 VDC**
Pressure Range: **0 to 10 "WC**
Module: **411**

Accuracy Class: **0.25%**
Excitation Voltage: **24 VDC**
Test ID: **38022**
Calibration Date: **9/5/24 11:11 PM**
System: **XLF2**

Pressure "WC	Output VDC	%Error Span	%Error BSL
-0.00493	0.000	0.04%	0.00%
2.49869	2.503	0.04%	-0.01%
4.99998	5.005	0.05%	0.00%
7.50014	7.505	0.05%	0.00%
10.00094	10.004	0.03%	-0.02%
7.49703	7.504	0.07%	0.02%
4.99887	5.005	0.06%	0.01%
2.49695	2.503	0.06%	0.01%
-0.00447	0.000	0.04%	-0.01%

*The standards used in this calibration are traceable to the National Institute of Standards and Technology (NIST).
Ashcroft's Calibration System is in compliance with the requirements of ISO 10012.

$$\%\ \text{Span Error} = Out_{Actual} - \left[\left\{Out_{@Pa} - Out_{@0}\right\} \times \left\{\frac{In_{Actual} - In_{@0}}{In_{@Pa} - In_{@0}}\right\} + Out_{@0}\right] \Big/ \left(Out_{@Pa} - Out_{@0}\right) \times 100$$

$Out_{@0}$ = Ideal signal @ min. pressure, $Out_{@Pa}$ = Ideal signal @ max. pressure
$In_{@0}$ = Ideal min. pressure input, $In_{@Pa}$ = Ideal max. pressure input

E-Mail adres: AESENSORS@AESENSORS.NL - website adres: WWW.AESENSORS.NL

(a) Calibration report pitot rube pressure sensor

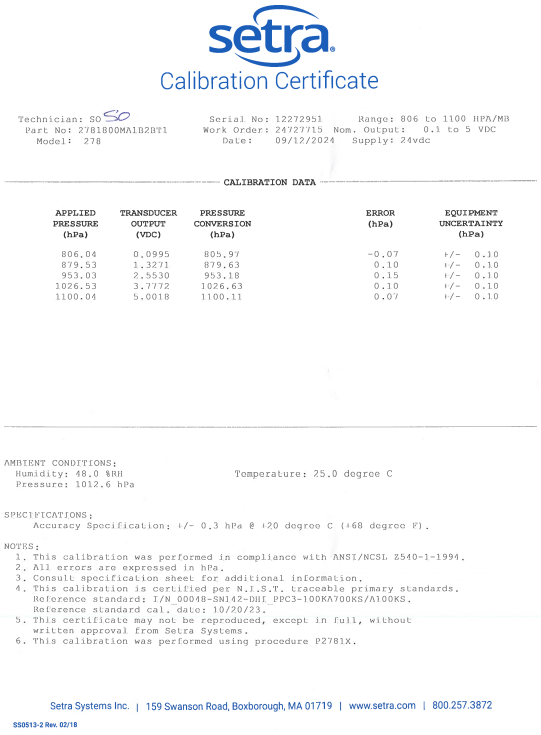

setra
Calibration Certificate

Technician: SO
Part No: 2781B00MA1B2BT1
Model: 278

Serial No: 12272951
Work Order: 24727715
Date: 09/12/2024

Range: 806 to 1100 HPA/MB
Nom. Output: 0.1 to 5 VDC
Supply: 24vdc

CALIBRATION DATA

APPLIED PRESSURE (hPa)	TRANSDUCER OUTPUT (VDC)	PRESSURE CONVERSION (hPa)	ERROR (hPa)	EQUIPMENT UNCERTAINTY (hPa)
806.04	0.0995	805.97	-0.07	+/- 0.10
879.53	1.3271	879.63	0.10	+/- 0.10
953.03	2.5530	953.18	0.15	+/- 0.10
1026.53	3.7772	1026.63	0.10	+/- 0.10
1100.04	5.0018	1100.11	0.07	+/- 0.10

AMBIENT CONDITIONS:
Humidity: 48.0 %RH
Pressure: 1012.6 hPa
Temperature: 25.0 degree C

SPECIFICATIONS:
Accuracy Specification: +/- 0.3 hPa @ +20 degree C (+68 degree F).

NOTES:
1. This calibration was performed in compliance with ANSI/NCSL Z540-1-1994.
2. All errors are expressed in hPa.
3. Consult specification sheet for additional information.
4. This calibration is certified per N.I.S.T. traceable primary standards.
Reference standard: I/N 00048-SN142-DHI PPC3-100KA700KS/A100KS.
Reference standard cal. date: 10/20/23.
5. This certificate may not be reproduced, except in full, without written approval from Setra Systems.
6. This calibration was performed using procedure P2781X.

Setra Systems Inc. | 159 Swanson Road, Boxborough, MA 01719 | www.setra.com | 800.257.3872

SS0513-2 Rev. 02/18

(b) Calibration report static pressure sensor

Figure G.1: Calibration reports pressure sensors